

ACTA MATERIALIA TRANSYLVANICA

Anyagtudományi Közlemények

3. évfolyam, 2020. 1. szám



ERDÉLYI MÚZEUM-EGYESÜLET
Kolozsvár
2020

A folyóirat megjelenését támogatta a Magyar Tudományos Akadémia, a Bethlen Gábor Alapkezelő Zrt. és az EME Műszaki Tudományok Szakosztálya / The publication of this magazine was supported by the Hungarian Academy of Sciences, by the Bethlen Gábor Fund and by the TMS – Department of Engineering Sciences



Főszerkesztő / Editor-in-Chief: Bitay Enikő

Nemzetközi Tanácsadó testület / International Editorial Advisory Board:

Prof. Biró László Péter, MTA Energiatudományi Kutatóközpont, Budapest, Magyarország
 Prof. emer. B. Nagy János, University of Namur, Namur, Belgium
 Prof. Czigány Tibor, Budapesti Műszaki és Gazdaságtudományi Egyetem, Budapest, Magyarország
 Prof. Diószegi Attila, Jönköping University, Jönköping, Svédország
 Dobránszky János, MTA–BME Kompozittechnológiai Kutatócsoport, Budapest, Magyarország
 Prof. Dusza János, Institute of Materials Research of Slovak Academy of Sciences, Kassa, Szlovákia
 Prof. Gyenge Csaba, Technical University of Cluj-Napoca, Kolozsvár, Románia
 Prof. emer. Gyulai József, Budapesti Műszaki és Gazdaságtudományi Egyetem, Budapest, Magyarország
 Prof. Kaptay György, Miskolci Egyetem, Miskolc, Magyarország
 Dr. Kolozsváry Zoltán, Plasmaterm Rt., Marosvásárhely, Románia
 Prof. Mertinger Valéria, Miskolci Egyetem, Miskolc, Magyarország
 Prof. Porkoláb Miklós, Massachusetts Institute of Technology, Cambridge, MA, USA
 Prof. Réger Mihály, Óbudai Egyetem, Budapest, Magyarország
 Prof. emer. Réti Tamás, Óbudai Egyetem, Budapest, Magyarország
 Prof. emer. Roósz András, Miskolci Egyetem, Miskolc, Magyarország
 Dr. Spenik Sándor, Ungvári Nemzeti Egyetem, Ungvár, Ukrajna
 Prof. Zsoldos Ibolya, Széchenyi István Egyetem, Győr, Magyarország

Lapszámszerkesztők / Editorial Board:

Dobránszky János, MTA–BME Kompozittechnológiai Kutatócsoport, Budapest, Magyarország
 Csavdári Alexandra, Babeş–Bolyai Tudományegyetem, Kolozsvár, Románia
 Gergely Attila, Sapientia Erdélyi Magyar Tudományegyetem, Marosvásárhely, Románia
 Kovács Tünde, Óbudai Egyetem, Budapest, Magyarország

Kiadó / Publisher: Erdélyi Múzeum-Egyesület

Felelős kiadó / Responsible publisher: Biró Annamária

Olvasószerkesztő / Proofreader: Szenkovics Enikő (magyar), David Speight (English)

Szerkesztőségi titkár / Editorial secretary: Kisfaludi-Bak Zsombor

Borítóterv / Cover: Könczey Elemér

Nyomdai munkálatok / Printed at: F&F International kft., Gyergyószentmiklós

Copyright © a szerzők / the authors, EME/ TMS 2020

ISSN 2601-1883, ISSN-L 2601-1883

DOI: 10.33923/amt-2020-01

A folyóirat honlapja: <https://www.eme.ro/publication-hu/acta-mat/mat-main.htm>

The journal website: <https://www.eme.ro/publication/acta-mat/mat-main.htm>

Acta Materialia Transylvanica. Anyagtudományi Közlemények az Erdélyi Múzeum-Egyesület (EME) Műszaki Tudományok Szakosztályának folyóirata, amely az anyagtudományok területéről közöl tudományos közleményeket: szakcikkek, összefoglalókat (szemléket), tanulmányokat. A folyóirat célja összképet adni kiemelten a Kárpát-medencei kutatási irányokról, tudományos eredményeiről, s ezt széles körben terjeszteni is. A folyóirat az EME felváltott céljaihoz híven a magyar szaknyelv ápolását is támogatja, így a nyomtatott folyóirat magyar nyelven jelenik meg, mely az Erdélyi digitális adattárban elérhető (<https://eda.eme.ro/handle/10598/30356>). A széles körű nemzetközi terjesztés érdekében a folyóirat teljes angol nyelvű változatát is közzéteesszük.

Acta Materialia Transylvanica – Material Sciences Publications – is a journal of the Technical Sciences Department of the Transylvanian Museum Society, publishing scientific papers, issues, reviews and studies in the field of material sciences. Its mission is to provide and disseminate a comprehensive picture focusing on research trends and scientific results in the Carpathian basin. In accordance with the general mission of the Transylvanian Museum Society it aims to support specialized literature in Hungarian. The printed version of the journal is published in Hungarian and is available in the Transylvanian Digital Database (<https://eda.eme.ro/handle/10598/30356>). However, we would like to spread it internationally, therefore the full content of the journal will also be available in English.

Tartalom / Content

HEGEDŰS Gergely, CZIGÁNY Tibor	1
<i>Polimer kompozitok állapotelemzése üveg fényvezető szállal és távközlési eszközökkel</i>	
<i>State Monitoring of Polymer Composites with Glass Optical Fibre and with Equipment Used in Telecommunication</i>	
ANDRÁS József, KOVÁCS József, ANDRÁS Endre, KERTÉSZ Ildikó, TOMUŞ Ovidiu Bogdan.....	10
<i>A marótárcsás kotrógépek gémszerkezete maradék élettartamának meghatározása roncsolásmentes módszerrel</i>	
<i>Remaining Lifetime Assessment of Bucket Wheel Excavator's Boom Structure by Using Non-destructive Method</i>	
ASZTALOS Lilla, LEVELES Borbála	15
<i>Tetoválótűhegyek károsodásának vizsgálata</i>	
<i>Damage Analysis of Tattoo Needle Tips</i>	
KOVÁCS Dorina, SZABÓ Annamária, KEMÉNY Alexandra	20
<i>Az aktív ernyő anyagának szerepe a plazmanitridálás során</i>	
<i>The Role of the Material of Active Screen During the Plasma Nitriding Process</i>	
KULCSÁR Klaudia, KÓNYA János	26
<i>Zárt és nyitott cellás szerkezeti formák vizsgálata végeelem-analízissel</i>	
<i>Evaluation of Closed and Open-cell Structural Lattices with Finite Element Analysis</i>	
NAGY András, NÉMEDI Imre	33
<i>Mágneses anyagvizsgáló berendezés fejlesztése</i>	
<i>Development of Magnetic Material Testing Equipment</i>	
SCHWEITZER Bence, BENKE Márton, HLAVACS Adrienn, MERTINGER Valéria.....	38
<i>Normál- és keresztthengerelt, lágyított AW-5056 Al-lemezek fülesedésének becslése {h00} pólusábrák alapján</i>	
<i>Earing Prediction of Unidirectionally and Cross-rolled, Annealed AW-5056 Al Sheets from {h00} Pole Figures</i>	

SZABÓ Attila, SÁNTA Róbert, LOVAS Antal, NOVÁK László	43
<i>A FINEMET-ötvözet tulajdonságváltozásának vizsgálata hagyományos, impulzusos és mechanikai feszültség alatt végzett hőkezelést követően</i>	
<i>Investigation of the Property Change in FINEMET Alloy After Conventional, Pulse and Mechanical Stress Annealing</i>	
TÓTH László, KOVÁCS Tünde, NYIKES Zoltán, UMESH Mhatre	50
<i>Az X40CrMoV5-1 jelű acél kopási viselkedése különböző felületkezelések hatására</i>	
<i>The Abrasion Behaviour of X40CrMoV5-1 Steel Under Various Surface Treatments</i>	
WIZNER Krisztián, KŐVÁRI Attila	55
<i>Folyamatosan öntött acélok gyártási körülményeinek hatása a melegen hengerelt termék leminősülésének mértékére</i>	
<i>Effect of the Production Conditions of Continuously Cast Steels on the Degree of Hot Rolled Product Downgrading</i>	

State Monitoring of Polymer Composites with Glass Optical Fibre and with Equipment Used in Telecommunication

Gergely HEGEDŰS,¹ Tibor¹ CZIGÁNY^{1,2*}

¹Budapest University of Technology and Economics, Faculty of Mechanical Engineering, Department of Polymer Engineering, Budapest, Hungary

²MTA–BME Research Group for Composite Science and Technology, Budapest, Hungary

* Corresponding author: czigany@eik.bme.hu

Abstract

Thanks to the widespread use of optical fibers in telecommunication, they, and their accompanying equipment have become cost-effective and easily accessible. We have proved that the changed attenuation of a monomodal optical fiber built into a polymer composite can indicate the elongation of the structure compared to its original, unloaded state, before the optical fiber breaks. We also proved that the location of deformation in polymer composite structures can be found with OTDR equipment (used for checking the coupling of optical fibers).

Keywords: *polymer composite, deformation monitoring, optical fiber, attenuation meter, OTDR.*

1. Introduction

Due to the continuous development of polymer composites, the need to know their material behavior is becoming increasingly important. Because of their complex structure, the simulation of their behavior [1, 2] is a complex task that has to take into account the different structural levels of composites, from the nanoscale material components, through the connection of the micro-level constituents (fiber, matrix) to the macro-level component (layers). For this reason, it is important to monitor the structural health of composites with non-destructive, in-situ physical methods [3]. Their complex structure allows the integration of health monitoring sensors, which greatly increases their competitiveness against other structural materials [4]. With built-in optical sensors, it is possible to monitor deformation, stresses, and the resulting damage and defects during the entire life of the composite (lamination, crosslinking, removal from the mold, assembly, use). Some characteristics of the light (power, phase, polarization, wavelength, timing, and spectral distribution) propagated in the optical fiber of the optical sensors change as a result of external conditions (such as load on the fiber,

deformation) [5]. Common to the different types of optical sensors is that the signal-processing device can be detached from the optical fiber. It is a separate unit; it does not need to be built into the composite [6]. The use of optical sensors is becoming more and more common in laboratories but has not become widespread in cost-sensitive industries (e.g., the automotive industry) because it requires the installation of a relatively complex, expensive system.

An optical fiber is often used to transmit the signal between optical sensors and the processing unit. Nowadays, optical fibers and related telecommunications equipment have become readily available. The most common tool for examining the condition of joints (connections, welds) used in optical networks in telecommunications is the optical power meter. An optical power meter set consists of a light source of specific wavelength (most commonly 1310 and 1550 nm), which can be connected to one end of the optical network, and a power meter unit, which can be connected to the other end of the network. Attenuation ($\alpha(\lambda)$ [dB]) is the ratio of the radiated power input (P_{in}) and the output (P_{out}) of the fiber expressed in decibels [7] (1):

$$\alpha(\lambda) = 10 \cdot \lg(P_{in}/P_{out}) \quad (1)$$

The radiated power required to calculate the attenuation is the power (watts) emitted, transmitted, or received in the form of radiation [8]. Another common tool used to test optical networks is optical time-domain reflectometry (OTDR), which uses reflected light due to Rayleigh scattering. Rayleigh scattering is caused by the micro-anomalies in the optical fiber. As a result of the anomalies, some of the light energy in the fiber is scattered in all directions. The closer the wavelength of the light to the magnitude of the micro-defects is, the greater the degree of scattering. The part of the scattered light that arrives at the cladding of the optical fiber at an angle greater than the critical angle is reflected from it and can even travel backward within the fiber. By measuring the backscattered light, information can be obtained about the inhomogeneities of the fiber, or even about the change of the inhomogeneities. The OTDR sends a pulse of light into the fiber and monitors the light returning from it. The return signal weakens over time as the light travels longer and longer. With the use of the speed of light in the fiber, the starting point of the return signal can be calculated. Rayleigh scattering can be used to localize fiber welds, micro bends, joints, fiber defects, cracks, breaks, and branches within the optical network. With the help of the OTDR, the location of each defect on the optical fiber can be determined with an accuracy of the order of meters [9]. The advantage of the test is that it can be performed from one end of the optical fiber since the instrument measures the pulses reflected from the optical fiber.

Several researchers have shown that micro-level and macro-level bending of optical fibers is reflected in the power of light transmitted through the fiber [10–12]. Several authors have examined the condition of the composite structure with built-in optical fibers, and their results suggest that the decrease in light output at the end of the optical fiber can be used to detect damage [13–15]. This method is suitable for determining the location of the damage, but it does not provide information about its extent.

In our previous papers [16, 17] we investigated the applicability of glass optical fiber to detect the deformation of polymer composites. In this study, we continued to examine the applicability of optical fibers and the devices used in telecommunications for the health monitoring of polymer com-

posite structures. Our aim was to deduce – from the changed characteristic of the light propagating in the built-in optical fiber – the change of the composite compared to its initial, unloaded state, due to repeated load. We measured the change in the attenuation of the built-in optical fiber using instruments commonly used in telecommunications (optical power meter and OTDR) during low cycle tensile loading of the composite specimen. Our goal was to detect the deformation before the critical condition causes failure, and to develop our method further. Our aim was to show that if the increase in fiber attenuation is greater than allowed, i.e., if the optical fiber is damaged somewhere because the polymer composite is damaged, an externally connected OTDR instrument common in telecommunications can be used to find the defect.

2. Materials and equipments used

The optical fiber used in the experiments was G.652.D single-mode glass optical fiber with an outer diameter of 125 μm and a core diameter of 9 μm (manufactured by Corning) with a perpendicular fiber end design.

We made the composite specimens from two layers of zero and ninety degrees woven (orthotropic) prestressed glass fabric (300 \pm 5 % g/m², RT 300 N, Kelteks). Between the two layers, we threaded a 140 mm long section of the 3 m long optical fiber. The optical fiber was guided out of the specimen in front of the grips of the tensile machine so that the grips did not directly load the optical fiber.

The optical fiber proved to be very vulnerable at the exit and entry points of the composite because after manual lamination, the resin surrounding the fiber area made the fiber very stiff and rigid. To avoid fiber breakage, we only removed the 250 μm lacquer layer of the fiber (for mechanical protection) in the middle of the threaded fiber over a 100 mm section, leaving a 20 mm lacquered section on each side of the built-in fiber. The specimen was reinforced with additional reinforcing fabric as a clamping tab beyond the built-in optical fiber section (beyond 140 mm). The specimens were not produced independently but were laminated by hand as a single sheet (so that during manual lamination, the fabric layers could be prestressed and would not be creased by the matrix material). Unsaturated polyester resin (AROPOL M105 TB, Ashland SpA) and 1.5 % initiator (PROMOX P200TX, PROMOX SRL) were used as matrix material. After curing at room tempera-

ture for 24 hours, the specimens were cut from the laminated sheet. The specimens were 25 mm wide, 1.3 mm thick, with a total length of 250 mm. Clamping length was 195 mm, and the installed length of the optical fiber was 140 mm. Three specimens were prepared for each test.

We used a fiber breaker (Fujikura, CT-30) and a fiber welding machine (Fujikura, FSM 12 S) to splice the optical fiber. We connected light with a wavelength of 1550 nm (AFL Telecommunications, from a FlexScan FS-200 light source) at one end of the optical fiber. We examined the change in attenuation at the other end of the fiber with an optical power meter and OTDR instrument with a resolution of 0.01 dB (AFL Telecommunications, FLX380-304 FlexTester OTDR).

We loaded the composite specimens with the built-in optical fiber in a tensile machine (Zwick, BZ050 / TH3A), and the strain was calculated from the crosshead displacement (as a quotient of the crosshead displacement and the initial clamping length). The optical power meter does not have a data logger, but the display shows the current attenuation value. To assign these values to the measured displacement and force, the values displayed by the tensile machine software and the display of the optical power meter were recorded on video (Figure 1.). With the help of these recordings, the attenuation values could later be assigned to the values recorded by the tensile machine.

3. Results and discussion

3.1. Effect of cyclic tensile load

We examined the change in the attenuation of the built-in optical fiber on 3 specimens during cyclic tensile loading starting from zero load. The attenuation of the optical fibers built in the specimens after gripping was nearly 0 dB. In the tests, the loading and unloading speeds were set to be 1.5 mm/min with an increasing max. displacement of 0.1 mm per cycle. In the case of one specimen, the measured values are shown in Figure 2 and 3.

Our results show that the change in the strain and attenuation of the optical fiber can be related, which can be described by a quadratic function with a coefficient of determination greater than 94 % (indicated by the dashed line in Figure 3.) This indicates that the measurement of the altered attenuation is suitable for the detection of strain.

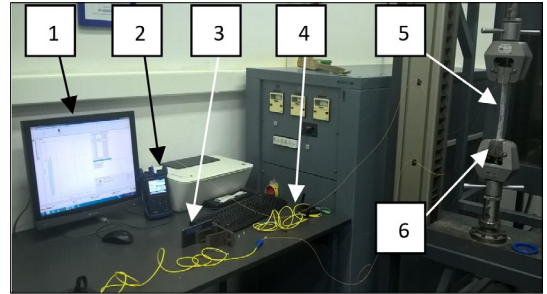


Figure 1. Measurement layout (1-measured displacement and force values, 2-optical power meter, 3-video camera, 4-optical fiber, 5-composite specimen, 6-tensile test machine gripper).

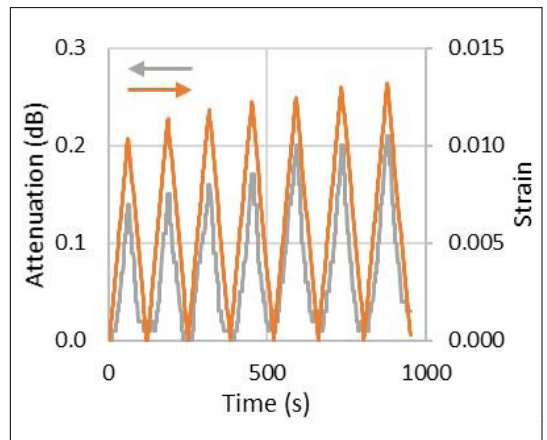


Figure 2. The change of attenuation and strain as a function of time during cyclic tensile loading.

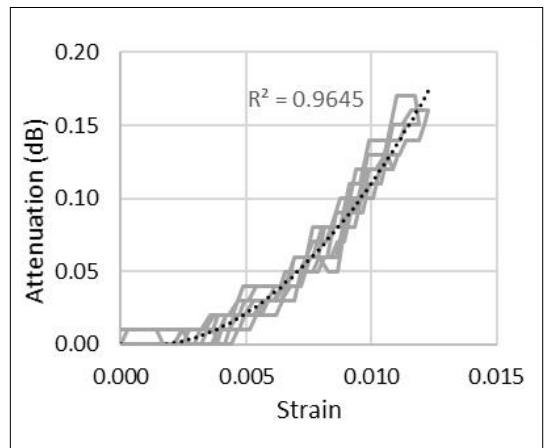


Figure 3. Attenuation of the optical fiber as a function of strain during cyclic tensile load.

Figure 4 summarizes the change in attenuation as a function of strain.

The measurement results show that the attenuation of the optical fiber is closely related to its strain. Higher strain results in higher attenuation. Although the measured attenuation values have a large variance, it can be said that above 1 % strain, the change in the attenuation of the optical fiber is greater than 0.1 dB. This method does not allow accurate strain measurement, but with the help of the changed attenuation of the fiber, the deformation state of the composite element can be categorized: below 0.1 dB attenuation change, the composite is in good condition, while above 0.1 dB attenuation change, it is expedient to test the condition of the composite with additional methods.

In previous tests, a 140 mm long fiber section was built into the specimens and (ideally) the installed section was fully loaded. In our next series of experiments, we investigated the effect of more than one loaded section of the optical fiber.

3.2. The effect of cyclic tensile load on more than one loaded section of the optical fiber

To examine several loaded sections of the optical fiber, we clamped 2 specimens side by side in the tensile machine and pulled the specimens together (in a similar layout as shown in **Figure 9.**). The optical fibers built into the loaded specimens were welded together with a 10 m long optical fiber (the specimens were connected together with $1,5 + 1,5 + 10 = 13$ m unloaded optical fibers). With this layout, we were able to load a built-in optical fiber at several points. The length of the loaded optical fiber was 2×140 mm. Loading and unloading were performed in the same way as in the previous series of experiments, at a speed of 1.5 mm/min, with an increasing maximum displacement of 0.2 mm per cycle. The test was stopped during the 5th cycle and the OTDR was used instead of the optical power meter (the result of this test is presented in Chapter 3.4.). After the test was performed with the OTDR, the optical power meter was reconnected to the optical fiber and the test was continued. In cycle 7, the built-in optical fiber was torn and the optical power meter showed an attenuation of over 40 dB. At this time, the OTDR was reconnected to it (see Chapter 3.4.). The torn optical fiber was illuminated with visible light, too. The results are presented in Chapter 3.3. **Figures 5** and **6** show the test results. The attenuation measured during the test as a function of strain is shown in **Figure 7.**

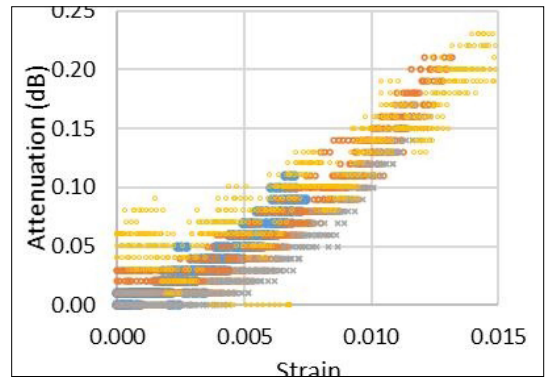


Figure 4. Attenuation measured during cyclic tensile loading as a function of strain (values measured for different specimens are marked with different colors).

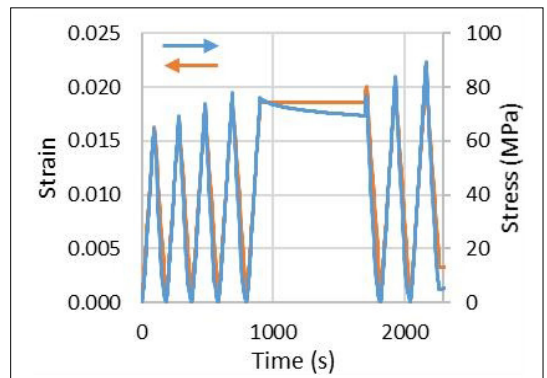


Figure 5. Strain and stress as a function of time measured during the testing of a built-in optical fiber loaded on a 2×140 mm long section (stopping the test for testing with the OTDR is identifiable in the figure).

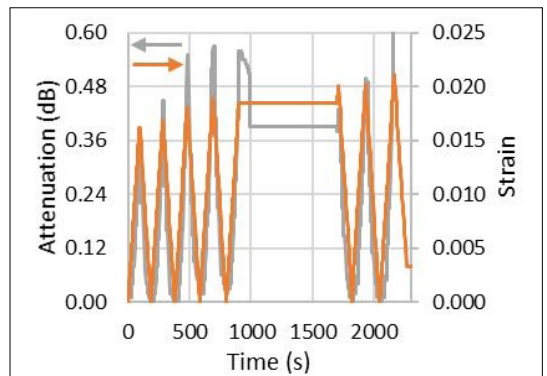


Figure 6. Attenuation and strain as a function of time measured during the testing of a built-in optical fiber loaded on a 2×140 mm long section (stopping the test for testing with the OTDR is clearly identifiable in the figure).

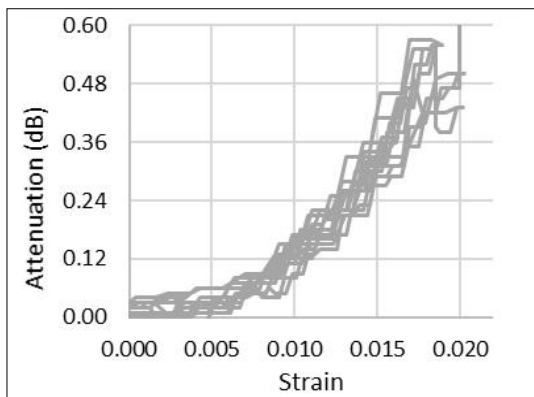


Figure 7. Change of the attenuation of the built-in optical fiber loaded at 2×140 mm as a function of strain.

The attenuation change of the optical fiber as a function of strain is bigger than observed in the previous series of experiments, which is clearly due to the greater length of the loaded fiber section. The optical power meter detects the amount of change in attenuation on both 140 mm loaded sections of the optical fiber.

The results show that the length of the loaded fiber section must be known so that the deformation state of the tested composite part can be determined based on the attenuation change of the optical fiber. If an optical fiber is loaded in several places, the magnitude of the loads cannot be deduced separately with the optical power meter. If a large deformation in the vicinity of the optical fiber breaks the fiber, it can be detected with the optical power meter, but other additional tests are needed to determine the location of the failure, which will be examined below.

3.3. Determining the location of the large deformation using visible light

Experiments with the optical power meter show that the attenuation of the built-in optical fibers changes as a result of the strain of the composite. The light attached to the fiber is absorbed and scattered due to the strain of the fiber. When the composite specimen is highly elongated, the optical fiber may be broken. In the event of a fracture of the fiber, light exits the fiber at the point of failure. The illumination wavelength of the optical power meter falls in the infrared radiation range, which is not visible. The exit of visible light from the fiber at the point of fracture can be identified, a phenomenon that may be suitable for locating the damage (Figure 8.).

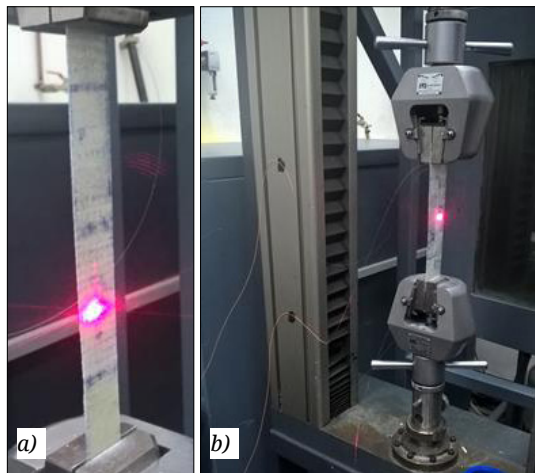


Figure 8. Visible light emitted at the point of fracture in the case of one (a) and two (b) gripped specimens.

3.4. Determining the location of the large deformation using OTDR

The results so far indicate that the deformation of the environment of the optical fiber results in a change in the attenuation of the fiber. We aimed to investigate whether the location of the large deformation in the composite structure can be detected with the help of an OTDR, which is also used in the inspection of telecommunication networks. Widespread commercial OTDR instruments for testing telecommunication networks are not suitable for continuous monitoring, as it takes a relatively long time to analyze and evaluate the measured parameters. The method is not ideal for fast, in-situ condition monitoring (evaluation is in the order of minutes), but may be a suitable complement to the previously presented attenuation measurement in a periodic condition check. By examining the built-in optical fiber, the method may be suitable for detecting large deformations of the composite in the vicinity of the optical fiber and for determining the location of the deformation. To prove this theory, we stopped the movement of the crosshead of the tensile test machine under tensile load (Chapter 3.1) when the optical power meter showed a significant jump in the attenuation of the built-in optical fiber (above 1 dB, which indicates a strain of more than 0.8 % in each case). We detached the end of the optical fiber from the optical power meter and reconnected it to the OTDR using the measurement layout shown in Figure 9.

Due to the dead zone of the OTDR, a 150 m optical fiber was connected after the instrument, and the optical fiber built into the composite specimen was attached to it with an optical connector. We connected an optical fiber approximately 200 m long to the other end of the built-in optical fiber, to avoid the reflections from the end of the fiber, followed by an additional 100 m long optical fiber wound with a small radius. With the OTDR, we examined the attenuation along the length of the built-in optical fiber at 1310 nm and 1550 nm. The OTDR can identify the location and value of each jump in attenuation with an accuracy of 0.1 m and 0.01 dB. The evaluation software tries to identify these jumps with the types of equipment and failures that occur in the optical networks. These elements cannot be interpreted in the examination of composites, but the location and value of the longitudinal attenuation change can be easily observed. The attenuation and distance measured with the OTDR on the unloaded specimen are shown in [Figure 9](#).

The tensile test of the specimen shown in [Section 3.1](#). was stopped at an attenuation value of ~20 dB, and the OTDR was connected as described above. The measured values are shown in [Figure 10](#) and [11](#).

From the graph obtained from the measurement, it can be seen that between the two optical connectors (marked with numbers 2 and 3 at the bottom of [Figure 11](#).) of the built-in optical fiber, the OTDR measured a considerable increase in attenuation. This increase is due to the load of the composite specimen into which the optical fiber is built. The OTDR instrument measured an attenuation of 15.2 dB at 1310 nm and 12.8 dB at 1550 nm at the fiber length of 150.7 m. Contrary to expectations, the attenuation change in the specimen caused by the tensile load is not separated in the graph from the protrusion caused by the optical connector, which shows the disadvantage of measurement with an OTDR. The OTDR cannot detect the location the deformation causing a large attenuation change with an accuracy of cm.

We also gripped and pulled two specimens together to observe the behavior of the multi-point loaded optical fiber and the possibility of examining it with OTDR. Two optical fibers built into the loaded specimens were welded together with a 10 m long optical fiber (the specimens were connected with 1.5 m + 1.5 m + 10 m = 13 m unloaded optical fibers). The measurement layout and the results are shown in [Figure 12](#), [13](#) and [14](#).

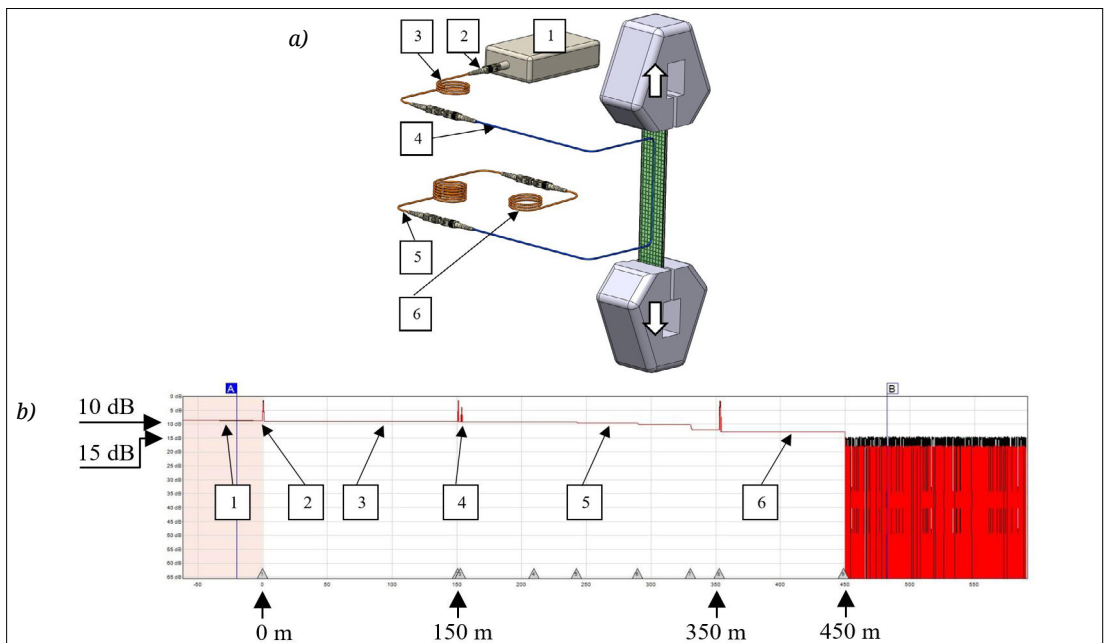


Figure 9. OTDR measurement layout (a) and the values measured with the OTDR on the unloaded specimen (b) (1 - OTDR, 2 - optical connector, 3 - 150 m long ballast fiber, 4 - 3 m long optical fiber with a 140 mm long section built into the composite specimen, 5 - 200 m long optical fiber, 6 - 100 m long optical fiber wound with a small radius to eliminate reflection).

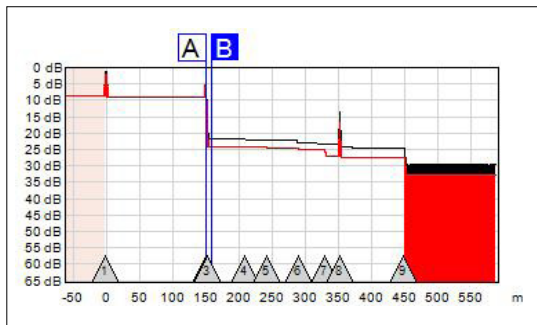


Figure 10. The software of the OTDR identifies the different attenuation-points with numbers marked at the bottom of the figure.

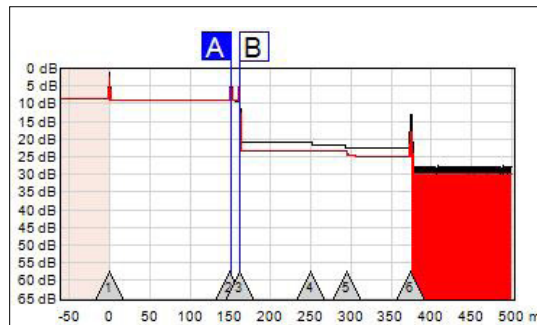


Figure 13. OTDR measurement graph of the fiber loaded in the two gripped specimens.

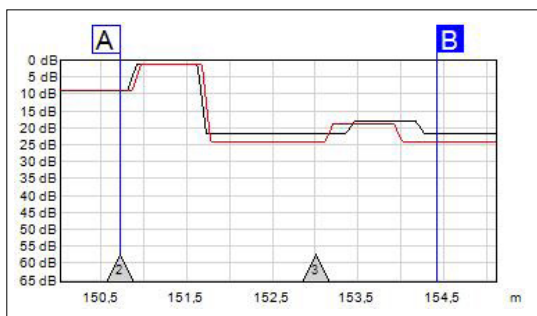


Figure 11. Diagram of OTDR measurement at the attenuation drop measured on the loaded specimen, section A-B of Figure 10 enlarged.

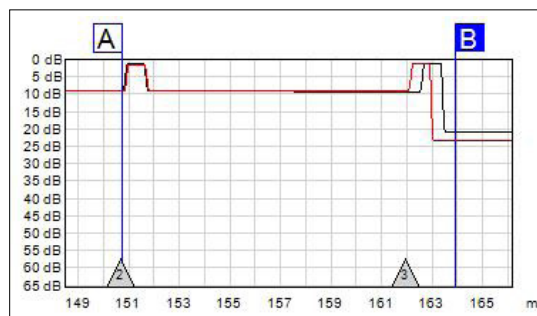


Figure 14. A detail of the OTDR measurement graph of the fiber loaded in the two gripped specimens.

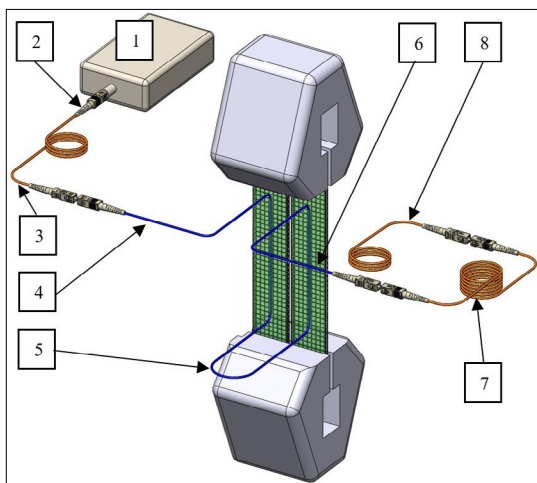


Figure 12. Measurement layout with two clamped test pieces (1 - OTDR instrument, 2 - optical connector, 3 - 150 m long ballast fiber, 4 - 1.5 m long fiber section leading to the test piece, 5 - 13 m fiber section connecting the test pieces), 6 - 1.5 m long fiber section exiting the specimen, 7 - 200 m long optical fiber, 8 - 100 m long fiber wound with a small radius to eliminate reflection).

Only two protruding peaks appear on the graph drawn by the OTDR software, and they do not show the same attenuation change either. The nature of the instrument developed for optical networks is well demonstrated in this measurement. In this case, the instrument was no longer able to distinguish the mechanical optical connectors, they were no longer displayed on the graph, and the software was not able to properly evaluate the attenuation change measured at each point. The instrument measured 15.6 dB attenuation at 1310 nm at the location marked with signal line “A”, but did not indicate this on the graph. At this length, in reality, one of the loaded specimens had a built-in optical fiber section and the OTDR regarded the 15.6 dB attenuation change as caused by the tensile load on the specimen. At mark “B”, the device measured 14.3 dB of attenuation at 1310 nm and at 162.0 m, and also showed this on the graph.

The results showed that the OTDR is able to detect and distinguish several loaded sections of a single optical fiber, it can measure their attenuation changes and their location with an accuracy of a few decimeters. However, these sections may

be incorrectly identified by the software, so when the results are evaluated, it needs to be considered that the software was developed specifically to assess the quality of optical networks.

4. Conclusions

Although originally the optical power meter and the OTDR are used to check the quality of telecommunication optical networks, for a more general purpose, the method presented may be suitable for in-situ condition monitoring of polymer matrix composite materials and detect the presence of deformation prior to critical failure. The cost-effectiveness of the method is ensured by the devices used, since both glass optical fibers and the optical power meter are an easily accessible device nowadays.

Our results show that the attenuation of a single-mode optical fiber built into a polymer composite changes as a function of strain. After the non-damaging load ceases, the attenuation of the built-in optical fiber returns to its initial, unloaded value. The method is able to indicate the strain of the composite structure above 1 % before it reaches a strain causing damage to the structure. Knowing the loaded length of the section of the built-in optical fiber, the strain state of the composite structure can be categorized on the basis of its attenuation change: proper, or requiring additional testing. In the case of a built-in optical fiber section of a given length, the maximum attenuation change at which the strain of the composite does not exceed 1 % can be determined; in the case of a larger attenuation change, the strain of the composite should be tested by additional measurement. The reason for the attenuation change is that the optical fiber is adhesively bonded to the matrix of the composite, and thus the optical fiber also deforms as the composite deforms, which reduces the light transmittance of the fiber, i.e., increases its attenuation.

We have shown that the attenuation change due to the deformation of the optical fiber built into a composite specimen can also be identified with an OTDR. The OTDR is not suitable for in-situ analysis, but may be a suitable complement to measurement with an optical power meter. With the help of the OTDR, the location (or locations) of the deformation causing the large attenuation change within the optical fiber can be determined with an accuracy of half a meter. The differently deformed locations can be separated from each other if there is a suitable length unloaded section (~ 3 m) between them, otherwise the measuring instrument will not be able to separate them.

Acknowledgments

This work was supported by the National Research, Development and Innovation Office, Hungary (NKFIH) [OTKA K 116070 and K120592; NVKP_16-1-2016-0046; and 2017-2.2.4-TÉT-AT]; the Higher Education Excellence Program of the Ministry of Human Capacities, Hungary in the framework of the Nanotechnology research area of the Budapest University of Technology and Economics, Hungary [BME FIKP-NAT]; and the National Research, Development and Innovation Fund, Hungary [TUDFO/51757/2019-ITM, Thematic Excellence Program].

The authors wish to thank András Nagy, Péter Dobos and Zsolt Szabó (ATL Kft.) for their help in performing the measurements.

References

- [1] Kovács L., Romhányi G.: *Derivation of Ply Specific Stiffness Parameters of Fiber Reinforced Polymer Laminates via Inverse Solution of Classical Laminate Theory*. Periodica Polytechnica Mechanical Engineering, 62. (2018) 158–164. <https://doi.org/10.3311/PPme.11846>
- [2] Maamar D., Zenasni R.: *Optimization of Safety Factor by Genetic Algorithm of Circular Notched Carbon / Epoxy Laminate at Low Velocity Impact*. Periodica Polytechnica Mechanical Engineering, 62. (2018) 218–225. <https://doi.org/10.3311/PPme.12041>
- [3] Sethy D., Makireddi S., Varghese F. V., Balasubramaniam K.: *Piezoresistive behaviour of graphene nanoplatelet (GNP)/PMMA spray coated sensors on a polymer matrix composite beam*. Express Polymer Letters, 13/11. (2019) 1018–1025. <https://doi.org/10.3144/expresspolymlett.2019.88>
- [4] Krawczak P.: *Polymer composites: Evolve towards multifunctionality or perish*. Express Polymer Letters, 13/9. (2019) 771. <https://doi.org/10.3144/expresspolymlett.2019.65>
- [5] Konstantopoulos S., Fauster E., Schledjewski R.: *Monitoring the production of FRP composites: A review of in-line sensing methods*. Express Polymer Letters, 8/11. (2014) 823–840. <https://doi.org/10.3144/expresspolymlett.2014.84>
- [6] Glisic B., Inaudi D.: *Fibre optic methods for structural health monitoring*. John Wiley & Sons Ltd., New York, 2007.
- [7] Grattan K. T. V., Meggitt B. T.: *Optical fiber sensor technology*. Springer Science+Business Media, B.V, Dordrecht, 1995.
- [8] MSZ 9620-1:1990: *Fénytechnikai terminológia. A sugárzás alapfogalmai, mennyiségei és egységei*.
- [9] Elliott B., Gilmore M.: *Fiber Optic cabling*. Newnes, Oxford, 2002.
- [10] Chinpon A., Thamaphat K., Hansuparnusorn M., Limsuwan P.: *A force measurement method using*

- the optical fibre beam*. Procedia Engineering, 32. (2012) 989–993.
<https://doi.org/10.1016/j.proeng.2012.02.043>
- [11] Luo F., Liu J., Ma N., Morse T. F.: *Fiber optic microbend sensor for distributed sensing application in the structural strain monitoring*. Sensors and Actuators, A: Physical, 75/1. (1999) 41–44.
[https://doi.org/10.1016/S0924-4247\(99\)00043-6](https://doi.org/10.1016/S0924-4247(99)00043-6)
- [12] Hu H.-F., Sun S.-J., Lv R.-Q., Zhao Y.: *Design and experiment of an optical fiber micro bend sensor for respiration monitoring*. Sensors and Actuators, A: Physical, 251. (2016) 126–133.
<https://doi.org/10.1016/j.sna.2016.10.013>
- [13] Crane R. M., Gagorik J.: *Fiber optics for a damage assessment system for fiber reinforced plastic composite structures*. In: Thompson D.O., Chimenti D.E. (eds) Review of Progress in Quantitative Nondestructive Evaluation. 28. (1984) 1419–1430.
https://doi.org/10.1007/978-1-4613-3706-5_94
- [14] Glossop N. D. W., Dubois S., Tsaw W., Leblanc M., Lymer J., Measures R. M., Tennyson R. C.: *Optical fibre damage detection for an aircraft composite leading edge*. Composites, 21/1. (1990) 71–80.
[https://doi.org/10.1016/0010-4361\(90\)90100-B](https://doi.org/10.1016/0010-4361(90)90100-B)
- [15] LeBlanc M., Measures R. M.: *Impact damage assessment in composite materials with embedded fibre-optic sensors*. Composites Engineering, 2/5-7. (1992) 573–596.
[https://doi.org/10.1016/0961-9526\(92\)90044-7](https://doi.org/10.1016/0961-9526(92)90044-7)
- [16] Hegedűs G., Czigány T.: *Developing a glass fibre sensor for polymer technology applications*. Institute of Physics (IOP) Conference Series: Materials Science and Engineering, 426. (2018) 012015.
<https://doi.org/10.1088/1757-899X/426/1/012015>
- [17] Hegedűs G., Czigány T.: *Analysis of the applicability of optical fibers as sensors for the structural health monitoring of polymer composites: the relationship between attenuation and the deformation of the fiber*. Sensors and Actuators A: Physical, 272. (2018) 206–211.
<https://doi.org/10.1016/j.sna.2018.01.039>

Remaining Lifetime Assessment of Bucket Wheel Excavator's Boom Structure by Using Non-destructive Method

József ANDRÁS,¹ József KOVÁCS,² Endre ANDRÁS,³ Ildikó KERTÉSZ,⁴
 Ovidiu Bogdan TOMUȘ⁵

University of Petroșani, Faculty of Mechanical and Electrical Engineering, Department of Mechanical, Industrial and Transportation Engineering, Petroșani, Romania

¹ *iosif.andras@gmail.com*

² *kovacsi@mail.com*

³ *andrei.andras@gmail.com*

⁴ *kerteszdiko@ymail.com*

⁵ *tobogdan@gmail.com*

Abstract

The bucket wheel excavators (BWE), when operating in faces with hard intrusions (rock structures with increased cutting resistance) are submitted to loads exceeding those arising during the operation in normal conditions. The most vulnerable structural element of the BWE from the point of view of these loads is the boom. The unexpected occurrence of hard formations produces shocks and vibrations, their unwanted effect being sudden failures of the constitutive elements and, in long term, fatigue, which increases the vulnerability of the mentioned structural element. In the paper we present the results obtained regarding the fatigue and remaining lifetime assessment using a new method, issued from the researches performed in the frame of BEWEXMIN project.

Keywords: *bucket wheel excavator, fatigue, lifetime, surface hardness.*

1. Introduction

Using surface hardness measurements on structural elements with a long history of cyclical loading as an indicator of the fatigue state, is relatively new in the analysis of structures.

The representative structures of this approach are mainly metallic bridges, cranes, load-carrying structures of buildings (mainly subjected to seismic loads), pipelines and other mechanical parts, such as gears.

In the past, the load carrying structures of huge earth-moving machines, such as bucket wheel excavators (BWE) became a subject of this approach [1].

It was determined that the fatigue resistance coefficient decrease can be correlated with Brinell Hardness (HB) increase in the case of steel.

Despite the different opinions of specialists regarding the so called cyclic softening-hardening of steels, the hardening process in the vicinity of

zones suffering plastic strain has been confirmed.

The remnant lifetime estimation of a crane's metallic structure using nondestructive methods is treated in [2]. The paper [3] deals with the remnant lifetime determination of mining equipment parts based on hardness increase. Underwater structures, such as steel pipes fatigue correlation with surface hardness change is presented in [4], while in [5] a hardness based method is presented for the lifetime evaluation of metallic bridges.

There are many published theoretical approaches, not all showing the direct correlation of hardening with the number of loading cycles. Such a correlation between the fatigue resistance coefficient (fatigue ratio) and Brinell Hardness has been statistically determined as in Figure 1. [6]

The increase in hardness discussed in this paper, depending on the number of repetitive load cycles (determined on the basis of operating time), was found to have compared the increase in hardness

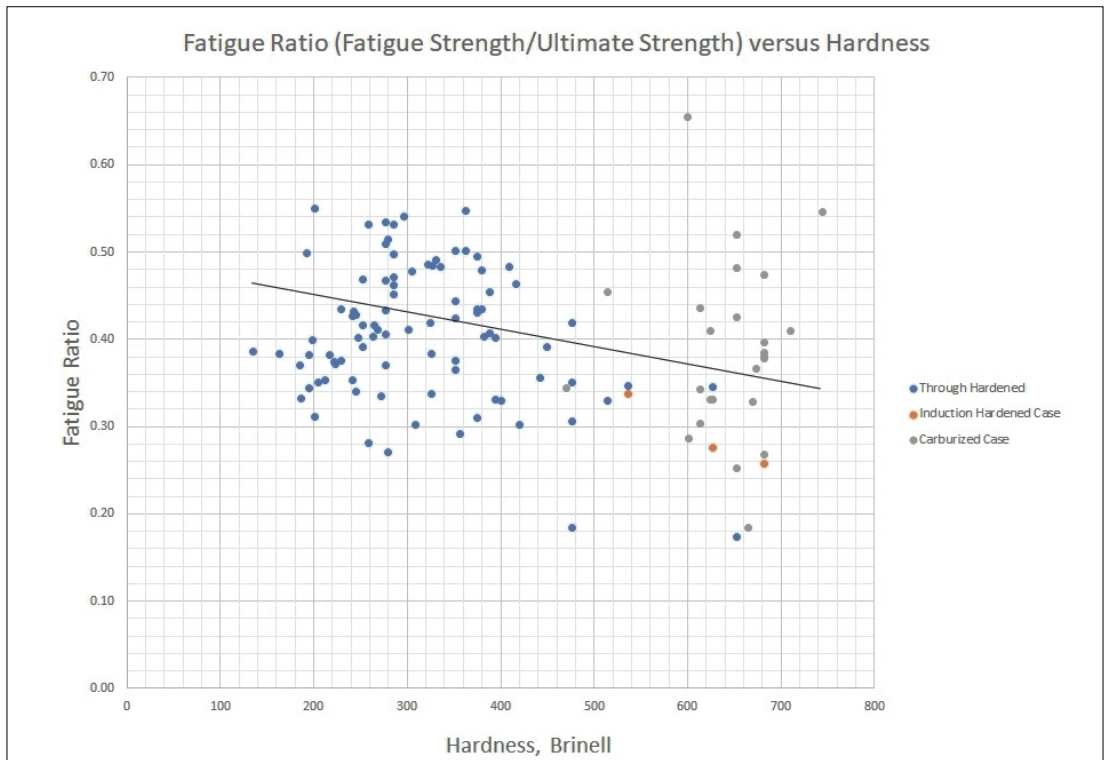


Figure 1. Brinell hardness increase with fatigue resistance coefficient decrease, according to [6].

measured on samples collected from the critical points of the excavator's boom structure, with original steel samples of the same brand, which were subjected to near the breaking tensile stress,

The average Brinell Hardness variation of samples collected from BWE boom elements related to samples made from the same kind of steel, in the original state, has been plotted, according to [Figure 2](#).

The hardness relative increase is significant, leading to the conclusion that the hardness can be

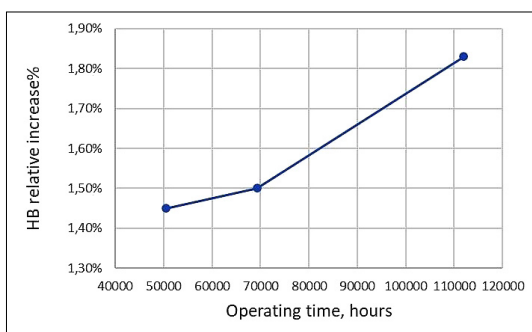


Figure 2. Brinell hardness relative increase as a function of operating hours.

considered as an indicator of fatigue resistance, i.e. for the assessment of the remaining lifetime of the structure in case.

2. Material and method

In our approach, three types of measurements were considered, as follows:

- Joint hardness and tensile strength measurements on samples made by the same kind of steel as the BWE boom elements, revealing an increase of surface hardness increase in the proximity of breakage relative to the hardness in the body of the sample;
- Hardness and strength measurements on samples obtained from the BWE boom members, which were replaced during renewal of the respective structural element after failure;
- In situ hardness measurements on selected points of constituent elements of the boom, using a portable non-destructive Krautkramer MIC 20 hardness measurement device, the points being selected on the basis of FEM analyses and fault history of the given BWE.

We extended the hardness measurement on a batch of 7 machines – type ERc1400-30/7 – from

different open pits from the Oltenia coal basin, on the same subassembly, and the bucketwheel boom.

In **Figure 3** the average hardness has been plotted in correlation with the age of service of different BWE -s from which the samples were collected.

It can be observed that the general trend of HB is increasing, the last point value is due to the fact that the steel is of another kind than the rest of the BWE-s, other deviations are due to the averaging and different load history (less operating hours at same age).

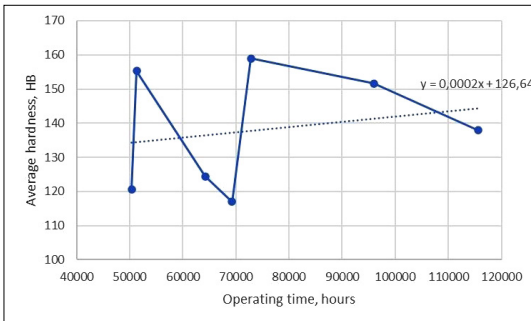


Figure 3. Evolution of average hardness according to operating time.

Nevertheless, the differences of hardness between different elements of the boom structure can provide useful information about the fatigue level of different structural parts, for the identification of those in which the probability of expected failures is greater.

We performed the hardness measurement on two machines type E 1400-307, 07 and 08, from the same open pit, under approximate temperature and excavation conditions to assess the hardness for which the structural properties of the materials are close.

From **Figure 4** we can find that on average the decay of properties is not affected by the operating time between excavators, but there is a clear difference between left and right wall (girder).

Also, the graphs indicates a difference between the joints (nodes) which shows an asymmetry between left and right and a concentration of hardening at the extremities of the boom relative to middle segment.

This fact, along with correlation with other analyses can be useful for deriving a complex, multifactorial discrimination method for detecting the most vulnerable parts of the boom.

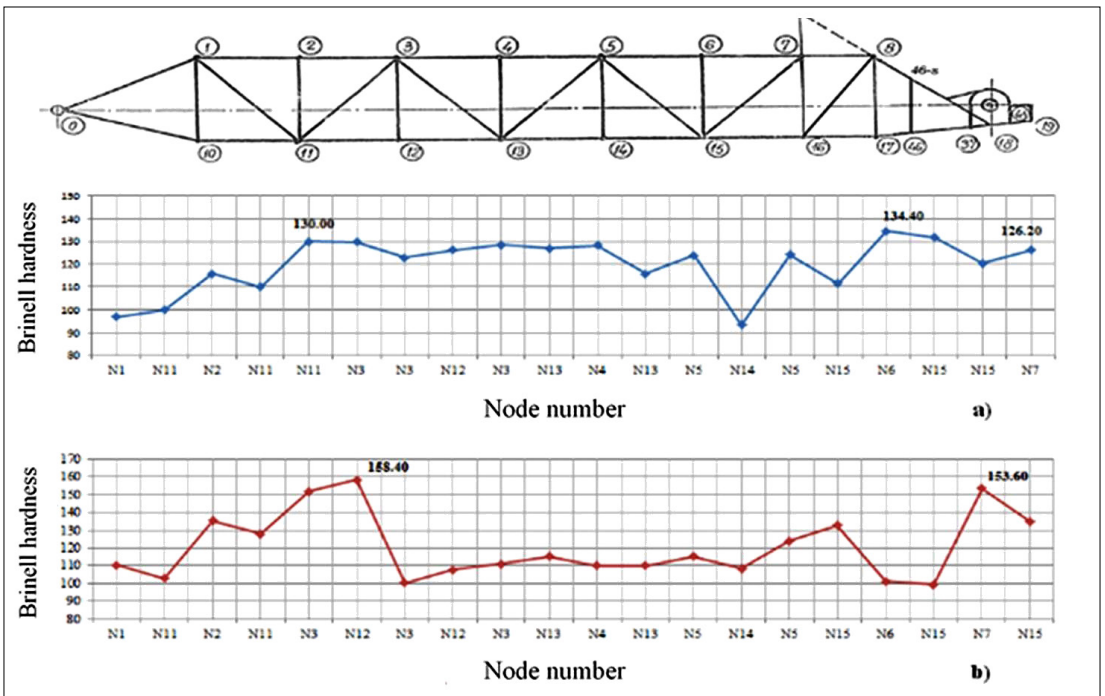


Figure 4. Distribution of the measured hardness on boom nodes.

3. Influence of the age of BWE on faults frequency

The carrying structure of the BWE suffers in time degradation by fatigue that affects the functionality of these machines, degradations that can be generated mainly by decrease of fatigue resistance of materials.

The degradations that may occur over time on mobile heavy-duty machinery may be disposed of in the form of punctual charts of type defects for these machines. These charts have been drawn up after conducting the technical expertise of 25 machines used in lignite open pits

In **Figures 5** and **6** different correlations between operating hours, failures occurred, throughput, rate of failure and production rate are presented.

By correlating the fault intensity with hardness growth, we can forecast the expected faults number dependence in terms of the average hardness, as in **Figure 7**.

4. Conclusion

Hardness based mechanical properties decay analysis is a useful method of investigating the change in structural features of mining machinery, and it can provide some information on the properties that evolve over time in the components of the load-carrying structure of the machine.

The hardness relative increase with the duration of service is significant, leading to the conclusion that the hardness can be considered as an indicator of fatigue resistance, i.e. for the assessment of remaining lifetime of the structure in case.

Different correlations between operating hours, failures occurred, throughput, rate of failure, production rate were derived, which are useful for state monitoring of the BWE carrying structure.

By correlating the fault intensity with hardness growth, it is possible to forecast the expected faults number dependence on the average hardness.

The differences of hardness between different elements of the boom structure can provide useful information about the fatigue level of different structural parts, for the identification of those in which the probability of expected failures is greater, which is useful for deciding the sensor placement location for state monitoring.

The results, in correlation with other analyses can be useful for deriving a complex, multifactorial discrimination method of detecting the most vulnerable parts of the boom.

The method presented is a new way to assess the state of the BWE-s and to forecast the remaining lifetime reserve.

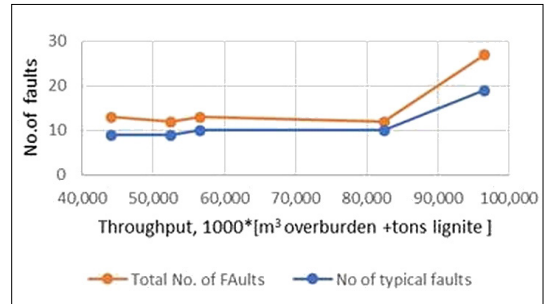


Figure 5. The number of failures according to the extracted lignite and overburden rock.

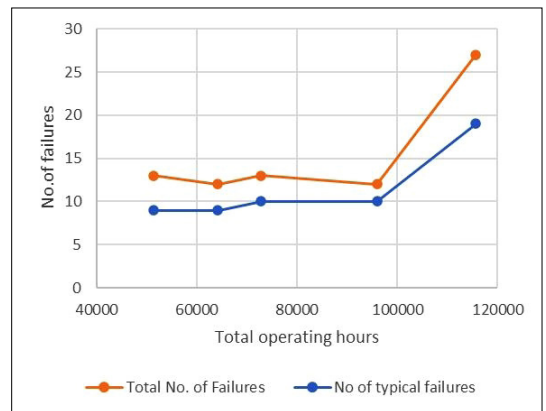


Figure 6. The number of failures according to operating hours.

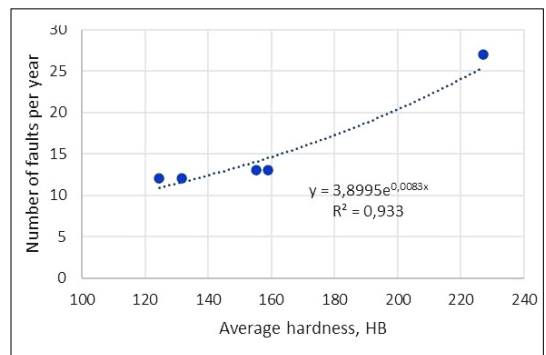


Figure 7. Correlation between fault intensity and hardness.

References

- [1] Boskovic S., Jovancic P., Ignjatovic D. et al.: *Vibration as deciding parameter during revitalization process for replacing the bucket wheel drive*. Journal of Vibroengineering 17/1. (2015) 24–32.
<https://www.jvejournal.com/article/15632>
- [2] Vilceanu F., Radu S. M.: *Methodology of establishing residual lifetime of lifting installation by non-destructive methods*. 6th International Multi-disciplinary Scientific Symposium, Universitaria Simpro 2014, 10-11 october 2014, Petroșani.
- [3] Zvonarev I. E., Ivanov S. L.: *Analysis of changes in hardness of a metal surface layer in areas of high stress and methods of determining residual life of parts for mining machines*. IOP Conf. Series: Materials Science and Engineering, 116 (2016) 012006
<https://doi.org/10.1088/1757-899X/116/1/012006>
- [4] Drumonda G., Roudetb F. I.: *High cycle fatigue damage evaluation of steel pipelines based on microhardness changes during cyclic loads*. 23^{ème} Congrès Français de Mécanique Lille, 28 Août au 1^{er} Septembre 2017.
- [5] Chaminda S. Bandara, Sudath C. Siriwardane, Udaya I. Dissanayake and Ranjith Dissanayake: *Hardness-Based Non-destructive Method for Developing Location Specific S-N Curves for Fatigue Life Evaluation*. Journal of Civil Engineering and Architecture 10. (2016) 183–191.
<https://doi.org/10.17265/1934-7359/2016.02.007>
- [6] *Hardness versus Fatigue Strength*, August 8, 2017 by Steel Market Development Institute
<https://barfatigueblog.org/2017/08/08/hardness-versus-fatigue-strength/> (accessed on: 15. 05. 2019.).

Damage Analysis of Tattoo Needle Tips

Lilla ASZTALOS,¹ Borbála LEVELES²

Budapest University of Technology and Economics, Faculty of Mechanical Engineering, Department of Materials Science and Engineering, Budapest, Hungary

¹ lilla@eik.bme.hu

² levelesb@gmail.com

Abstract

Tattooing is becoming more and more accepted at different levels of society today. A contributor to this is that besides body decoration, the cosmetics industry is increasingly using it for make-up tattoos and to hide skin imperfections and surgical scars. Tattoo needles, despite being in direct contact with human tissues and even with blood, are not subject to current Medical Device Regulation, so they do not require a number of material and biocompatibility tests in order to be placed on the market. The focus of our research was on how the needle and the soldering of the needles are damaged during tattooing, and how this develops over time, as a worn needle tip can not only degrade the quality of the tattoo, but also increase skin breakdown and the amount of dissolving allergenic substances.

Keywords: *tattoo needle, damage, needle wear.*

1. Introduction

Tattoos are created by piercing tiny needles at a frequency of 50–3000 Hz into the skin. The needles then break through the surface of the skin and introduce the dye into the skin's dermis layer (min. 1.2 mm deep). The tattoo dye is perceived by the skin as a foreign substance and initiates macrophage cells to destroy the dye, however, after ingestion of the dye, the cells get stuck with the dye in the skin matrix. After 2–3 weeks of creating the tattoo, the colours fade, as the tattoo also gets dye in the upper epidermis, which wears out over time as the cells die and regenerate. Over the years, the tattoo also fades as the dye in the skin is gradually broken down by the immune system [1–3].

1.1. Needle tip damage

Needle tip destruction is typically studied in medical applications such as injection needles or thicker needles used in epidural anaesthesia. The tip of the spinal needle is often damaged during the latter, especially when the spinal cord puncture needs to be repeated several times into the bone or cartilage due to failure, so it is of primary

interest for us to examine these. [4–6]. Because these are all disposable needles, they remain intact or slightly deformed after a puncture. In clinical practice, some research groups examined Quincke-type needles used for epidural anaesthesia and found that four percent of the needle tips were clearly bent and 11 % were slightly bent based on scanning electron micrographs. Needles in contact with the bone caused clear tip damage in 7 %, and 99 % of the needles remained intact or slightly bent in the case of penetration without bone contact. In conclusion, the tips of disposable needles are suffer more damage in contact with hard tissue (bone) than after penetration into soft tissue [4, 7].

Like injection needles, thin tattoo needles suffer small but permanent damage after contact with the skin. The longer a needle used, the more the tip becomes blunted, which causes more pain during use, and bacteria are better able to adhere to surface damage, which also increases the risk of infection [8–10]. The study of this destruction is worth a closer look, as it can also cause unwanted damage to the skin surface, and the tattooing process can be more painful. The dullness of the nee-

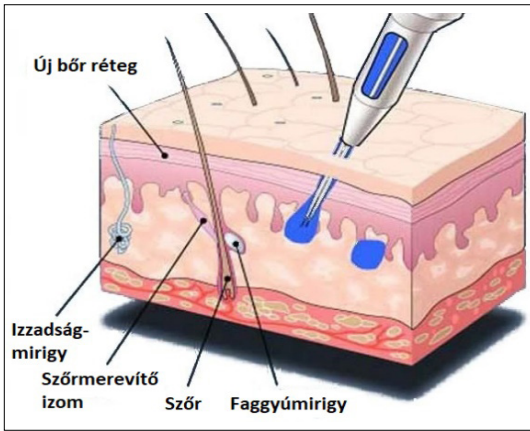


Figure 1. Tattooing process.

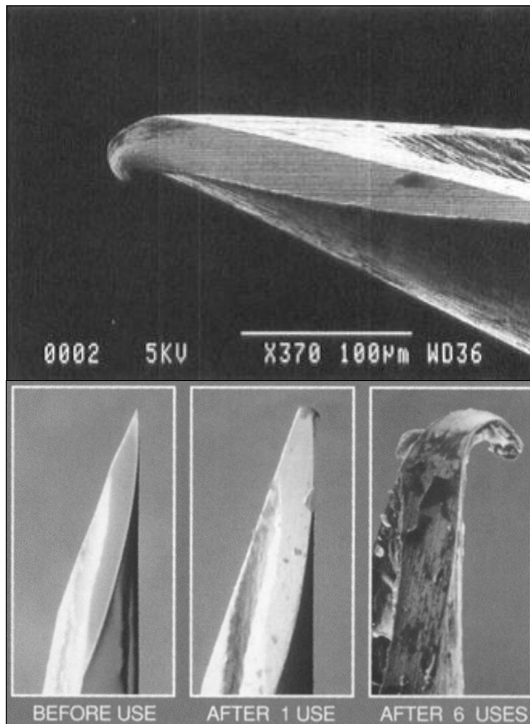


Figure 2. Abrasion of needle tips used for epidural anesthesia [4].

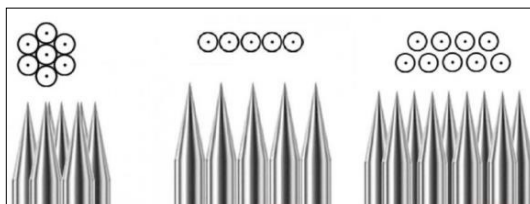


Figure 3. Tattoo needle arrangements. From left to right: round, flat and magnum layout.

dle tips also leads to a deterioration in the quality of the tattoo, so it should be replaced consistently, over a period of time or after the tattooed surface. To avoid this, we aimed to examine how long generally – or after a tattoo – it is advisable to replace the needle tip so that maximum utilization is achieved. Of course, at the beginning of each new tattoo, the artist must use a new, sterile needle, for hygiene reasons.

2. Methods

2.1. In vivo damaged needles

To examine the needle tips, we used 13 round arranged tattoo needles pierced in areas of 30–100 mm². Each needle was used to make a tattoo using the handpoke (freehand tattoo) method, meaning that the needles were not moved by machine, but were inserted into the skin by hand. After use, the dried paint and impurities were removed with an ultrasonic vibrator, ethyl alcohol, and acetone, but still remained in the wells. In addition, 2 unopened, sterile needles were examined as a reference. These needles are individually soldered in different numbers, there are also 3-5-9 pieced ones in three different arrangements (Figure 3.). After cleaning, the needles were examined by stereo microscopy, and then scanning electron microscopy (SEM) images of the tips and soldering were taken to see how much they had cracked during use.

2.2. Modeling the tattooing process in an in vitro environment

As it is difficult to determine the period of use and the compressive force of hand-used needles, it was advisable to devise a standardized measurement method to set the wear time of the needles. For the first experiment, we handmade samples on the so-called training skin used by tattooists, and then in order to make the abrasion process as even as possible per unit of time and for easier feasibility, we mounted a two-roll tattoo device from the brand Horizon to a Yamaha LCM100 linearly controlled robot in the BME ATT laboratory (Figure 4.). The manual tattooing process was performed for 30 min and the automated process for 30, 60, and 90 min. The power supply was set to a specific frequency, to a value between 50 and 60 Hz determined from high-speed camera recording. This represents about a hundred thousand insertions of with a needle that has been running for 30 minutes.

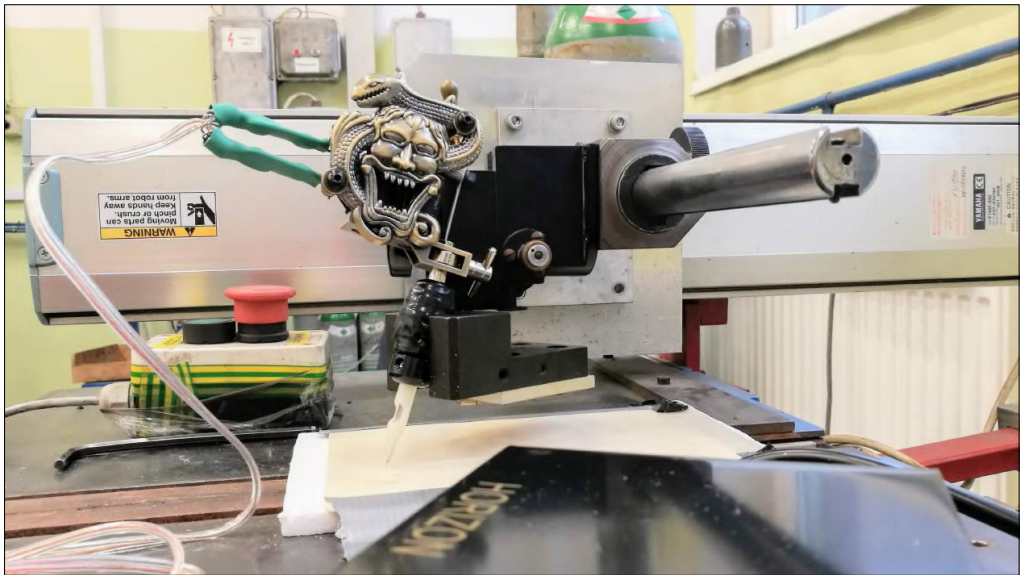


Figure 4. Equipment used for the automation of the tattooing process.

3. Results

3.1. In vivo damaged needles

Scanning electron microscopy (Zeiss EVO MA10) images provide the most information on needle tip destruction and detachment rates. Strong wear of the needle tips was observed in the samples, the tips of almost all members of the needle group were plastically deformed (**Figures 5–7**).

Material composition analysis was also performed by energy dispersive X-ray spectrometry (EDAX Metek Elect Plus). As a result of the study, it was found that the material of the needles is not made of 316L commercially marked austenitic stainless steel, but of a more general, not very biocompatible alloy, 1.4301 steel. The stress of stabbing the skin is abrasive, the wear properties of these steel types are not outstanding [11, 12]. Poor wear resistance in medical devices is unfavourable, as particles detached during the wear process can cause irritation if they enter the body, especially the two main alloys of the steel type: chromium and nickel [13].

3.2. In vitro experiments

At lower magnification stereo and electron microscopy images, there is almost no damage to the needle ends. Even at higher magnification, the needles on the training skin showed dulling only on the needle tips used by hand, and with the result shown in **Figure 8**, no significant damage could be observed on the needles used with the

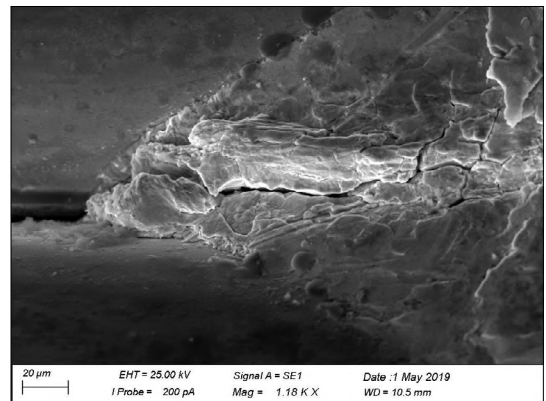


Figure 5. Damage on the soldering of the needle groups in in vivo case.

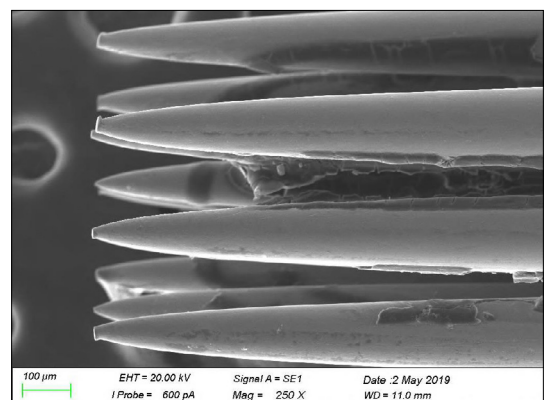


Figure 6. Significant wear was observed in almost all of the needle groups in the in vivo case.

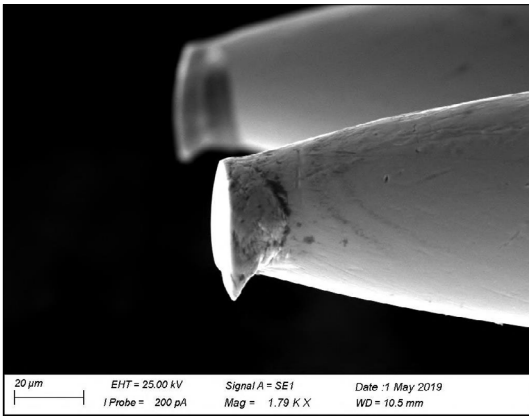


Figure 7. Electron micrograph of a worn needle tip at higher magnification.

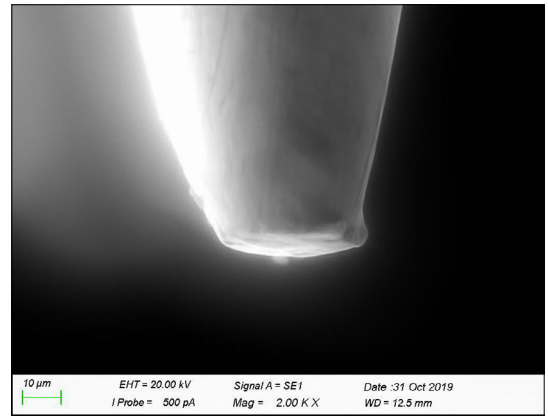


Figure 8. In vitro needle damage in case of hand-made process.

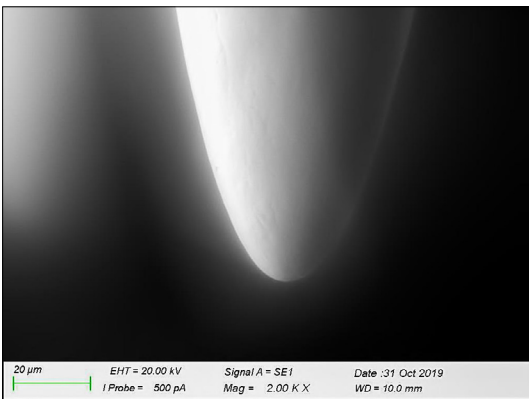


Figure 9. In vitro needle damage in the case of an automated tattoo process on training skin.

linear welding robot, regardless of the duration of the run (Figure 9.). The training skin is made of silicone and is much softer to the touch than real skin, which may have caused the results of real-world tests to differ from those seen in vitro. During the automated tattooing process, however, the soldering of the needles was significantly damaged because the surface of the silicone training skin was easily torn and the needle tips became stuck in it more easily during movement.

4. Conclusions

Our studies have confirmed that the tip of tattoo needles as well as the soldering of the needles suffer significant damage even after short-term use. We have found that the properties of the so-called training skin recommended for tattoo artists differ significantly from the properties of real skin, so it is not applicable in laboratory testing

for damage to tattoo needles. As a continuation of our research, we would perform the method presented here on pigskin to explore the process of needle wear in more detail as a function of the time elapsed with the tattoo.

Acknowledgments

The publication was supported by the Ministry of Human Resources' NTP-SZKOLL-19-066 National Talent Program.

References

- [1] Sad B.: *New technologies for dynamic tattoo art*. Proceedings of the 5th International Conference on Tangible Embedded and Embodied Interaction. 2011. 313–316. <https://doi.org/10.1145/1935701.1935774>
- [2] Serup J., Bäumlér W.: *Tattoo Infections, Personal Resistance, and Contagious Exposure through Tattooing*. Current Problems in Dermatology. Basel, Karger 52. (2017) 30–41. <https://doi.org/10.1159/000450777>
- [3] Sweeney S. M.: *Tattoos: a review of tattoo practices and potential treatment options for removal*. Current Opinion in Pediatrics, 18/4. (2006) 391–395. <https://doi.org/10.1097/01.mop.0000236388.64333.cd>
- [4] Jokinen M. J. et al.: *Deformed spinal needle tips and associated dural perforations examined by scanning electron microscopy*. Acta Anaesthesiologica Scandinavica, 40/6. (1996) 687–690. <https://doi.org/10.1111/j.1399-6576.1996.tb04511.x>
- [5] Sitzman B. et al.: *The Effects of Needle Type, Gauge and Tip Bend on Spinal Needle Deflection*. Anesthesia & Analgesia, 82/2. (1996) 297–301. <https://doi.org/10.1097/0000539-199602000-00014>

- [6] Benham M.: *Spinal needle damage during routine clinical practice*. *Anaesthesia*, 51. (1996) 843–845. <https://doi.org/10.1111/j.1365-2044.1996.tb12614.x>
- [7] Rout P. G. J. et al.: *An Investigation of the Effect on 27-gauge Needle Tips following a Single Local Anaesthetic Injection*. *Dental Update*, 30/7. (2003) 370–374. <https://doi.org/10.12968/denu.2003.30.7.370>
- [8] Kline D., Kuhn T.: *Needle Reuse and Tip Damage*. *Diabetes Care*, 27/2. (2004) 617–617. <https://doi.org/10.2337/diacare.27.2.617>
- [9] Abolhassani N., Patel R.: *Deflection of a Flexible Needle during Insertion into Soft Tissue*. 2006 International Conference of the IEEE Engineering in Medicine and Biology Society. <https://doi.org/10.1109/iembs.2006.259519>
- [10] Kataoka H. et al.: *A Model for Relations Between Needle Deflection, Force, and Thickness on Needle Penetration*. *Lecture Notes in Computer Science*, (2001) 966–974. https://doi.org/10.1007/3-540-45468-3_115
- [11] Barcelos M. et al.: *Wear resistance of AISI 304 stainless steel submitted to low temperature plasma carburizing*. *REM – International Engineering Journal*, 70. (2017) 293–298. <https://doi.org/10.1590/0370-44672016700094>.
- [12] Reza Bateni M. et al.: *Wear and corrosion wear of medium carbon steel and 304 stainless steel*. *Wear*, 260/1–2. (2006). 116–122. <https://doi.org/10.1016/j.wear.2004.12.037>
- [13] Schriever I. et al.: *Distribution of nickel and chromium containing particles from tattoo needle wear in humans and its possible impact on allergic reactions*. *Part Fibre Toxicol*, 16/33. (2019) <https://doi.org/10.1186/s12989-019-0317-1>

The Role of the Material of Active Screen During the Plasma Nitriding Process

Dorina KOVÁCS,¹ Annamária SZABÓ,² Alexandra KEMÉNY³

Budapest University of Technology and Economics, Faculty of Mechanical Engineering, Department of Materials Science and Engineering, Budapest, Hungary

¹ dorina@eik.bme.hu

² annamaria.szabo97@gmail.com

³ alexa@eik.bme.hu

Abstract

In this research the effect of the active screen's material was investigated. 42CrMo4 steel was plasma nitrided with unalloyed steel, titanium and nickel active screen at 490 and 510 °C for 4h in 75 % N₂ + 25 % H₂ gas mixture. Scanning electron microscopy (SEM), energy dispersive spectrometry (EDS) and X-ray photoelectron spectroscopy (XPS) were used for the characterisation of the surface properties. Iron-nitride was not formed on the surface with nickel screen. The evaluation of examination results showed that most of the detected nitrogen was molecular (N₂) in the formed layer.

Keywords: *active screen plasma nitriding, X-ray photoelectron spectroscopy.*

1. Introduction

The nitriding is a type of thermochemical surface treatment in which a hard, wear resistant surface layer can be formed by diffusing nitrogen into the surface which forms nitride with the atoms of the material. Nitrogen, as an interstitial alloy, dissolves in solid solutions of iron and can react and form compounds with certain alloys and constituents of steel [1, 2]. The vibratory motion is increased with the increasing of the nitriding temperature, which allows the diffusion of the nitrogen atoms into the lattice of iron. After the saturation of the solid solution, the nitrogen can create a compound with the iron atoms, which forms a continuous layer with higher hardness than the dissolved nitrogen in the solid solution [3, 4].

The plasma nitriding, also called ion-nitriding, was introduced in the 1920s as a surface treatment. As soon as the gas ionization begins, the ions start to bombard the surface, which also called vaporization, because the precipitation of ions from the metal surface can rip off the atoms and contaminations. After the bombarding, which also serves the cleaning of the surface, the acce-

lerated nitrogen ions heat the workpiece to the nitriding temperature with the controlling of the voltage, then the diffusion of nitrogens into the material and formation of nitrides starts [5–8]. [5–8]. Three different types of plasma nitriding exist: DCPN – direct current plasma nitriding, ASPN – active screen plasma nitriding and ASBPN – active screen biased plasma nitriding. The ASPN was developed to avoid the shortcomings (hollow cathode effect, corner effect) of the other method [9–11].

In ASPN treatment, the plasma is not created on the workpiece, but on a screen (often called as a cage) placed around the workpiece. As a result, at first, the active screen is bombarded by the ionized atoms and their associated positively charged ions. The sputtered iron-ions connect to the nitrogen-ions in the plasma through the screen. From these nitride particles, some of them can be deposited on the surface of the screen, but others due to the surface structure of the screen pass through and adsorb on the sample which is heated by the radiation and the gas inlet and continuous plasma flow maintained by the vacuum pump [11–13].

The active screen is characterized by the surface structure, the distance from the sample and the material, but in this paper, we will present only the effect of the material. Naeem [14] used austenitic stainless steel screen in his research. It was stated from the chemical composition analysis that nickel and chromium were found on the treated sample, which was caused by the deposition of the bombarded active screen. Yazdani et al. [15] nitride aluminium samples with unalloyed steel screen at 550 °C, with 75 % N₂ + 25 % H₂ gas mixture for different time lengths. Fe₃N layer was created on the samples which was formed from the sputtered iron of the screen combined with nitrogen.

Researchers not only pay attention to the plasma nitriding of metals but also for polymers. Polypropylene was nitrided between 5–15 mins to investigate how the process changes the adhesion properties of the surface. It can be observed that after this little time, Fe could deposit on the surface, which came from the active screen [16].

In this study tempered steel was nitrided by unalloyed steel, titanium and nickel coated active screen to investigate how the screen material affects the formation of the nitride layer and what bond can be made with the material of the sample.

2. Experimental details

2.1. Materials

42CrMo4 and Ti-6Al-4V ELI was used as a material which were cut into disks with a 20 mm diameter. The thickness of the samples was 6 mm. The tempered steel was put into the furnace in tempered condition. All samples were ground on P80 to P2500 SiC particle size papers and then polished by a 3 µm diamond suspension. Before the nitriding, it was degreased in an ultrasonic vibrated ethanol bath.

The materials and dimensions of the active screen are seen in Table 1. The samples were placed in the centre of the screen. The screens

Table 1. Materials and dimensions of the active screen

Material	Diameter (mm)	Hole size (mm)
DC01	100	5
Ti 1	100	18
Ti 2	55	6
Ni	100	5

were made by laser cutting. The nickel coating was electroplated in ~70 µm thickness.

2.2. Nitriding parameters

The plasma nitriding treatment was made in self-designed plasma nitriding equipment. The samples were nitrided at 490 °C with unalloyed steel and titanium screen, for 4 hours with 75 % N₂ + 25 % H₂ gas mixture. The nickel coated sample was nitrided for 4 hours at 510 °C with the same gas mixture

2.3. Characterization methods

Stereomicroscopic (Olympus SZX16) images were taken from the upper surfaces of the nitrided samples. The microhardness of the layer was measured by a microhardness tester (Buehler IndentaMet 1105). For the EDS measurement Zeiss EVO MA10 electron microscope with EDAX Z2 detector, for the XPS Phoibos 100 MCD-5 detector were used.

3. Plasma nitriding

The first experiments were made on titanium to analyse the increase of the corrosion resistance, but it was observed that the sputtered particles from the screen were deposited on the surface. After this observation, the investigation of the effect of the screen material was started.

3.1. Plasma nitriding of titanium with different active screens

Before and after the nitriding, mass measurements were performed on the specimen, which results are shown in Table 2.

The mass increase was not observed after the nitriding with titanium screen, but it was increased with steel screen.

Figure 1 shows the surface after the nitriding.

As can be seen in Figure 1, the surface of the sample, which was nitrided with steel screen, was matt while the scratches of surface preparation were observed and the light was refracted differently by the optically active layer of the surface in the sample which was treated with titanium screen. It was clear that the golden yellow colour is a characteristic of TiN [17] was not formed

Table 2. Masses of titanium samples which were nitrided with different active screens

Sample	m _{st.} (g)	m _{end.} (g)	Δm (g)
Steel screen	8.4130	8.4146	0.0016
Titanium screen	8.3364	8.3365	0.0001

which suggested that this type of nitride did not form on the surface.

The hardness of the titanium sample was $332 \text{ HV}0.01 \pm 25$. With steel screen, the hardness was $661 \text{ HV}0.01 \pm 32$ which is two times higher than the base hardness, while the hardness was changed to $436 \pm 14 \text{ HV}0.01$ after the nitriding with titanium screen. The titanium-nitrides can reach up to 1400 HV hardness [18]. According to this, the compound layer was not formed, or it was so thin that the diamond head could pass over the entire layer.

Figure 2 shows the cross-section images of the samples.

It can be seen in the optical microscope images that the compound layer was not created on the surface. The microstructure of the samples was different near the edges and in the middle of the surface. Based on the hardness testing of the cross-section, the hardness was decreasing to the base hardness through 0.1 mm , which proves with the previous observations that the nitrogen could diffuse into the material. Table 3 shows the the chemical composition of the surface measured with EDS.

It is seen that the titanium content of the surface was decreased compared to the base titanium content and iron appeared in a large amount with steel screen. On the samples, which treated with titanium screen, the titanium content was increased, but the content of the other elements was not changed significantly. Nitrogen appeared in both cases. These proved that the sputtered particles from the screen could deposit on the surface; moreover, it could cover the surface of the samples.

3.2. Plasma nitriding of tempered steel with titanium active screen

In the previous experiments, TiN was not created on the surface, but the sputtered particles from the surface deposited on the sample; therefore, $42\text{CrMo}4$ was nitrided with a smaller screen. The sample was marked to ASPN Ti.

The results of the mass measurements are seen in Table 4.

The mass increase in this case, same as before, was significant, but the hardness was not increased. The hardness of the sample remained within the range of the deviation, $320 \pm 20 \text{ HV}0.01$. The compound layer also did not form on the surface.

After the nitriding, different tones of colours were observed on the surface, which is seen in

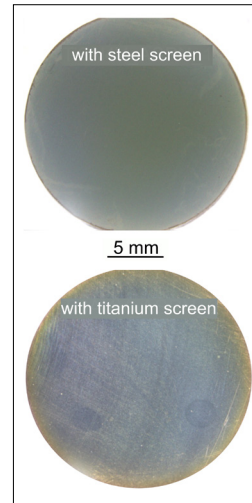


Figure 1. Stereomicroscopic images of titanium samples surface which was nitrided with different screens.

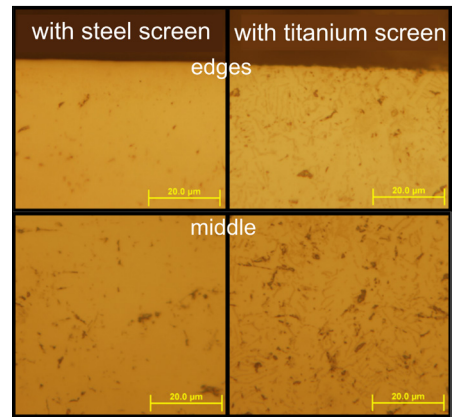


Figure 2. Optical microscopic images of cross-sections of nitrided titanium samples which was nitrided with different screens.

Table 3. Chemical composition of the samples with EDS analysis which was nitrided with different screens

Element (%)	Base material	With steel screen	With Ti screen
Ti	83.18	11.19	85.21
Al	6.10	0.18	6.72
V	4.33	0.91	3.77
O	6.15	7.34	1.14
Si	0.24	–	–
N	–	7.40	3.16
Fe	–	72.98	–

Table 4. Mass of the sample which was nitrided with titanium screen

Sample	m _{st.} (g)	m _{end} (g)	Δm (g)
ASPN_Ti	12.5257	12.5267	0.0010

Table 5. Chemical composition of the samples with EDS analysis which was nitrided with titanium screen

Component (%)	Base material	ASPN_Ti middle	ASPN_Ti edge
N	–	7.46	4.86
O	–	5.17	3.51
Al	–	0.17	–
Si	0.28	0.24	–
Ti	–	5.98	3.37
Cr	1.41	1.18	1.21
Fe	99.4	79.79	87.05
Mo	0.12	–	–
Mn	0.74	–	–

Table 6. Chemical composition of the steel sample with XPS analysis which was nitrided with titanium screen

Element	Amount (%)
C1s	74.88
N1s	2.22
O1s	16.06
Ti2p	4.24
Ca2p	1.53
Mn2p	0.36
Si2p	0.38
Na1s	0.07

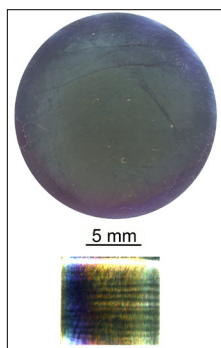
**Figure 3.** 42CrMo4 sample was nitrided with a titanium screen. The lower picture shows the formed colour transition during the nitriding.

Figure 3. Between these colours, the golden yellow appeared near the edges, and because of this EDS analysis was performed at different points. **Table 5** shows the results of the measurements.

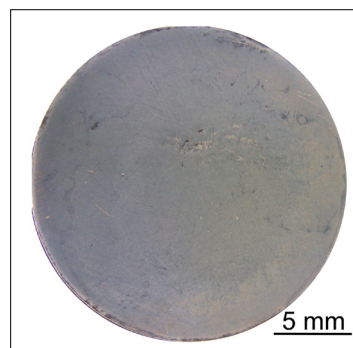
It can be observed that titanium was deposited from the surface to the sample, but the expected TiN was not formed near the edges because in this point the iron content was higher than in the middle; moreover, the nitrogen content was decreased too. XPS analysis was performed for a more accurate determination [19, 20] which results are seen in **Table 6**.

The formed layer on the surface completely covers the base material, because iron, molybdenum and chromium were not seen in the spectrum. The formed layer contained titanium and nitrogen, but these elements were not bound. The different colours of the sample referred to the creation of titanium-oxide, but based on the measurements (however the formed bonds were closer to TiO₂ than the TiN) it cannot be stated that the surface was covered only with a titanium-oxide layer. It is most likely that a TiN_xO_y layer was formed on the surface; its thickness and composition was varied depending on the location.

3.3. Plasma nitriding of tempered steel with nickel coated active screen

The base material of the active screen was unalloyed steel, which was galvanized with nickel in 70 μm thickness.

After the nitriding, the surface was given uniform grey colour (**Figure 4**) in which the scratch of the polishing can be seen; it means that the compound layer also was not formed on the surface.

**Figure 4.** Stereomicroscopic image of 42CrMo4 sample which was nitrided with nickel coated active screen.

It can be seen in the optical microscopic image (Figure 5.) that the compound layer was not created, which was proved by the hardness measurement. Again, the hardness was not increased in this sample; the values were within the deviation 420 ± 45 HV0,01.

Further analysis was performed by XPS for that the upper 100 nm layer was vaporized; then the chemical composition was measured in this depth. Figure 6 shows its results.

As it is seen in this figure, the nitrogen has not created a bond with the iron, so iron-nitride did not appear – which verifies the previous suppositions. Most of the detected nitrogen (84 %) was molecular (N_2) on the sputtered layer. In this depth, N-C were presented in a low amount (16 %), but it does not have a hardening effect to the surface.

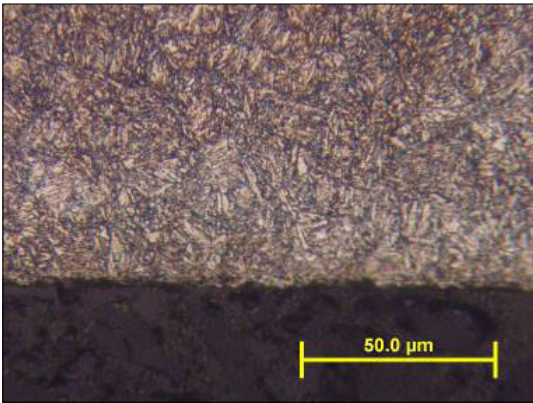


Figure 5. The microstructure of 42CrMo4 sample which was nitrided with nickel coated screen.

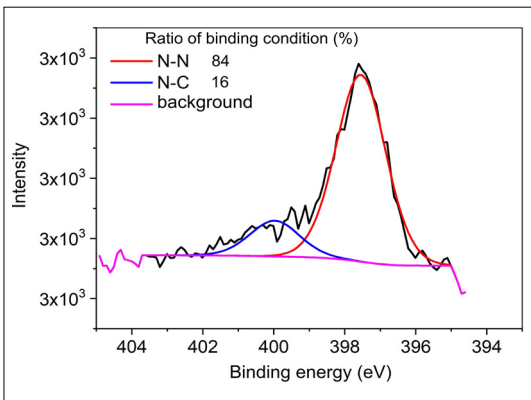


Figure 6. XPS characteristic diagram of 42CrMo4 sample which was nitrided with nickel coated screen.

4. Conclusion

The material of the active screen affects the surface properties of the nitrided sample during active screen plasma nitriding in the following ways:

- no hardening effect occurs;
- the compound layer does not form on the surface, so iron-nitride was not created;
- particles from the active screen were deposited on the sample.

With nickel coated active screen plasma nitriding at 510 °C, for 4 hours with 75 % N_2 + 25 % H_2 gas mixture only nickel from the surface of the screen has adhered to the sample surface at hundreds of nm thickness, and iron nitride phases were not formed. This can even be considered as a new surface alloying process.

Acknowledgement

The authors are grateful to Viktor Takáts from the Institute for Nuclear Research and to Gábor Dobos from the from BME, Department of Atomic Physics for the XPS measurements.

References

- [1] Yaghmaee M.S., Kaptay G.: *The Solubility of Nitrogen and Nitrides in Ternary Liquid Iron Alloys. The Limits of the 'Solubility Product' Concept.* Materials Science Forum 414–415. (2003) 491–496.
- [2] Kolozsváry Z.: *Nitriding structure and properties of nitrided layer.* ASM Handbook, Volume 4D, Heat Treating of Irons and Steels (2014) 88–96. <https://doi.org/10.31399/asm.hb.v04d.a0005986>
- [3] Szilágyiné B. A.: *Trends of nitriding processes.* Production Processes and Systems, 6. (2013) 57–69.
- [4] Aizawa T., Wasa K.: *Low temperature plasma nitriding of inner surfaces in stainless steel mini-/micro-pipes and nozzles,* Micromachines. 8. (2017) 1–9. <https://doi.org/10.3390/mi8050157>
- [5] Szilágyiné B. A., Kocsisné B. M.: *Comparison of gas and plasma nitrocarburised surface layer of 16CrMo5 steel.* Proceedings – European Conference on Heat Treatment and 21st IFHTSE Congress (2014) 551–558.
- [6] Börner K., Burlacov I., Spies H., Biermann H., Hamann S., Röpcke J.: *Investigations on the active screen plasma nitriding process.* In: 13th International Conference on Plasma Surface Engineering (2012) 96–99.
- [7] Middendorf C., Mader W.: *Growth and microstructure of iron nitride layers and pore formation in ϵ -Fe $_3$ N.* Zeitschrift für Metallkunde/Materials Research and Advanced Techniques 94. (2003) <https://doi.org/10.3139/146.030333>

- [8] Kenéz L., Kutasi N., Filep E., Jakab-Farkas L., Ferencz L.: *Anodic plasma nitriding in hollow cathode (HCAPN)*. HTM – Journal of Heat Treatment and Materials, 73. (2018) 96–105. <https://doi.org/10.3139/105.110344>.
- [9] Li Y., Zhang S., He Y., Zhang L., wang L.: *Characteristics of the nitrided layer formed on AISI 304 austenitic stainless steel by high temperature nitriding assisted hollow cathode discharge*. Materials and Design, 64. (2014) 527–534. <https://doi.org/10.1016/j.matdes.2014.08.023>.
- [10] Sousa de R. R. M., Araújo de F. O., Costa da J. A. P., Dumelow T., Oliveira de R. S., Alves C.: *Nitriding in cathodic cage of stainless steel AISI 316: Influence of sample position*. Vacuum 83. (2009) 1402–1405. <https://doi.org/10.1016/j.vacuum.2009.04.054>
- [11] Salavat M. K., Soltanieh M., Niasari M. H.: *Diffusion Layer Growth Mechanism in ASPN Method Using an Iron Cage for St52 Steel*. In: Proceedings of the 2nd World Congress on Mechanical, Chemical, and Material Engineering (MCM'16) (2016) 1–8. <https://doi.org/10.11159/mmmme16.106>
- [12] Gallo C. S., Dong H.: *On the fundamental mechanisms of active screen plasma nitriding*. Vacuum, 84. (2009) 321–325. <https://doi.org/10.1016/j.vacuum.2009.07.002>
- [13] Zaho C., Li C. X., Dong H., Bell T.: *Study on the active screen plasma nitriding and its nitriding mechanism*. Surface and Coatings Technology, 201. (2006) 2320–2325. <https://doi.org/10.1016/j.surfcoat.2006.03.045>
- [14] Naeem M., Sha M., Zaka-ul-islam M., Ashiq A., Díaz-Gullién J. C., Shahzad M., Zakaullah M.: *Enhanced surface properties of plain carbon steel using plasma nitriding with austenitic steel cathodic cage*. Materials and Design, 108. (2016) 745–753. <https://doi.org/10.1016/j.matdes.2016.07.044>
- [15] Yazdani A., Soltanieh M., Aghajani H.: *Active screen plasma nitriding of Al using an iron cage: Characterization and evaluation*. Vacuum, 122. (2015) 127–134. <https://doi.org/10.1016/j.vacuum.2015.09.018>
- [16] Kauling A. P., Soares G. V., Figueroa C. A., Oliverira de R. V. B., Baumvol I. J. R., Giacomelli C., Mioti L.: *Polypropylene surface modification by active screen plasma nitriding*. Materials Science and Engineering, C, 29. (2009) 363–366. <https://doi.org/10.1016/j.msec.2008.07.002>
- [17] Kamat A. M., Copley S. M., Todd J. A.: *Effect of processing parameters on microstructure during laser-sustained plasma (LSP) nitriding of commercially-pure titanium*. Acta Materialia, 107. (2016) 72–82. <https://doi.org/10.1016/j.actamat.2016.01.051>
- [18] Nishimoto A., Nii H., Narita, Akamatsu K.: *Simultaneous duplex process of TiN coating and nitriding by active screen plasma nitriding*. Surface and Coatings Technology, 228. (2013) 558–562. <https://doi.org/10.1016/j.surfcoat.2012.04.021>
- [19] Kovách G., Csorbai H., Dobos G., Karacs A., Pető G.: *Formation and characterization of electric contacts on CVD diamond films prepared by ion implantation*, Materials Science Forum, 473–474. (2005) 123–128. <https://doi.org/10.4028/www.scientific.net/MSF.473-474.123>
- [20] Takáts V., Csík A., Hakl J., Vad K.: *Diffusion induced atomic islands on the surface of Ni/Cu nanolayers*. Applied Surface Science, 440. (2018) 275–281. <https://doi.org/10.1016/j.apsusc.2018.01.087>

Evaluation of Closed and Open-cell Structural Lattices with Finite Element Analysis

Klaudia KULCSÁR,¹ János KÓNYA²

Dent-Art-Technik Kft. Győr, Hungary

¹ kulcsar.klaudia@dentarttechnik.hu

² janos@dentarttechnik.hu

Abstract

Four lattice structures based on well-known crystal structures were evaluated in this study using the finite element method. Simple cubic, face-centered cubic, body-centered cubic, and diamond structural alignments were used to build up lattices from the body volume. Modern-day implant development trends are shifting towards additive manufacturing technologies, which have the advantage of creating structures that can improve the biological stability of implants that have integrated scaffolds. Such scaffolds can be trabecular structures that mimic bone tissue and facilitate tissue penetration into the porous parts of the implant. The final purpose of our study is to create an implant system that promotes the process of osseointegration. Evaluations have been carried out using finite element analysis.

Keywords: *closed cell structures, open cell structures, finite element analysis, crystal structures .*

1. Introduction

In orthopaedic surgery, cellular lattices are used as three-dimensional porous bio-products that attempt to mimic the structure and behaviour of bone tissue [1]. Porous biomaterial, which must be designed to have the same mechanical properties as that of bone tissue, may be used as bone replacements. Several other design factors that improve bone growth shall be considered as well. For example, permeability of the bone mimicking porous structure can affect cell migration [2]. Several principles have emerged in the last two decades allowing design structures that could replace bone tissue. These principles consider both mechanical properties, biocompatibility and bio functionality [3, 4]. In most studies, porous structures were made from titanium or titanium alloys, but titanium alloys are stiffer, and their mechanical properties outperform those of bone tissue [5]. Differences in mechanical properties of bone and titanium alloys can block bone growth and can cause bone resorption, which may lead to implant loosening [6, 7]. Porous structures are created with additive man-

ufacturing technology, and their mechanical properties are closer to that of human bone [5, 8, 9].

In recent years, additive manufacturing technology (which some literature sources call rapid prototyping or 3D printing) has become widely popular. Here, the final product is made up layer-by-layer [10]. Selective Laser Melting (SLM) has been successfully developed recently to process metal powders. The density of parts manufactured with SLM can exceed 99 % [11]. Commercially pure titanium and titanium alloys are still generally used in medical implants to replace hard tissues and bone, because they have outstanding mechanical and biological properties [12]. Implants are also made from other biocompatible materials such as Co-Cr alloy and stainless steel. Comparing their elastic moduli with that of titanium alloys, one can see that the latter has a lower modulus of elasticity. However, elastic modulus of titanium is still much higher than that of human bone tissue [13]. Ahmadi et al studied six different lattice structures that had been manufactured with selective laser melting

(SLM) from Ti-6Al-4V ELI (Grade 23) powder. The types of studied lattice structures were simple cubic, diamond, truncated cube, truncated cuboctahedron, rhombic dodecahedron, and rhombicuboctahedron. Cylindrical test specimens were manufactured using these previously mentioned structures. Then, they were subjected to static compression testing [14]. Chen et al studied open-cell models with different porosities. During their investigation, they studied the differences in the geometry of the porous structures between CAD models and final 3D printed parts. For example, the CAD model with 80 % theoretical porosity was printed with only 71 % porosity in practice [15].

2. Presentation of evaluated structures

The main purpose of this study was to create a porous scaffold that promotes and speeds up the osseointegration process at the bone-implant interface after implant insertion. In our previous studies, we experimented with 20×20 mm cubes that had been designed based on existing crystal structures. In this study, we investigated the environment of these small cubic structures by building up 60×60×60 mm cubes from them.

2.1. Simple cubic structure

Simple cubic structure was made up of 20×20×20 mm cubes with cutout spheres located at the corner points. Cutout sphere diameter was gradually increased in 0.1 mm increments. **Figure 1** shows the phases of volume reduction. The lattice structure was designed as the negative of the crystal structure. The upper surface was left intact as a plane; no spheres were removed from there. Volume reduction was achieved by increasing cutout sphere diameter. For simple cubic structure, the closed-cell structure did not transform into an open-cell lattice. Thus, low volume reduction could be achieved in this case.

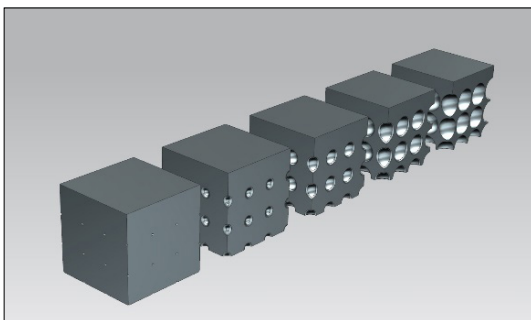


Figure 1. Simple cubic cell structure from the solid model.

2.2. Face-centered cubic structure

In face-centered cubic structure, cutout spheres were located at the cornerpoints and at the centre of each side of the cube. The upper surface was left intact as a plane; no spheres were removed from the cornerpoints. The porous structure was designed as the negative of the crystal structure. **Figure 2** shows phases of volume reduction for face-centered cubic structure. For this structural alignment, it was observed that an open-cell structure emerged. Thus, large volume reduction could be achieved. Cutout sphere diameters were increased in 0.1 mm increments here as well.

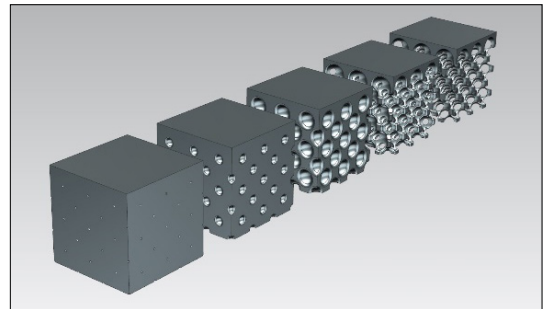


Figure 2. Face-centered cubic structure from the solid model.

2.3. Body-centered cubic structure

In body-centered cubic structural alignment, cutout spheres were located at the cornerpoints and at the middle of the body diagonal of the 20×20×20 mm cubes. For this solution, the upper surface was left planar as well, because no spheres were removed from those cornerpoints. The lattice was designed as the negative of the crystal structure. Cutout sphere diameter was increased in 0.1 mm increments here as well. **Figure 3** shows phases of volume reduction for body-centered cubic structure. It is notable here that the structure transformed into an open-cell scaffold. Thus, large volume reduction could be achieved.

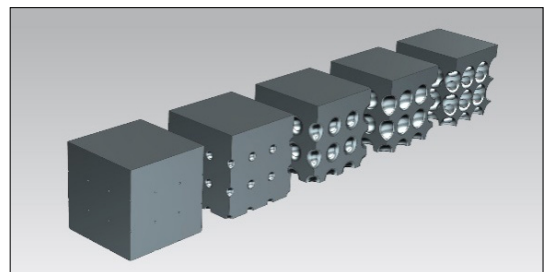


Figure 3. Body-centered cubic structure from the solid body.

2.4. Diamond structure

Diamond structure can be derived from face-centered cubic structure. This meant, cut-out spheres were located at the cornerpoints, at each side of the small cubes, and at the mid-octan centres as well. The upper surface was left planar here also. Thus, spheres were not removed from one mid-octan centre and from the upper cornerpoints of the cubes. Cutout sphere diameter was increased by 0.1 mm also. **Figure 4** shows phases of volume reduction for diamond structure.

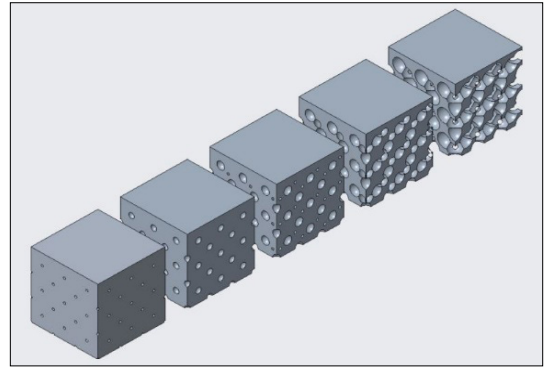


Figure 4. Diamond structure from the solid body.

3. Results of finite element analysis

Simulations were carried out using ANSYS software. For each of the above-mentioned structures, a $60 \times 60 \times 60$ mm cube was created that consisted of smaller, $20 \times 20 \times 20$ mm cubes. Mechanical loads were identical in all cases: the lower part of the cube was fixed, and 4500 N force was exerted on the upper planar surface. The acting force was evenly distributed, and a friction-free fix constraint was chosen. Stress intensity levels were analysed first, and can be seen in **Figure 5** on a representative meshed part.

We wanted to see how the small cube in the centre behaves with its entire environment. Thus, stress intensity levels were analysed in the central small cube separately, too. One example is shown in **Figure 6** with its meshing.

Results of different structures were compared and then, stress intensity levels were compared in the entire body in order to find which structure provided the best results.

3.1. Results of simple cubic structure modelling

199 simulations were conducted on the part with simple cubic structure. The smallest cutout sphere diameter was 0.1 mm, while the largest was 19.9 mm. **Figure 7** shows measurement results. Maximum of equivalent stresses in the entire body and that in the central area were quasi identical. The lowest possible cell volume ratio, which is the ratio between the volume of the given lattice structure and the volume of the solid starting body in the form of a percentage, was only around 57 %. Equivalent stress levels were minimal here. The simple cubic structure was only a closed-cell scaffold.

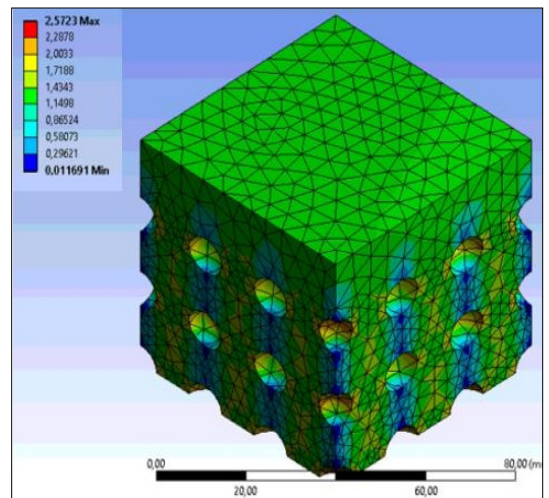


Figure 5. Visualization of equivalent stress in the entire body.

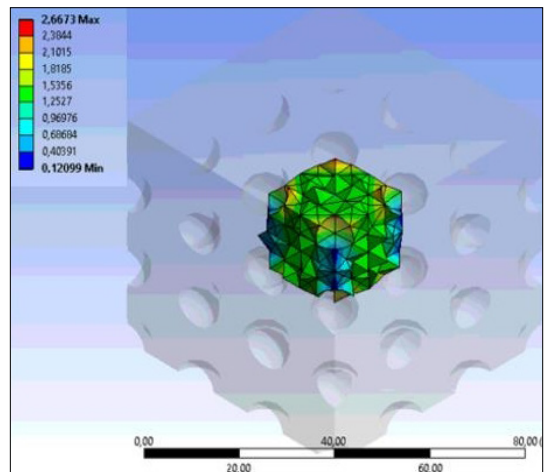


Figure 6. Visualization of equivalent stresses in the centric cube.

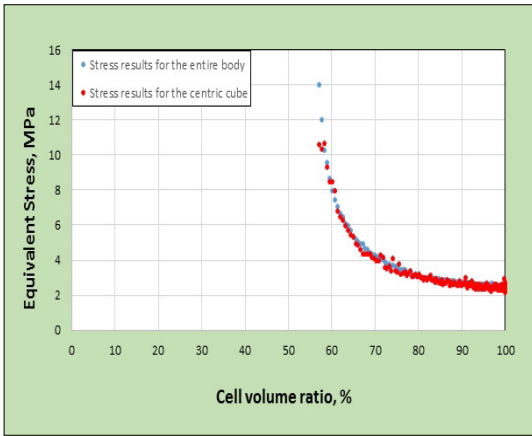


Figure 7. Equivalent stress levels versus cell volume ratio in the parts with simple cubic lattice structure.

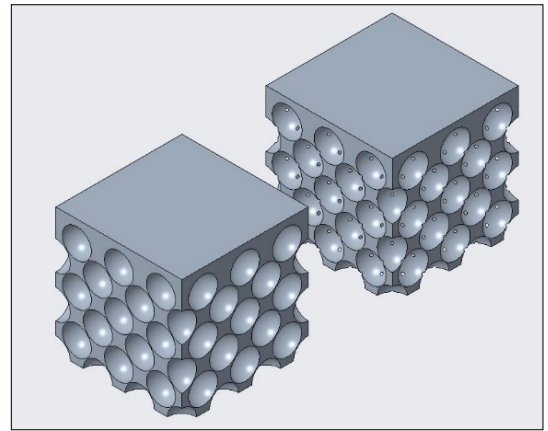


Figure 9. Closed and open-cell structural geometry with face-centered cubic configuration.

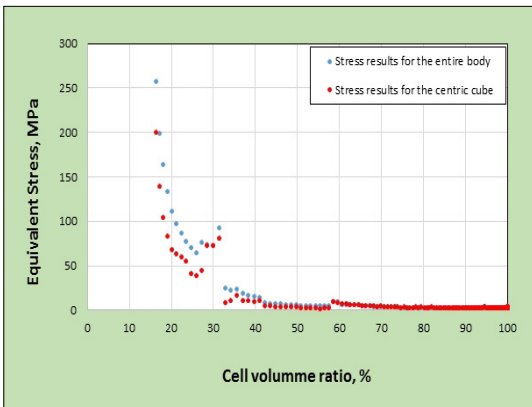


Figure 8. Equivalent stress levels versus cell volume ratio in the parts with face-centered cubic lattice structure.

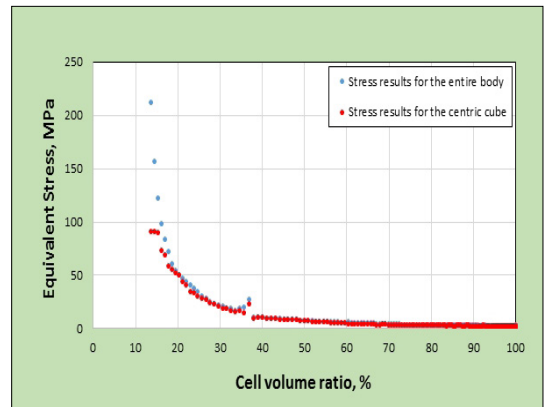


Figure 10. Equivalent stress levels versus cell volume ratio in the parts with body-centered cubic lattice structure.

3.2. Results of face-centered cubic structure modelling

155 simulations were conducted for face-centered cubic structure. The smallest diameter was 0.1 mm, while the diameter of the largest cutout sphere was 15.5 mm. **Figure 8** shows equivalent stress maximum levels for the part with face-centered cubic structure. At the volume ratio of 32 %, equivalent stress was higher. At that point, the lattice transformed from closed-cell to open-cell structure. Volume could be reduced substantially for the lattice with face-centered cubic structure, and stress intensity levels were still acceptable at the cell volume ratio of 20 %.

At the cell volume ratio of 32 %, the lattice transitioned from closed to open-cell configuration. **Figure 9** shows the geometries of the closed and open-cell structures.

3.3. Results of body-centered cubic structure modelling

199 simulations were conducted for body-centered cubic lattice structure with the smallest cutout sphere diameter of 0.1 mm. The largest removed spheres were 19.9 millimetres in diameter. **Figure 10** shows maximum equivalent stress levels for body-centered cubic lattice structure. Higher equivalent stress was measured at the volume ratio of 36 %. Then stress levels started to decrease and then increased again. This was the point where the closed-cell lattice transformed into an open-cell structure. Substantial volume reduction could be achieved for body-centered cubic structure, and equivalent stress levels were still considered particularly good at the cell volume ratio of 13 %.

At the cell volume ratio of 36 %, the structure transitioned from closed to open-cell configuration. **Figure 11** shows the geometries of the closed and open-cell structures.

3.4. Results of diamond structure modelling

132 simulations were conducted for diamond lattice structure with the smallest cutout sphere diameter of 0.1 mm. The largest removed spheres were 13.3 millimetres in diameter. **Figure 12** shows maximum equivalent stresses. Stress levels increased at the cell volume ratio of 63 %. It was the point when the closed-cell alignment transitioned into an open-cell one. There is another increase at 57 %. Equivalent stress levels for diamond lattice structure were acceptable up to the cell volume ratio of 40 %.

Figure 13 presents the geometric alignment of the closed and open-cell lattice structures. It is notable that this structure had more transition levels compared to the previously mentioned ones.

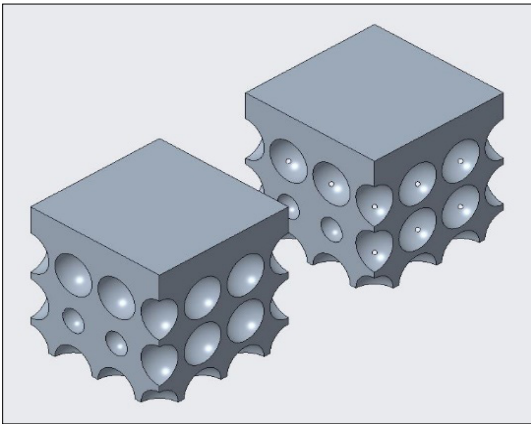


Figure 11. Closed and open-cell structural geometry with body-centered cubic configuration.

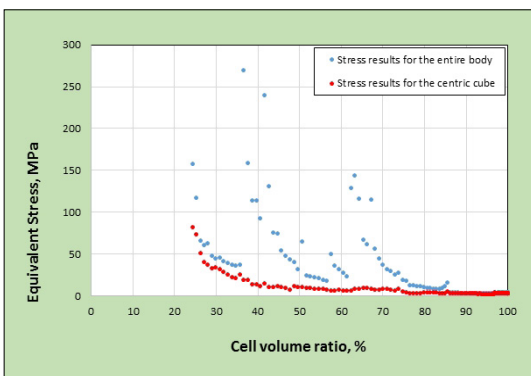


Figure 12. Equivalent stress levels versus cell volume ratio in the parts with diamond lattice structure.

4. Conclusions

Previously mentioned test results were collected in **Figure 14**. The diagram shows the sets of result points corresponding equivalent stress levels of the entire lattice for simple cubic, face-centered cubic, body-centered cubic, and diamond structures as a function of cell volume ratio. The least volume reduction could be achieved with the simple cubic structure type, so it is unimportant that stress results were low as well. This lattice remained a closed-cell structure “only”, which is why this solution can be considered irrelevant. Depending on the cell volume fraction, equivalent stress levels were higher for the diamond lattice structure. Face-centered and body-centered cubic lattice structures provided almost identical results up until the volume fraction of 35 %. Then, below this value, equivalent stress levels in the face-centered structure started to increase. Face-centered and body-centered cubic, and diamond structures could all contain closed and open-cell scaffolds. For all the three lattices, the transition from closed to open-cell structure was clearly noticeable. Increase in equivalent stress levels was well-defined, which was due to the reduced wall thicknesses in the solid models when structures transitioned from closed-cell to open-cell designs.

In this study, different cell structures were investigated that conformed to the atomic alignment of cubic crystal lattice structures. Equivalent stress levels were investigated both in the entire lattice and in its central area. To summarize, body-centered cubic lattice structure provided the best results. Calculations are going to be validated empirically as well on additively manufactured test specimens

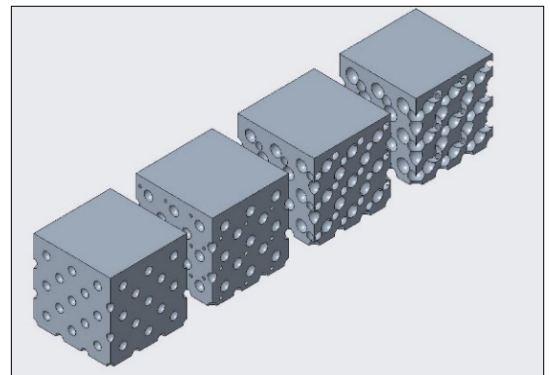


Figure 13. Closed and open-cell structural geometry with diamond configuration.

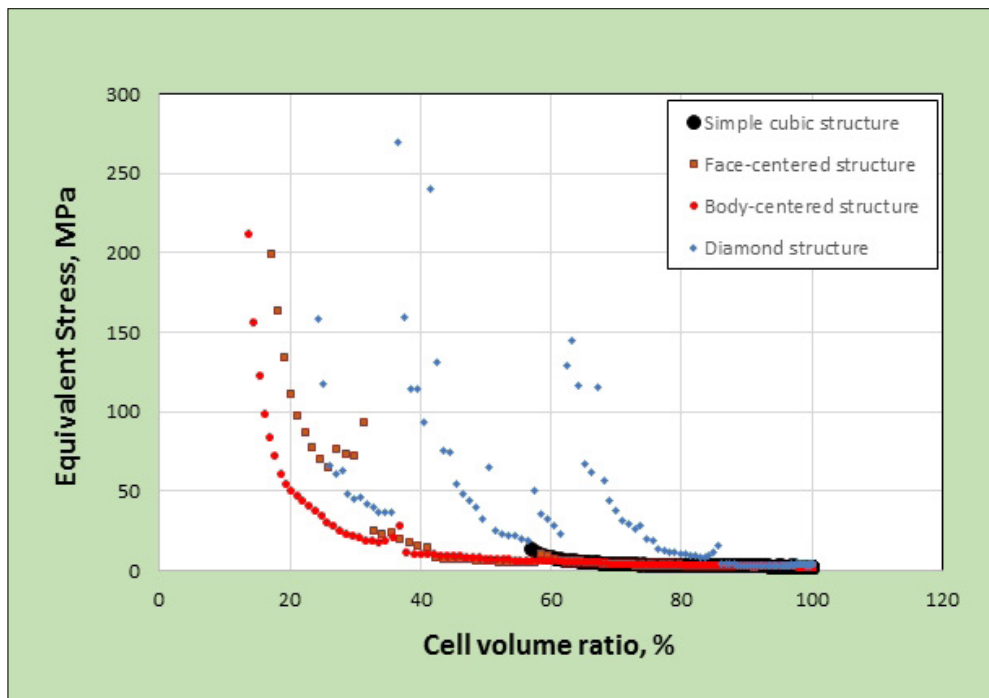


Figure 14. Antegrated set of results.

Acknowledgement

I would like to express my special thanks to János Dobránszky DSc, who helped in this study.

References

- [1] Butscher A., Bohner M., Hofmann S., Gauckler L., Müller R.: *Structural and material approaches to bone tissue engineering in powder-based three-dimensional printing*. Acta Biomaterialia, 7/3. (2011) 907–920. <https://doi.org/10.1016/j.actbio.2010.09.039>
- [2] Hollister S. J.: *Porous scaffold design for tissue engineering*. Nature Materials, 5/7. (2005) 518–524. <http://doi.org/10.1038/nmat1421>
- [3] Hutmacher D. W.: *Scaffold design and fabrication technologies for engineering tissues – state of the art and future perspectives*. Journal of Biomaterials Science, Polymer Edition, 12/1. (2001) 107–124. <https://doi.org/10.1163/156856201744489>
- [4] Goulet R. W., Goldstein S. S., Ciarelli M. J. et al.: *The relationship between the structural and orthogonal compressive properties of trabecular bone*. Journal of Biomechanics, 7/4. (1994) 379–389. [https://doi.org/10.1016/0021-9290\(94\)90014-0](https://doi.org/10.1016/0021-9290(94)90014-0)
- [5] Ahmadi S. M., Campoli G., Yavari S. A. et al.: *Mechanical behavior of regular open-cell porous biomaterials made of diamond lattice unit cells*. Journal of the Mechanical Behavior of Biomedical Materials, 34/1. (2014) 106–115. <https://doi.org/10.1016/j.jmbbm.2014.02.003>
- [6] Engh C. A., Bobyn J. D., Glassman A. H.: *Porous-coated hip replacement. The factors governing bone ingrowth, stress shielding, and clinical results*. The Journal of Bone and Joint Surgery, 69-B/1. (1987) 45–55. <https://doi.org/10.1302/0301-620X.69B1.3818732>
- [7] Huiskes R., Weinans H., van Rietbergen B.: *The relationship between stress shielding and bone resorption around total hip stems and the effects of flexible materials*. Clinical orthopaedics and related research, 274/1. (1992) 124–134. <https://doi.org/10.1097/00003086-199201000-00014>
- [8] Amin Yavari S., Ahmadi S. M., van der Stock J. et al.: *Effects of bio-functionalizing surface treatments on the mechanical behavior of open porous titanium biomaterials*. Journal of the Mechanical Behavior of Biomedical Materials, 36/1. (2014) 109–119. <https://doi.org/10.1016/j.jmbbm.2014.04.010>
- [9] Van der Stock J., Van der Jagt O. P., Amin Yavari S., et al.: *Selective laser melting-produced porous titanium scaffolds regenerate bone in critical size cortical bone defects*. Journal of Orthopaedic Research, 31/5. (2013) 792–799. <https://doi.org/10.1002/jor.22293>
- [10] Gibson I., Rosen D. W., Stuckre B.: *Additive Manufacturing Technologies. Rapid Prototyping to Direct Digital Manufacturing*. Springer, New York, 2010. 6–9.

- [11] Vandebroucke B., Kruth J. P.: *Selective laser melting of biocompatible metals for rapid manufacturing of medical parts*. Rapid Prototyping Journal, 13/4. (2007) 196–203.
<https://doi.org/10.1108/13552540710776142>
- [12] Li Y., Yang C., Zhao H. et al.: *New Developments of Ti-Based Alloys for Biomedical Applications*. Materials, 7/3. (2014) 1709–1800.
<https://doi.org/10.3390/ma7031709>
- [13] Zysset P. K., Guo X. E., Hoffer C. E.: *Elastic modulus and hardness of cortical and trabecular bone lamellae measured by nanoindentation in the human femur*. Journal of Biomechanics, 32/10. (1999) 1005–1012.
[https://doi.org/10.1016/S0021-9290\(99\)00111-6](https://doi.org/10.1016/S0021-9290(99)00111-6)
- [14] Ahmaid S. M., Yavari S. A., Wauthle R.: *Additively Manufactured Open-Cell Porous Biomaterials Made from Six Different Space-Filling unit Cells: The Mechanical and Morphological Properties*. Materials, 8/4. (2015) 1871–1896.
<https://doi.org/10.3390/ma8041871>
- [15] Chen S. Y., Huang J. C., Pan C. T.: *Microstructure and mechanical properties of open-cell porous Ti-6Al-4V fabricated by selective laser melting*. Journal of Alloys and Compounds, 713. (2017) 248–254.
<https://doi.org/10.1016/j.jallcom.2017.04.190>

Development of Magnetic Material Testing Equipment

András NAGY,¹ Imre NÉMEDI²

¹ University of Dunaujváros, Dunaujvaros, Hungary, nagyandras@uniduna.hu

² Technical Vocational College of Serbia, Subotica, Serbia, nimre@vts.su.ac.rs

Abstract

This paper deals with the development of equipment that can accurately determine the magnetic properties of small volume thin plate samples. The alloys to be tested are sheets of amorphous structure, such as Finemet alloy, which has excellent high frequency magnetic properties, making it a good candidate for the construction of high efficiency electric motors. This article discusses the components and operation of the equipment under development, whilst giving a brief overview of the efficiency classification of electric motors and the importance of the emerging efficiency class.

Keywords: *amorphous, BH curve, magnetic measuring equipment, fluxgate sensor.*

1. Introduction

This paper discusses the development of a magnetic tester that can accurately determine the magnetic properties of small volume thin plate samples. The alloys to be tested are plates of amorphous structure, such as Finemet alloy, which has excellent high-frequency magnetic properties. In [1] a 6-pole electric motor stator was made of amorphous material, achieving an efficiency of over 90 %. The use of amorphous material in BLDC (brushless direct current) motors also shows advantageous properties, in [2] a 1 kW motor with a speed of 70,000 rpm was built using Metglas 2605 SA1 alloy. Tests have shown that the use of an amorphous material can reduce the heating of the electric motor. [3] gives a comprehensive review of the results of recent applications of amorphous materials in electric motors. A study of a two-pole, 1.2 kW motor revealed that when using amorphous materials, the loss is reduced by 1/5 [4].

The required minimum efficiency of an electric motor is the function of power, electric motors currently available on the market fall into the IE1-IE3 category. The European Union has issued a regulation [5] on eco-design requirements for electric motors. The emergence of IE4 class

motors („Super premium efficiency”, defined in IEC 60034-30 and IEC 60034-331) requires new technologies and materials to reduce the various losses of electric motors.

In the manufacturing sector, electric motors account for an average 70 % of electricity consumption [6]. It is clear that the goal is better energy efficiency, which means less environmental emissions.

The use of amorphous materials requires that thin amorphous sheets having a thickness of 20–40 µm be cut to the proper shape so that machining has the least possible effect on the amorphous structure as well as on the favourable magnetic properties. Cutting experiments [7] show that laser cutting with appropriate technological parameters produces a minimal heat affected zone. Thus, the amorphous material structure is damaged only to the extent that it does not significantly affect the magnetic properties.

This article describes the development of equipment to measure the impact of different cutting technologies on the magnetic properties of a material. Issues and solutions that arise during the development of the equipment and the measurement process are presented along with the circuitry of the equipment.

2. The structure of the equipment

2.1. Basis of the operation

The operation of the magnetic tester is based on the fact that when a material is placed in a DC magnetic field, it creates its own magnetic field under excitation. By measuring this, the hysteresis loop can be determined and the resulting values calculated (eg. coercive force, remnant magnetization, etc.). In order to excite the examination sample, the homogeneous magnetic field can be produced in various ways, for example by means of a Helmholtz coil or a solenoid. The magnetic testing apparatus disclosed herein uses a solenoid for this purpose, which creates a highly accurate magnetic field inside (in case of sufficiently accurate geometry) (Figure 1).

The ferromagnetic pattern placed inside the solenoid creates its own magnetic field under excitation. This evolving magnetic field is also constant over time due to the excitation of DC current, so it is not suitable for measurement by a conventional measuring coil (based on the measurement of voltage induced by a variable magnetic field). In order to select the appropriate magnetic field sensor, it is necessary to determine some of the characteristics that form the basis of the specification.

Figure 2 shows how the sample is located inside the solenoid. The excitatory magnetic field generated by the solenoid produces a magnetic field in the sample which, due to the small volume of the sample, is orders of magnitude weaker than the excited magnetic field.

The essence of the measurement procedure is, therefore, to measure the magnetic field (B) formed by the excitation (magnetic field strength, H) produced with high precision by the solenoid. From this, the B-H curve can be drawn and magnetic properties calculated.

A block diagram of the magnetic tester is shown in Figure 3.

The central control is carried out by a 16-bit PIC microcontroller that communicates with the coil drive circuit, enabling the digital setting of the output current. The sensor interface sub-circuit of the magnetometer performs signal conditioning and isolation, enabling high-resolution digitization. The device communicates with the control software developed for the PC via a digital interface (USB - VCP).

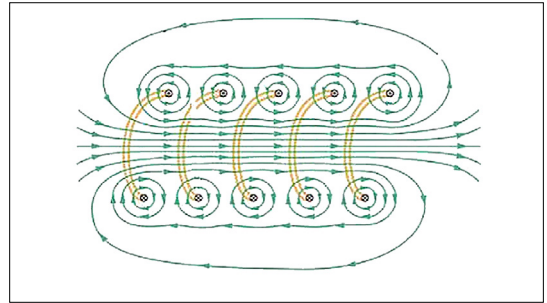


Figure 1. Magnetic field lines formed inside a solenoid.

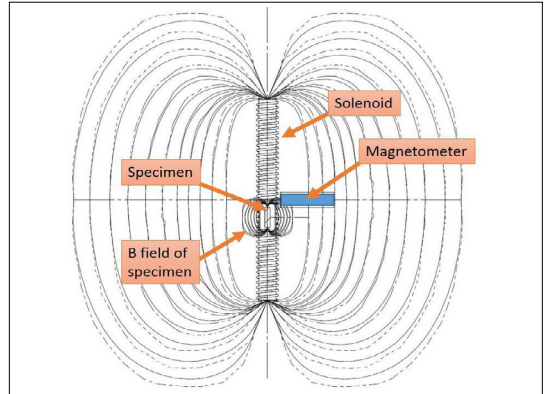


Figure 2. Magnetic field of a sample placed inside a solenoid and the placement of a magnetometer to measure it. [8]

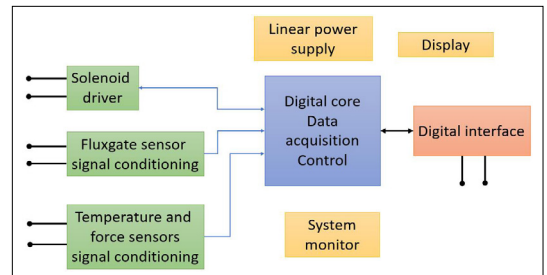


Figure 3. Block diagram of the electronics of the magnetic tester.

2.2. Solenoid design

One of the main components of the device is a solenoid producing a homogeneous magnetic field. Within this, the resulting field strength is calculated using the following formula:

$$H = (N \cdot I) / L \quad (1)$$

in which

H – magnetic field strength, A/m;

N – solenoid number of turns;

I – current, A;

L – length of solenoid, m.

It can be seen that for a given geometry the field strength can be varied proportionally to the current flowing in the coil in a linear relationship. For the sizing of the solenoid, other contexts were also used, such as Ohm's Law.

Scaling is based on a few recorded data:

- length of solenoid: 500 mm;
- external diameter of solenoid core: 50 mm;
- maximum field strength (min.): 30 000 A/m.

From the initial data the following results were obtained:

- solenoid No. of turns (by layer): 306;
- number of layers: 6;
- solenoid Ohmic resistance: 3.08 Ω;
- maximum winding current: 10.3 A;
- coil power dissipation: 332 W;
- wire diameter: 1.6 mm.

The power dissipated by the solenoid is converted into heat, which heats the wire, increasing its resistance. For accurate field strength adjustment, the device is provided with a constant current drive which drives a constant current across the coil regardless of the resistance of the coil. The design of the solenoid and the unit built are shown in **Figure 4**.



Figure 4. The 3D model (left) of the solenoid and the manufactured solenoid (right).

2.3. Magnetic field sensor

A carefully selected sensor is required to detect the magnetic field of the excited sample. **Figure 5** compares the technology of some magnetometers based on measurement ranges.

Among the requirements for the sensor are the relatively low measurement range ($\pm 10 \mu\text{T}$), the high degree of directional sensitivity and the ability to detect a constant (DC) magnetic field.

Fluxgate sensors are best suited to these requirements.

The working principle of the fluxgate magnetometer is illustrated in **Figure 6**. The ferromagnetic iron core of figure (a) is driven in saturation periodically by the drive (primary) coil in both positive and negative directions. The variation in flux density can be captured by the sensor (secondary) coil. In the presence of an external magnetic field, this signal becomes asymmetric, the strength of the magnetic field being proportional to the second harmonic of the signal, figure (b).

3. Component design

3.1. Coil Drive Electronics

The coil drive circuit is essentially a constant current driver and a double H bridge integrated together. In this way, the direction and magnitude of the current can be changed simultaneously.

Magnetic Sensor Technology	Detectable Field (Gauss)				
	10^{-10}	10^{-6}	10^{-2}	10^2	10^6
1. Search-Coil Magnetometer	[Bar from 10^{-10} to 10^6]				
2. Flux-Gate Magnetometer	[Bar from 10^{-6} to 10^2]				
3. Optically Pumped Magnetometer	[Bar from 10^{-6} to 10^2]				
4. Nuclear-Precession Magnetometer	[Bar from 10^{-6} to 10^2]				
5. SQUID Magnetometer	[Bar from 10^{-10} to 10^{-2}]				
6. Hall-Effect Sensor	[Bar from 10^{-2} to 10^6]				
7. Magnetoresistive Magnetometer	[Bar from 10^{-6} to 10^2]				
8. Magnetodiode	[Bar from 10^{-2} to 10^2]				
9. Magnetotransistor	[Bar from 10^{-2} to 10^2]				
10. Fiber-Optic Magnetometer	[Bar from 10^{-10} to 10^2]				
11. Magneto-Optical Sensor	[Bar from 10^{-2} to 10^6]				

Figure 5. Comparison of magnetic field sensor technologies [9]

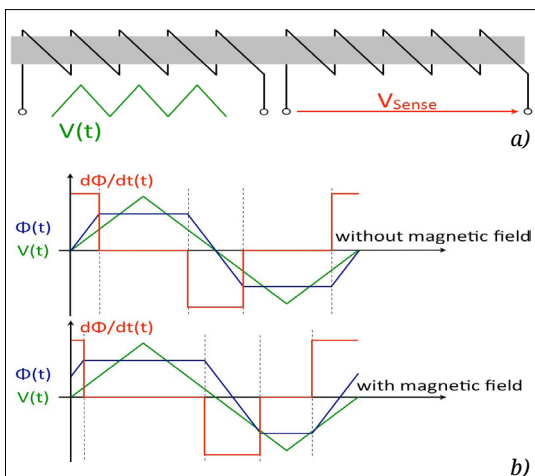


Figure 6. Operating principle of Fluxgate magnetometer [10].

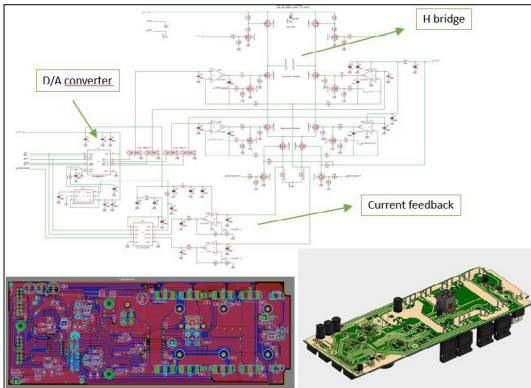


Figure 7. Schematic diagram of coil drive electronics, PCB design and 3D model.

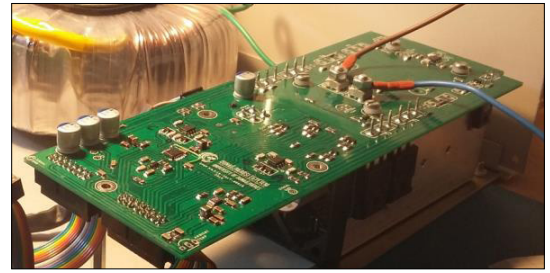


Figure 8. Manufactured and built-in coil drive electronics.

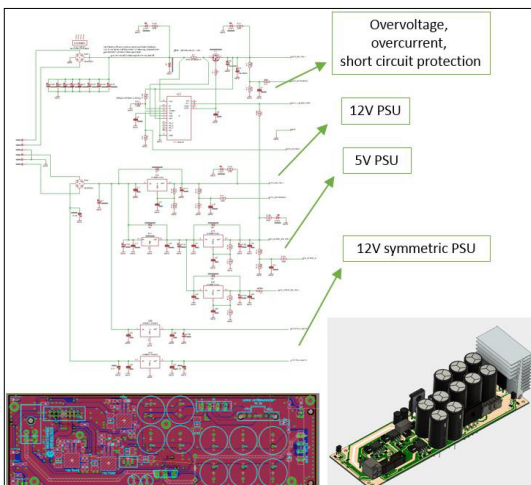


Figure 9. Power Supply schematic, PCB design, and 3D model.

The double H bridge allows the measuring range to be switched in addition to changing current direction, therefore larger and smaller volume samples can be accurately examined.

The photo of the completed electronics is shown in **Figure 7** and **Figure 8** shows the different levels of design.

3.2. Power supply electronics

The power supply must produce several stabilized voltage levels, including 5V for digital circuits, $\pm 12V$ for fluxgate sensors, 36V for solenoid drives. The schematic, the PCB design and the 3D model are shown in **Figure 9**.

The power supply uses the voltage generated by a 230V / 36V toroidal transformer, therefore mains isolation is implemented and electrical safety is ensured. A photograph of the completed



Figure 10. Power supply manufactured and installed.

power supply is shown in **Figure 10**. To handle the heat dissipation of the rectifying diode bridge, a heat sink is applied so that the heat is released outside of the enclosure. For accurate design, electrical and mechanical design have been performed side by side.

3.3. Measurement controller and communication unit

A separate measurement control module has been developed to control the measurement process, to digitize the analog signals and to transfer the measured values to a computer. At the heart of the system is a 16-bit PIC microcontroller, the dsPIC30F6014A-30 from Microchip.

Figure 11 illustrates the circuit schematic, the PCB design and the 3D model of the unit. The unit is also equipped with a 4-line LCD to inform the user about the measurement process. **Figure 12** shows the unit assembled with the front panel with the connecting ribbon cables.

During the design of the measurement control unit, galvanic isolation of the USB port had to be ensured so that neither the computer nor the unit would be damaged by a hot-plug event or a ground loop. This was accomplished with a

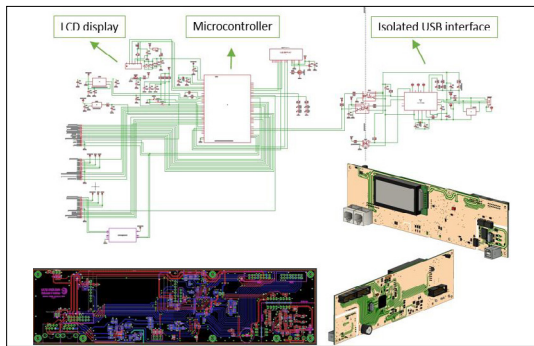


Figure 11. Wiring diagram of the controller, PCB design and 3D model.



Figure 12. Measurement Controller manufactured and installed.

6kV isolation voltage separator, interrupting the UART RX and TX lines.

USB communication is based on Virtual Serial Port (VCP) technology using an MCP 2200 integrated circuit. It is powered by the voltage supplied by the USB port of the PC and is therefore independent of the unit status

4. Conclusions

This article describes the design of magnetic testing equipment under development at the University of Dunaujvaros. The apparatus is capable of determining the B-H curve of small-volume ferromagnetic material samples using a homogeneous stationary magnetic field (H) produced inside a solenoid. A fluxgate sensor was used in order to measure the magnetic field (B) of the sample. The main units are solenoid, solenoid drive unit, central measurement control unit, power supply and PC side software.

The development of the equipment is closely linked to research improving the efficiency of electric motors, which, inter alia, aims to reduce iron loss by using amorphous materials. The development of precise molding/die-cutting technology for these materials is essential for their application in the construction of electric motors. The technological parameters of the cut must be determined in such a way as to minimize the degrades of the excellent magnetic properties of the raw material.

Acknowledgement

This work is supported by the EFOP-3.6.1-16-2016-00003 and EFOP-3.6.2-16-2017-00016 project. Both of the projects are co-financed by the European Union.

References

- [1] Wang Z. et al.: *Development of an Axial Gap Motor With Amorphous Metal Cores*. IEEE Transactions on Industry Applications, 47/3. (2011) 1293–1299. <https://doi.org/10.1109/TIA.2011.2127430>
- [2] Kolano R., Krykowski K., Kolano-Burian A., Polak M., Szynowski J., Zackiewicz P.: *Amorphous Soft Magnetic Materials for the Stator of a Novel High-Speed PMBLDC Motor*. IEEE Transactions on Magnetics, 49/4. (2013) 1367–1371. <https://doi.org/10.1109/TMAG.2012.2234757>
- [3] Krings A., Boglietti A., Cavagnino A., Sprague S.: *Soft Magnetic Material Status and Trends in Electric Machines*. IEEE Transactions on Industrial Electronics, 64/3. (2017) 2405–2414, March. <https://doi.org/10.1109/TIE.2016.2613844>
- [4] Yang W., Huang C., Zhang Q.: *Optimization of Squirrel-Cage Rotor for Amorphous Asynchronous Motor*. Chinese Automation Congress (CAC), Hangzhou, China, 2019, 2107–2110.
- [5] A BIZOTTSÁG (EU) 2019/1781. rendelete (2019. október 1.) az elektromos motorokra és a frekvenciaváltókra vonatkozó környezettudatos tervezési követelményeknek a 2009/125/EK európai parlamenti és tanácsi irányelv szerinti megállapításáról, a 641/2009/EK rendeletnek a tömszelence nélküli önálló keringetőszivattyúkra és a termékbe beépített tömszelence nélküli keringetőszivattyúkra vonatkozó környezettudatos tervezési követelmények tekintetében történő módosításáról és a 640/2009/EK bizottsági rendelet hatályon kívül helyezéséről
- [6] Global Efficiency Intelligence LLC.: *Global Industrial Motor Systems Efficiency Initiative*, <https://www.globalefficiencyintel.com/global-industrial-motor-systems-initiative>, January, 2020
- [7] Szabo A., Koti D., Santa O., Kozsely G.: *Development of the Shaping Method of Amorphous Ribbons Used in Electric Drives*. XXXVI. International Colloquium Advanced Manufacturing and Repair Technologies in Vehicle Industry, Vol. XIX, 2019.
- [8] Waide P., Brunner C.: *Energy-Efficiency Policy Opportunities for Electric Motor-Driven Systems*. IEA Energy Papers, 7. (2011), OECD Publishing, <https://doi.org/10.1787/5kkg52gb9gjd-en>
- [9] Sheiretov Y.: *Deep Penetration Magnetoquasistatic Sensors*. Doctor of Philosophy at the Massachusetts Institute of Technology, June 2001
- [10] Dirk Ettl.: *Conception et fabrication d'un magnétomètre à jauge de contrainte*. Université de Grenoble, 2012, French, <https://tel.archives-ouvertes.fr/tel-00744722>

Earing Prediction of Unidirectionally and Cross-rolled, Annealed AW-5056 Al Sheets from {h00} Pole Figures

Bence SCHWEITZER,¹ Márton BENKE,² Adrienn HLAVACS,³ Valéria MERTINGER⁴

Institution of Physical Metallurgy, Metalforming and Nanotechnology (University of Miskolc, Faculty of Materials Science and Engineering), Miskolc, Hungary,

¹ thebencyx@gmail.com

² fembenke@uni-miskolc.hu

³ femhadri@uni-miskolc.hu

⁴ femvali@uni-miskolc.hu

Abstract

Earing of deep drawn cups is an effective measure of plastic anisotropy. It is the result of crystallographic anisotropy, i.e. texture. There are several methods to predict earing, but all of these methods are rather complex. Furthermore, above a certain sheet thickness, deep drawing cannot be performed, and prediction methods fail since they are usually valid within a certain sheet thickness range. A new, simple method has been proposed to predict earing. Besides simplicity, another major benefit of the method is that it can be applied to a wide range of sheet thicknesses. The method has been previously applied for unidirectionally rolled and recrystallized and cross-rolled Al sheets. In the present manuscript, the proposed method is applied on the AW-5056 type, unidirectionally and cross-rolled, then annealed Al sheets having very weak (close to random) structure. It is shown that for such samples, the method predicts negligible earing. It is also revealed that for the 5056 type Al alloy, the differences in texture and earing between unidirectionally and cross-rolled samples become so small after annealing, that the benefit of cross rolling is negligible.

Keywords: *cross-rolling, earing, texture.*

1. Introduction

The term “cross-rolling” is used for several special types of rolling [1]. In this manuscript, cross-rolling refers to a modified version of conventional “unidirectional rolling” during which the sheets are rotated by 90° about the normal direction (ND) between consecutive passes [2–5]. The result of such a process is a more random texture compared to unidirectional rolling with four-fold symmetry. Li et al. obtained a higher orientation scatter on the rolling plane of Mg sheets [2]. Wronski et al. applied cross-rolling to low carbon steel and copper and established that the anisotropy of plastic formability decreased in copper but increased in the steel [3]. Huh et al. achieved the suppression of cube texture formation in 5182 type Al sheets which resulted in better formability [4]. Tang et al. reported that on cross-rolled

AZ31 type magnesium sheets, negligible earing and increased ductility were obtained [5]. It can be concluded that in general, using cross-rolling, a more random texture and consequently, a more uniform plastic formability can be achieved.

Deep drawing is a simple method to characterize the plastic anisotropy of rolled sheets. Besides this, several methods have been developed to predict earing. Fukui and Kudo showed that earing can be predicted from the Lankford number: $\Delta r = (r_0 + r_{90}) / 2 - r_{45}$ [6]. Since then, reports have been published about mechanics based [7], crystallography based [8, 9] and more sophisticated methods [10]. Nowadays, earing is usually estimated with finite element (FE) methods [11]. One drawback of the above prediction methods is that they are valid within given sheet thickness ranges. If sheet thickness is out of this range, the mod-

el must be modified and validated. This becomes crucial if such sheet thickness is the target, where deep drawing cannot be carried out, thus, the method cannot be validated. A simple method has been published recently by the authors which is able to predict earing from $\{h00\}$ pole figures [12, 13]. Besides simplicity, the developed method can be applied in a wide sheet thickness range, which makes it a generally applicable method. Furthermore, it can be used on pole figures obtained by EBSD, or by non-destructive (sample-cutting-free) texture measurement methods [14]. The method was successfully applied on unidirectionally cold rolled and subsequently annealed Al sheets showing the following four-fold earing types: rolling, close to zero and recrystallized earing, at notably different sheet thicknesses (0,3–3 mm) [12]. Later, it was applied on cross-rolled Al sheets as well [13]. The present manuscript aims to further widen the applicability of the developed earing prediction method. Now, the method is to be applied on unidirectionally (UD) and cross-rolled (CR) Al sheets which have been subsequently subjected to annealing heat treatments to obtain weak (almost random) recrystallization textures.

2. Materials and Methods

Sheets of 5056 aluminum with initial thickness of 4 mm were unidirectionally- (UD) and cross-rolled (CR) using a VonRoll roll stand. Except for the type of rolling (UD or CR), the applied parameters were similar. Sheets were produced with both 6 and 12 passes. Samples A1, A5, and A6 were UD rolled, while samples A3K, A4K, and A9K were CR rolled to ~1 mm in 6 passes. Between consecutive passes, sample A4K was rotated around ND clockwise, while samples A3K and A9K were rotated back and forth. The height reduction of the first pass was 0.6 mm, and 0.5 mm for the subsequent passes. Sample A10 was UD rolled and sample A11K was CR rolled to ~1 mm in 12 passes. The height reduction for the first pass was 0.3 mm and 0.25 for the following passes. Sample A11K was also rotated back and forth around ND [13]. The rolled sheets were heat treated in an air atmosphere furnace at 320°C for 2 hours to obtain a fully recrystallized structure.

Round samples with 30 mm diameter were cut out from the sheets for X-ray diffraction texture measurements. Texture examinations were carried out using a Bruker D8 Advance X-ray diffractometer with Cu X-ray source equipped with an Eulerian cradle. The applied tube voltage and

current were 40 kV and 40 mA. $\{111\}$, $\{200\}$, and $\{220\}$ pole figures were measured up to 75° tilting. Recalculated $\{200\}$ pole figures were obtained with the software of the equipment, TexEval. Orthotropic deformation was applied for the recalculation of both UD and CR samples.

The used earing prediction method is described in detail in a previous publication [12]. In brief, the CHI-cuts of the recalculated $\{200\}$ pole figures were obtained. The $\{200\}$ CHI-cuts were plotted for each PHI (sample rotation) angle. The method supposes that the intensity variation on the CHI-cuts can be approximated with a sum of Gaussian curves [15]. The CHI-cuts were fitted with Gaussian curves. The net intensity (area) of each Gaussian curve was determined and weighted (multiplied) with the sine of the CHI values of the peaks of the Gaussian curves. Then, the weighted areas were summed to the given PHI angle. The summarized, weighted $\{200\}$ intensity function versus PHI is the predicted relative cup height variation versus PHI. Predicted average earing was calculated as the ratio of average predicted ear height and average predicted cup height and divided by a scaling factor [12]. The determination of the scaling factor was based on comparison to experimental data described in detail in [13]. The scaling factors for UD and CR cases were 40 and 60, respectively.

3. Results

3.1. Results of 6 Pass Rolling

Figure 1 shows the recalculated $\{200\}$ pole figures of the annealed UD and CR samples rolled in 6 passes. On the pole figures, no intensity peaks are present. The RD is at 12'o clock in every case. Thus, it can be said that all the UD and CR samples show a close to random structure.

In Figure 2 the predicted earing and predicted average earing of the annealed samples rolled in 6 passes are summarized. It can be seen that for all UD and CR samples, notable ears that are characteristic to rolling earing at RD + 45° + (n · 90°) directions or ears typical to recrystallized earing at RD + (n · 90°) directions (or any other directions) do not appear. The observed differences in cup height are very small, the intensity varies between 60 and 80 counts. Such differences are negligible. This is proved by the predicted average earing which is below 1. Thus, it can be said that all UD and CR samples show very weak earing.

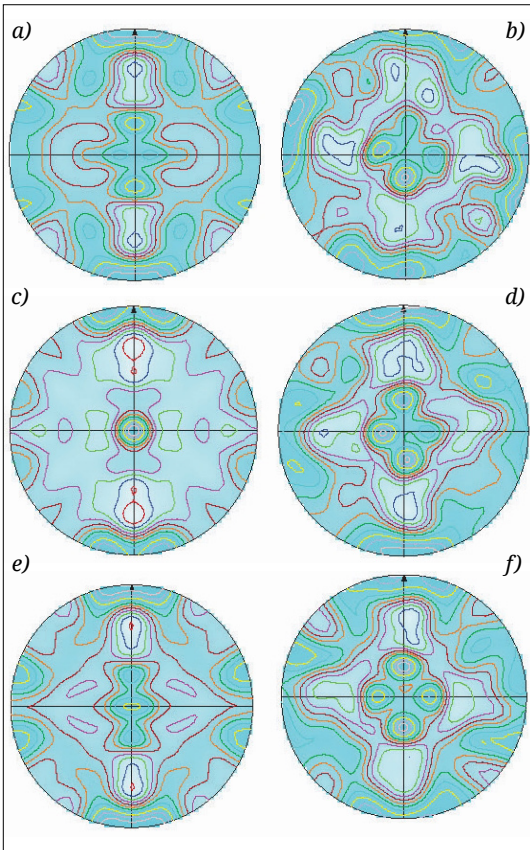


Figure 1. Recalculated {200} pole figures of the annealed samples rolled in 6 steps. (a) A1; (b) A3K; (c) A5; (d) A4K; (e) A6; (f) A9K.

3.2. Results of 12 Pass Rolling

In **Figure 3** the recalculated {200} pole figures of the annealed UD and CR samples rolled in 12 passes is presented. It is evident that the annealing heat treatment resulted a random structure in both UD and CR samples.

Figure 4 shows predicted earing and predicted average earing of the samples rolled in 12 passes. According to the figure, both UD and CR samples show weak earing. The predicted average earing is below 1.

4. Conclusions

It was seen that no intensity peaks appeared on the {200} pole figures of UD and CR rolled and subsequently annealed AW-5056 type Al sheets. Thus, a homogenous intensity distribution was present on the {200} pole figures (i.e., the rolling plane) of the examined samples. The developed earing prediction method is based on the intensity distribution of the {h00} pole figures i.e., the {h00} intensity distribution on the rolling plane. It is shown that in such cases, when a homogenous {200} intensity distribution is present on the rolling plane, very small cup height variations and weak average earing is obtained using the developed earing prediction method. It is also shown that for the AW-5056 type Al alloy, the differences in texture and earing between UD and CR samples become so small after annealing, that the benefit of cross rolling is negligible.

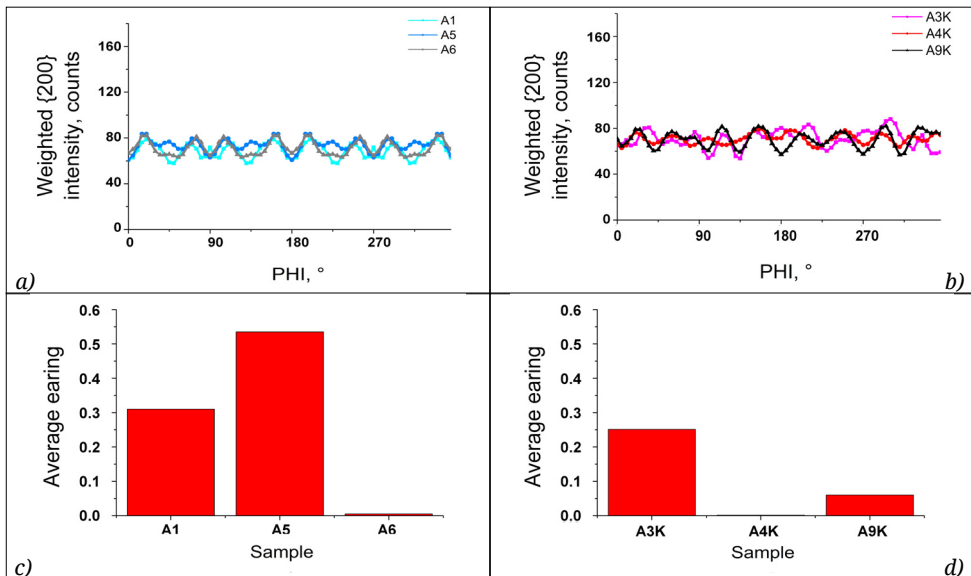


Figure 2. Predicted earing of the annealed samples rolled in 6 steps. (a) UD samples; (b) CR samples; (c) predicted average earing of the UD samples, (d) CR samples.

Acknowledgment

The described article was carried out as part of the EFOP-3.6.1-16-2016-00011 “Younger and Renewing University – Innovative Knowledge City – institutional development of the University of Miskolc aiming at intelligent specialization” project implemented in the framework of the Szechenyi 2020 program. The realization of this project is supported by the European Union, co-financed by the European Social Fund. Supported by the ÚNKP-19-4 New National Excellence Program of the Ministry for Innovation and Technology and the NKFIH K119566 project.

References

- [1] Neugebauer R., Glass R., Kolbe M., Hoffmann M.: *Optimisation of processing routes for cross rolling and spin extrusion*. J. Mater. Process. Tech. 125–126. (2002) 856–862.
[https://doi.org/10.1016/S0924-0136\(02\)00392-8](https://doi.org/10.1016/S0924-0136(02)00392-8)

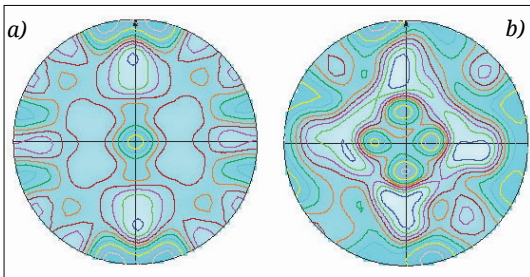


Figure 3. Recalculated $\{200\}$ pole figures of the annealed samples rolled in 12 steps. (a) A10; (b) A11K.

- [2] Li X., Al-Samman T.: *Mechanical properties and anisotropy of ME20 magnesium sheet produced by unidirectional and cross rolling*. Materials & Design 32. (2011) 4385–4393.
<https://doi.org/10.1016/j.matdes.2011.03.079>
- [3] Wronski S., Wrobel M., Baczanski A., Wierzbanski K.: *Effects of cross-rolling on residual stress, texture and plastic anisotropy in f.c.c. and b.c.c. metals*. Materials Characterization 77. (2013) 116–126.
<https://doi.org/10.1016/j.matchar.2013.01.005>
- [4] Huh M. Y., Cho S. Y., Engler O.: *Randomization of the annealing texture in aluminum 5182 sheet by cross-rolling*. Materials Science and Engineering A, A315. (2001) 35–46.
[https://doi.org/10.1016/S0921-5093\(01\)01207-2](https://doi.org/10.1016/S0921-5093(01)01207-2)
- [5] Tang W., Huang S., Li D., Peng, Y.: *Mechanical anisotropy and deep drawing behaviors of AZ31 magnesium alloy sheets produced by unidirectional and cross rolling*. Journal of Materials Processing Technology, 215. (2015) 320–326.
<https://doi.org/10.1016/j.jmatprot.2014.08.020>
- [6] Fukui S., Kudo H.: *The earing in deep-drawing and directionality in tension-test of sheet metal*. Rep. Inst. Sci. Tech. Univ. Tokyo, 4 (1950) 33.
- [7] Sowerby R., Johnson W.: *Prediction of earing in cups drawn from Anisotropic sheet using slip-line field theory*. Journal of Strain Analysis for Engineering Design, 9 (1974) 102–108.
<https://doi.org/10.1243%2F03093247V092102>
- [8] Tucker G. E. G.: *Texture and earing in deep drawing of aluminium*. Acta Metallurgica, 9 (1961) 275–286.
[https://doi.org/10.1016/0001-6160\(61\)90220-6](https://doi.org/10.1016/0001-6160(61)90220-6)

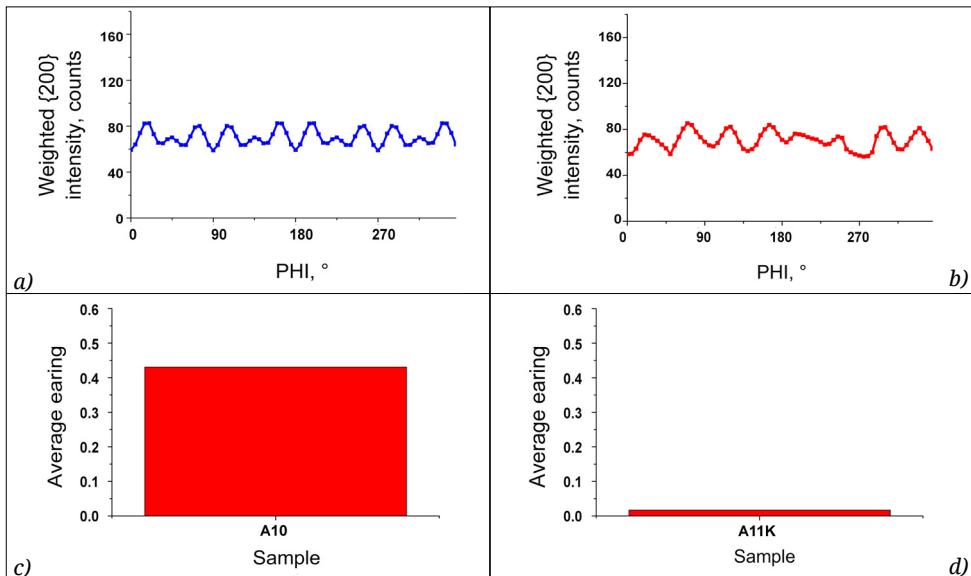


Figure 4. Predicted earing of the annealed samples rolled in 12 steps. (a) UD sample; (b) CR sample; (c) predicted average earing of the UD sample, (d) CR sample.

- [9] Kanatake N., Tozawa Y., Otani T.: *Calculations from texture of earing in deep drawing for fcc metal sheets. International Journal of Mechanical Sciences*, 25. (1983) 337–345.
[https://doi.org/10.1016/0020-7403\(83\)90012-7](https://doi.org/10.1016/0020-7403(83)90012-7)
- [10] Van Houtte P., Cauwenberg G., Aernoudt E.: *Analysis of the earing behaviour of aluminium 3004 alloys by means of a simple model based on yield loci calculated from orientation distribution functions. Materials Science and Engineering*, 95. (1987) 115–124.
[https://doi.org/10.1016/0025-5416\(87\)90503-9](https://doi.org/10.1016/0025-5416(87)90503-9)
- [11] Engler O., Mertens N., Van Dam P.: *Texture-based design of a convoluted cut-edge for earing-free beverage cans. Journal of Materials Processing Technology*, 211. (2011) 1278–1284.
<https://doi.org/10.1016/j.jmatprotec.2011.02.011>
- [12] Benke M., Hlavacs A., Imre P., Mertinger V.: *Prediction of earing of aluminium sheets from {h00} pole figures. European Journal of Mechanics endash; A/Solids*, 81. (2020) 103950.
<https://doi.org/10.1016/j.euromech-sol.2020.103950>
- [13] Benke M., Schweitzer B., Hlavacs A., Mertinger V.: *Prediction of earing of cross-rolled Al sheets from {h00} pole figures. Metals - Open Access Metallurgy Journal*, 10/2. (2020) 192.
<https://doi.org/10.3390/met10020192>
- [14] Sepsi M., Mertinger V., Benke M.: *Sample cutting-free pole figure measurement method for centreless diffractometers in modified X mode. Materials Characterization*, 151. (2019) 351–357.
<https://doi.org/10.1016/j.matchar.2019.03.031>
- [15] Ma Q., Mao W., Feng H., Yu Y.: *Rapid texture measurement of cold-rolled aluminum sheet by X-ray diffraction. Scripta Materialia*, 54. (2006) 1901–1905.

Investigation of the Property Change in FINEMET Alloy After Conventional, Pulse and Mechanical Stress Annealing

Attila SZABÓ,¹ Róbert SÁNTA,² Antal LOVAS,³ László NOVÁK⁴

¹ University of Dunaujvaros, Department of Mechanical Engineering, Dunaujvaros, Hungary, szaboattila@uniduna.hu

² University of Dunaujvaros, Department of Mechanical Engineering, Dunaujvaros, Hungary, santarobert@uniduna.hu

³ Budapest University of Technology and Economics, Faculty of Transportation Engineering, Department of Automotive technologies, Budapest, Hungary, antal.lovas@gjt.bme.hu

⁴ Technical University of Kosice, Department of Physics, Kosice, Slovakia, Technical University of Kosice, ladislav.novak@tuke.sk

Abstract

In the present work the comparison of the effect of traditional, pulse and stress annealing is made by monitoring the important mechanical and magnetic properties of FINEMET type amorphous precursor alloy. The magnetic properties were determined from the shape of magnetization curve (coercive force, anisotropy) during various heat treatments and the mechanical properties were measured using brittleness test. The traditional heat treatments were performed in resistance furnace and the magnetic measurements were performed in astatic magnetometer. The pulse and stress annealing (as well as their combinations) were carried out inside in the magnetometer. The temperature of pulse heat treatments is regulated with the length of current pulse flowing through the sample. After each pulses the magnetization curves were measured in-situ, in the magnetometer.

Keywords: pulse heat treatment, FNEMET, amorphous, nano-crystalline, brittleness.

1. Introduction

In recent decades, Fe-based nanocrystalline alloys have become fundamental in the production of soft magnetic materials. The excellent properties are developed via thermal decomposition of the FINEMET ($\text{Fe}_{73.5}\text{Si}_{13.5}\text{B}_9\text{Nb}_3\text{Cu}_1$), amorphous precursor [1]. It is believed, that the nanometer-size α -Fe (Si) grain structure plays a basic role in the development of the extra-ordinary properties [2]. The onset-temperature of amorphous-phase decomposition can be altered even in the same crystallization reaction, resulting in different size distribution [3]. The minimum grain-size is expected to be formed when the temperature of crystallization is around the 0.5 times the melting point of the alloy in question [4]. The magnetic softness is reflected in the magnitude of coercivity which exhibits an inverse-like relation in several soft magnetic alloys of average grain

size. However, this relation breaks down in the range of 100-1 nm grain diameters in FeSiB-alloys. This exceptional behaviour is attributed to the coincidence between the magnetic correlation length and the grain diameters. The rapid drop is believed to be the consequence of an averaging of crystal anisotropy within the domain wall thickness in these alloys [2]. This grain-size lowering is extremely sharp in the case of Fe(SiB) based glasses.

The phenomenon is attributed to the coincidence between the magnetic correlation length and the average grain diameters causing the crystal anisotropy averaging over the dimension of the domain wall thickness (~100 nm in these alloys).

However the nanometer-sized grain dimension is not the only reason for the development of excellent magnetic softness. Only those of nano-crystalline alloys exhibit magnetic ultrasoft-

ness, in which the nanograin system is developed from the glassy precursor via “primary reaction” [5]. This reaction is the first step during the amorphous phase decomposition of hypo-eutectic Fe-B glasses. Hence, this two-step mechanism can be regarded as the proto-type for the nano-crystallization in FINEMET ($\text{Fe}_{73.5}\text{Si}_{13.5}\text{B}_9\text{Nb}_3\text{Cu}_1$) precursors [6]. This transformation has been analysed in several references [7–9]. There is general agreement concerning the importance of separation of the first and second steps of crystallization, because magnetically hard, inter-metallic particles precipitate during the second crystallization step, destroying the soft magnetic character of the alloy. This separation is enhanced by the addition of appropriate alloying elements into the precursor glass. The addition of the nucleating element (Cu) (enhancement the nucleation of $\alpha\text{-Fe}$ particles) has an outstanding significance from the point of view of ensuring homogeneous distribution of nuclei formation [10], but also contributes to separation of crystallization steps belonging to the $\alpha\text{-Fe}(\text{Si})$ and Fe_3B formation. The Nb addition contributes to the retardation of Fe_3B precipitation (crystalline inter-metallic compound) avoiding the magnetic hardening [11]. The Si addition ensures the overall stabilization of the glassy state.

The temperature of $\alpha\text{-Fe}$ nucleation in hypo-eutectic Fe-B glassy alloys is lowered by the Cu addition [12]. The essence is the “catalytic” mechanism of eutectoid type decomposition of the fcc environments being entrapped during liquid quenching [13]. The preferential solubility of Cu in fcc (γ) Fe environments, $\gamma\text{-Fe}$ type symmetries are quenched into the amorphous matrix, which are inactive during the magnetization process, i.e. the domain wall displacement is hindered. As the temperature increases during heat treatment, the γ -centres decompose at first, via an eutectoid mechanism, as the activation energy of Cu diffusion is low [14, 15]. The outlined mechanism is also supported by the experiments [6]. Hence, itself this nucleation phenomenon also contributes to the suppression of coercivity prior to the development of nanocrystalline structure [13].

The traditional nanocrystallizations are performed by isothermal heat treatments at around 540 °C, 1h, when the DO3 ordered phase is formed, which is $\alpha\text{-Fe}(\text{Si})$ solid solution. The Nb and B are enriched in the remaining amorphous phase. Recently, “pulse heat treatments” and stress annealing (annealing combined with longitudinal stress) [16] were also studied for tailoring the soft magnetic properties.

Though several outlined methods are applied even in the industrial praxis already, some details of the physical background of property tailoring is still open. Mainly the knowledge of atomic level mechanism of coercivity and brittleness evolution is insufficient during the various heat treatment types. This topic is the focus of the present paper.

2. Experimental

2.1. Materials, heat treatments and measuring methods

The well-known FINEMET alloys are applied in the experiments. The samples purchased were 10 mm width, 30 μm thickness and length was set to 100 mm with scissors. Impulse heating was performed by alternating the current pulses with the peak current of approximately 10A, the frequency was set to 50Hz. Pulse duration was 0.08-0.12 sec. Samples were heat treated with this method without applying forced air cooling. The estimated cooling rate was about 100 K/s and the thermal heating rate was about 1000 K/s. The magnetic measurements were performed in-situ during the heat treating process in an astatic magnetometer. The coercive force (H_c) was determined from the magnetization curves, which are plotted after each individual pulse.

In **Figure 1** examples are shown for the time dependence of temperature caused by individual pulses of different length, representing different energies. The details of measurement and the evaluation of results are described in [16].

The relative strain at fracture (ε_f) is determined from simple bending test by bending the ribbons of thickness d between two parallel plates to a semicircle of radius $r = D/2$, where D denotes the distance between the two plates. At fracture, ε_f is evaluated from the expression $\varepsilon_f = d / (D - d)$ described in [17, 18].

Stress annealing was also applied using case external uniaxial stress ($\sigma = 0, 2$ and 4 MPa) combining the traditional or pulse treatments with longitudinal stress during the time-period of sample heating. The longitudinal stress was applied to the weights placed on the samples inside in the magnetometer.

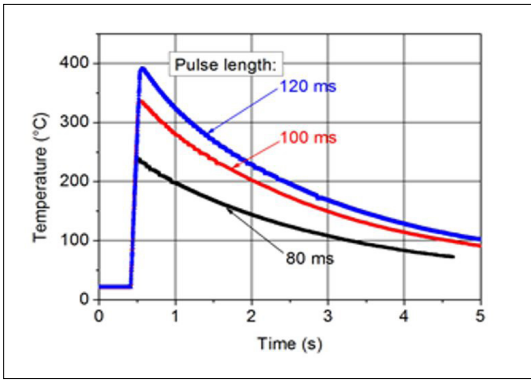


Figure 1. The time dependencies of temperature using pulses of different length measured on sample FINEMET [16].

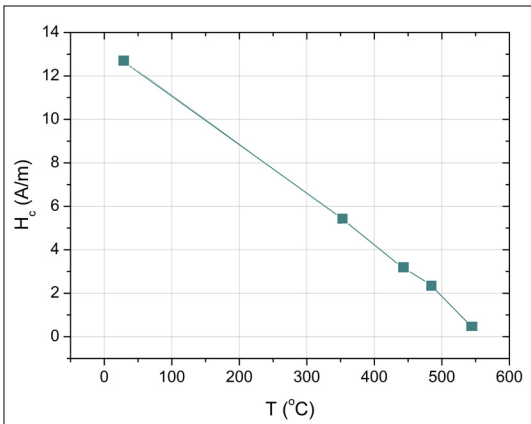


Figure 2. The change of H_c in FINEMET precursor versus the temperature of isothermal 1h heat treatments [19].

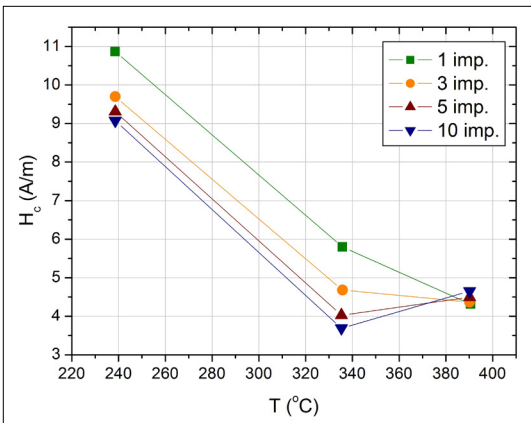


Figure 3. Correlation between coercivity and the maximum temperature attained by different pulse number and pulse length.

3. Results and discussion

3.1. Temperature dependence of coercivity during isothermal heat treatments

The change of magnetic properties during amorphous nanocrystalline transformation are reported in several papers [6, 18]. A typical trend is illustrated in Figure 2, where the H_c of FINEMET samples are plotted versus the temperature of isothermal (1h) annealing. This result is regarded as reference tendency for the appreciation of the impact of pulse treatments.

The net H_c decrease originates from two, slightly overlapping physical processes: In the low temperature range the H_c lowering arises solely from the structural relaxation ($T_{\text{anneal}} < 350$ °C), which consists of short range arrangement, containing also bond reorientation between the frozen contacting atoms, without long range diffusion. More, than the 50 % of the total H_c decrease originates from this process. No trace of crystal nucleation is detected in this temperature range. Beyond 400 °C the additional H_c decrease arises from crystal nucleation and growth of nano-crystals. In this process diffusion over medium range order is also involved.

The further decrease of H_c by nearly a magnitude treatment is typical in these alloys. Within this temperature interval nanometer-sized DO3 type grain assembly is developed, which is Fe (Si) solid solution. This process is completed at around 540 °C. The H_c lowering in the early stage of crystallization is unexpected in the Fe-B alloys. Just the opposite tendency is experienced in the binary glasses [20]. The significant lowering is interpreted by the enhanced elimination of γ -trapping centers by the entrapped Cu-atoms via the eutectoidal reaction, so the mechanism of catalytic effect of Cu-atoms on the γ -center elimination is an eutectoidal reaction, starting from the fcc environments.

In Figure 3 the H_c evolution is depicted versus the increasing peak temperature for several independent series of pulses (see Figure 1). It was detected that peak temperature depends predominantly on the pulse length (Figure 1). Consequently, the highest H_c depression is expected at the highest peak temperature applied in the experiments. At the 0.1 s pulse length, the peak temperature is nearly 350 °C. The impact of a single pulse on H_c suppression is nearly the same as that for the 1h isothermal heat treatment at the same temperature, indicating that magnetic stress re-

laxation is an extremely rapid process, presumably of the non-diffusive nature of this relaxation mechanism.

This observation is also supported by the series of measurements, collected in Figure 4. Here, the H_c lowering is plotted for different (increasing) pulse lengths (0.08 s, 0.10 s and 0.12 s). Again, these independent measurements were performed in-situ in the magnetometer, subsequently the individual pulses. It is remarkable, that H_c decrease is negligible during the pulse series, except the first heat pulse. On the other hand, it is also clear, that peak temperature (or the magnitude of activation energy) has a dominant role in the kinetics of H_c decrease. In the period of structural relaxation, the H_c decrease is coupled solely with short range atomic rearrangements within these – sterically independent – quenched-in stress centres. As the peak temperature of pulses is high enough, the population density of these centres rapidly decreases.

3.2. Pulse heat treatments in external (axial) field

A longitudinal external field was also applied in order to study the interaction between the thermal activation and the outer magnetic field in the evolution of coercivity during the series of individual pulses. The easy direction of magnetization in soft magnetic rapidly quenched ribbons is along the ribbon length. The direction of magnetic field produced by the magnetometer is parallel with this easy direction of magnetization of the ribbon.

If the longitudinal magnetic field is applied during the heat pulse, the slope of H_c curves increases versus the pulse number, which means that longitudinal field (similarly to the traditional heat treatments) promotes the H_c decrease (see Figure 6.). In these experiments 0.08 s pulse length is applied. In such circumstances (≈ 240 °C peak temperature) grain nucleation and growth is excluded, only stress relaxation is the uncial mechanism in the H_c lowering. The role of the longitudinal field is similar at higher, 0.1 pulse length (see Figure 7.), but after successive 0.12 s pulses, the value of H_c is identical with that obtained after 1h isothermal heat treatment at the appropriate temperature ≈ 400 °C (reaches the H_c measured in nano-crystalline state) (see Figure 6.).

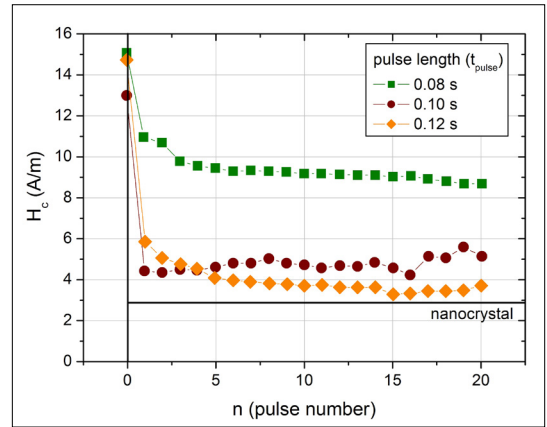


Figure 4. Coercivity change versus the applied pulse number in the case of different pulse length (peak temperature).

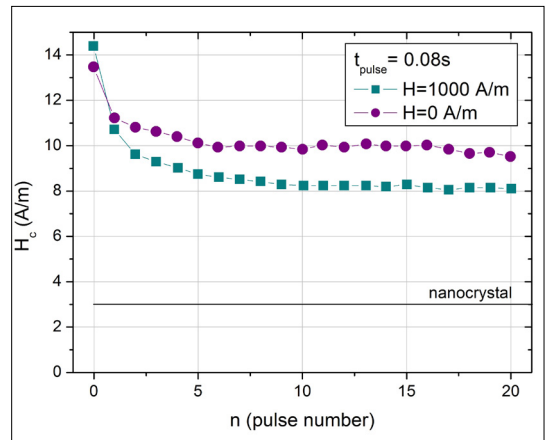


Figure 5. The role of 1000 A/m field on H_c evolution during the series of 0.08 s length pulses.

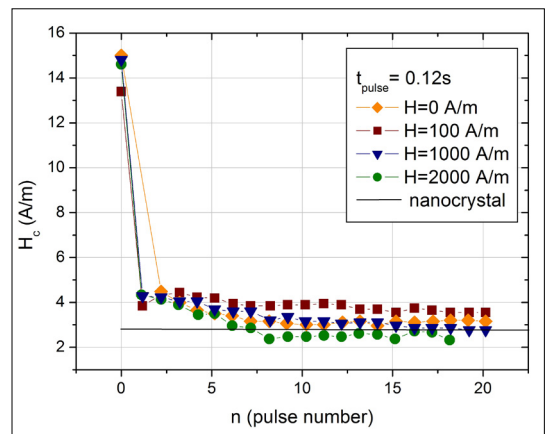


Figure 6. The influence of field strength on H_c during the series of 0.12 s length pulses.

3.3. Pulse heat treatments in axial field and load

From a thermodynamic point of view the metallic glasses are a single phase homogeneous continuum. In spite of this, many physical properties do exhibit significant macroscopic anisotropy (difference in mechanical properties in longitudinal and rectangular direction, or the difference in the mechanical response to the hydrogen absorption at the opposite side of ribbon surfaces).

Such effects hint at the difference between the local cooling rate on the opposite side of ribbons. One can suppose a coupling between the local cooling rate, the population density and distribution of the quenched-in stress centres, which can be coupled with the stress sensitive properties like H_c or even the quenched-in anisotropy. Such tendencies can be recognized in the **Figure 7**, where the coercive force is monitored during the series of pulse annealing of FINEMET alloys.

The measurement was carried out also in a longitudinal magnetic field and under longitudinal mechanical stress. As **Figure 7** shows, the H_c of quenched ribbons (0 pulse) slightly decreases, when longitudinal field or stress was applied during the measurements due to the small positive magnetostriction of this alloy. The role of longitudinal field and load is obvious: It is remarkable, that H_c breaks down due to the applied load already after the first impulse (peak temperature ≈ 330 °C, 0.1 s pulse length) approaches the value of completely nano-crystallized structure in spite of the obvious absence of nano-crystalline structure at this temperature.

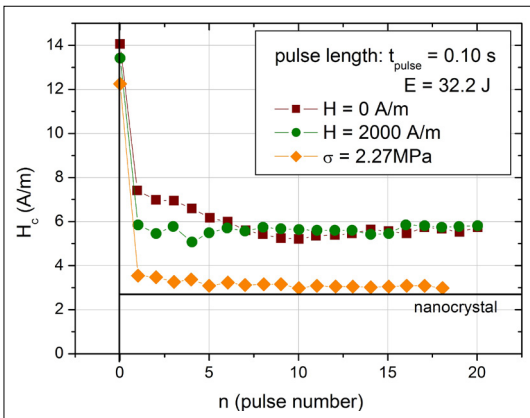


Figure 7. The evaluation of H_c versus the series of isotherm pulses during the independent measurements-longitudinal field and stress were also applied.

3.4. The origin and evolution of brittleness of glassy alloys

Several atomic level mechanisms do contribute to the evolution of brittleness in metallic glasses. The significant brittleness difference between metallic glasses originates partially from the different composition or from the various thermal history [21]. The brittleness of Fe-based as quenched glasses arise dominantly from the metalloids contents which ensures simultaneously the sufficient glass forming ability (mainly the B, P and Si content). Hence, the ductility or the degree of brittleness [18] is mainly composition specific in transition metal-metalloid based glasses, i.e. no direct relation exists between the crystal nuclei formation and the brittleness evolution. A typical example is the Fe100-xBx binary system. When the hypo- and hyper-eutectic glasses (low and high B-content) are compared, the hyper-eutectic glasses are less flexible (more brittle) in spite of the perfectly X-ray amorphous nature of ribbons. The reason is the increasing covalent bonding character with the increasing B-content in the hyper-eutectic region of Fe100-xBx glasses. In general, the tendency of brittleness is in direct correlation with the hardness (HV) of the as quenched Fe-B samples [21]. Increasing brittleness is also experienced at the crystallization onset, being also supported by the high resolution diffraction techniques.

The theoretical treatment of brittleness evolution is based on the free volume theory of glass formation [22, 23]. The macroscopic shear viscosity is supposed to describe the connection between the shear viscosity $\eta(T)$ and the average free volume v per atom. ΔG_m is the activation energy of displacement, v^* the critical free volume fluctuation, γ a geometrical factor between 0.5 and 1, and C is a constant:

$$\eta(T) = CRT \exp\left(-\frac{\Delta G_m}{RT}\right) \exp\left(\frac{\gamma v^*}{v}\right) \quad (1)$$

This macroscopic tendency of viscosity change is considered as the phenomenological background for the evolution of brittleness in the rapidly quenched sample. According to [22, 23], there is a coupling between the kinetics of annealing out of the quenched-in free volume and the brittleness. The free volume is cooling rate dependent, resulting stress gradient across the sample thickness.

According to the outlined consideration, the evolution of brittle behaviour is the consequence of different rates of free volume annihilation

between opposite surfaces, which also manifested in the spontaneous deformation of the samples during heat treatments.

In the case of the investigated FINEMET alloys the development of (magnetically and mechanically) hard particles (precipitates at high temperature ($T_{\text{anneal}} \approx 600 \text{ }^\circ\text{C}$) so this sudden increase of brittleness (see in Figure 8.) seems to arise from relaxation ($T_{\text{anneal}} \approx 330 \text{ }^\circ\text{C}$). The outlined considerations are experimentally supported by the Figure 8. The change of brittleness versus the pulse number for various pulse length is illustrated in Figure 9. The series of 0.08 sec pulse length (max. peak temperature is around $240 \text{ }^\circ\text{C}$) the flexibility of ribbons is sustained over the entire period of pulse series (20 pulses) i.e. no brittleness can be detected. In spite of this, significant H_c decrease occurs during the same circumstances (see Figure 5.). In contrast, when the pulse length is slightly increased (pulse length 0.09 s, with peak

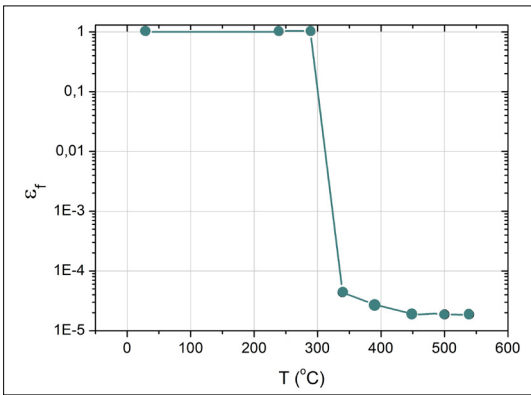


Figure 8. The change of brittleness of FINEMET sample during isothermal heat treatments.

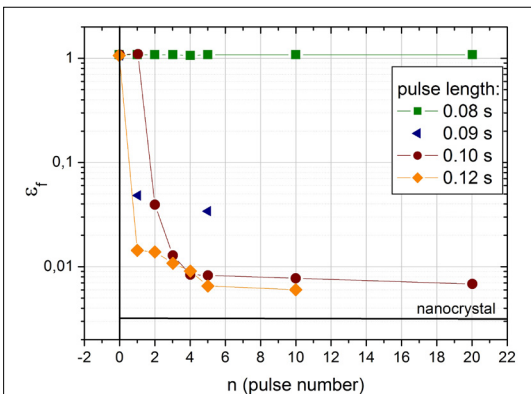


Figure 9. The change of brittleness of FINEMET sample versus the pulse number for various pulse length.

temperature of $292 \text{ }^\circ\text{C}$) sudden breakdown of flexibility is experienced even after the first pulse. As the pulse length approaches 0.1 s, the brittleness also approaches the values obtained after isothermal heat treatments. According to the Figures 8 and 9 the temperature of heat treatment has a dominant role in the degree of brittleness, the duration of heat treatment has only secondary significance.

The degree of brittleness is generally lower in the case of pulse heat treatments (compare Figure 8 and 9.).

4. Conclusions

The impact of traditional (isotherm) impulse and stress annealing was compared in the property evaluation of FINEMET alloys. Pulse and stress annealing (as well as their combinations) were carried out inside in a magnetometer, where the magnetic measurements were carried out after each pulses, in-situ. The temperature of pulse heat treatments was regulated with the length of current pulse. In the experiments a coercive force lowering and HV increase can be detected already during the structural relaxation phase, however a more significant HV increase and H_c decrease is experienced only after partial crystallisation. During the research, the following conclusions were drawn:

Significant (more than 50 %) H_c lowering can be detected during structural relaxation (below $300 \text{ }^\circ\text{C}$) in FINEMET type precursor alloy, without the appearance of crystal nuclei formation.

The contribution of heat treatment temperature is predominant in the degree of H_c lowering and also in embrittlement evolution.

Solely short range atomic rearrangements are responsible in both of property changes.

The impact of longitudinal stress is similar to the effect of a longitudinal magnetic field during heat treatment, i.e. the decrease of coercive force (H_c) accelerates, when the annealing in magnetic field and external mechanical stress are simultaneously applied.

Acknowledgements

The research presented in this paper was carried out as part of the EFOP-3.6.2-16-2017-00016 and EFOP-3.6.1-16-2016-0003 projects in the framework of the New Széchenyi Plan. The completion of this project is funded by the European Union and co-financed by the European Social Fund.

References

- [1] Makino M., Inoue A., Masumoto T.: *Nanocrystalline Soft Magnetic F-M-B (M=Zr, Hf, Nb) Alloys Produced by Crystallization of Amorphous Phase*. Materials Transactions JIM, 36/7. (1995) 924–938. <https://doi.org/10.2320/matertrans1989.36.924>
- [2] Herzer G.: *Nanocrystalline soft magnetic alloys*. In: Handbook of Magnetic Materials. (Szerk.: Buschow K. H. J.) Elsevier Science, Amsterdam, 10/3. 1997. 415–462. [https://doi.org/10.1016/S1567-2719\(97\)10007-5](https://doi.org/10.1016/S1567-2719(97)10007-5)
- [3] Lu K., Wang Y. Z., Wei W. D., Li Y. Y.: *The temperature dependence of specific resistance for nanocrystalline alloys with different average grain size*. Advanced Cryogenic Materials, 38. (1991) 285.
- [4] Lu K.: *Nanocrystalline metals crystallized from amorphous solids nanocrystallization, structure and properties*. Materials Science and Engineering R., 16/4. (1996) 161–221. [https://doi.org/10.1016/0927-796X\(95\)00187-5](https://doi.org/10.1016/0927-796X(95)00187-5)
- [5] Scott M. G.: *Crystallization in Amorphous Metallic Alloys*. In: Butterworths Monographs in Materials (Szerk.: Luborsky F. E.) Butterworth & Co (Publishers) Ltd., London, 1983. 144–168.
- [6] Lovas A., Kiss L. F., Varga B., Kamas P., Balogh I., Bakonyi L.: *Survey of magnetic properties during and after amorphous-nanocrystalline transformation*. Journal of Physics IV., 8/2. (1998) 291–298.
- [7] Yamauchi K., Yoshizawa Y.: *Recent development of nanocrystalline soft magnetic alloys*. NanoStructured Materials, 6. (1995) 247–254. [https://doi.org/10.1016/0965-9773\(95\)00048-8](https://doi.org/10.1016/0965-9773(95)00048-8)
- [8] Yoshizawa Y., Yamauchi K.: *Effects of magnetic field annealing on magnetic properties in ultrafine crystalline Fe-Cu-Nb-Si-B alloys*. IEEE Transactions on Magnetics, 25/5. (1989) 3324–3326. <https://doi.org/10.1109/20.42291>
- [9] Ayers J. D., Harris V. G., Sprague J. A., Elam W. T., Jones H. N.: *A model for nucleation of nanocrystals in the soft magnetic alloy $Fe_{73.5}Nb_3Cu_1Si_{13.5}B_9$* . NanoStructured Materials, 9. (1997) 391–396. [https://doi.org/10.1016/S0965-9773\(97\)00091-3](https://doi.org/10.1016/S0965-9773(97)00091-3)
- [10] Hono K., Ping D.H., Ohnuma M. Onodera H.: *Cu clustering and Si partitioning in the early crystallization stage of an $Fe_{73.5}Si_{13.5}B_9Nb_3Cu_1$ amorphous alloy*. Acta Materialia, 47/3. (1999) 997–1006. [https://doi.org/10.1016/S1359-6454\(98\)00392-9](https://doi.org/10.1016/S1359-6454(98)00392-9)
- [11] Lovas A., Kisdi-Koszó É., Konczos G., Potocky L., Vértesy G.: *Casting of ferromagnetic amorphous ribbons for electric and electrotechnical applications*. Philosophical Magazine B, 61. (1990) 549–565.
- [12] Varga B., Lovas A., Ye F., Gu X. J., Lu K.: *Pressure dependence of nanocrystallization in amorphous $Fe_{86}B_{14}$ and $Fe_{85}Cu_1B_{14}$ alloys*. Materials Science and Engineering: A, 286. (2000) 193–196. [https://doi.org/10.1016/S0921-5093\(00\)00634-1](https://doi.org/10.1016/S0921-5093(00)00634-1)
- [13] Lindqvist P. A., Uhrenius B.: *On the Fe-Cu phase diagram*. Calphad, 4/3. (1980) 193–200.
- [14] Lovas A., Kiss L. F., Balogh I.: *Saturation magnetization and amorphous Curie point changes during the early stage of amorphous-nanocrystalline transformation of a FINEMET-type alloy*. Journal of Magnetism and Magnetic Materials, 215–216. (2000) 463–465. [https://doi.org/10.1016/S0304-8853\(00\)00189-X](https://doi.org/10.1016/S0304-8853(00)00189-X)
- [15] Kovac J., Novák L., Hubac L.: *Impulse annealing as possibility of modification of magnetic properties of amorphous metallic alloys*. Journal of Electrical Engineering, 66/7s. (2015) 142–145.
- [16] Mehrer H.: *Diffusion in Solids – Fundamentals, Methods, Materials, Diffusion-Controlled Processes*. 1. kiadás. Springer-Verlag, Berlin–Heidelberg, 2007.
- [17] Gerling R., Wagner R.: *Properties of in-core reactor-irradiated amorphous $Fe_{40}Ni_{40}B_{20}$* . Journal of Nuclear Materials, 107. (1982) 311–317. [https://doi.org/10.1016/0022-3115\(82\)90430-5](https://doi.org/10.1016/0022-3115(82)90430-5)
- [18] Herzer G.: *Nanocrystalline soft magnetic alloys*. In: Handbook of Magnetic Materials. (Szerk.: Buschow K. H. J.) Elsevier Science, Amsterdam, 10/3. 1997. 415–462.
- [19] Hubas L., Novak L., Balla S., Lovas A.: *Evolution of magnetic and mechanical properties in FINEMET-type precursor glasses during isothermal and pulse heat treatments*. Acta Physica Polonica A, 131/4. (2017) 672. <https://doi.org/10.12693/APhysPolA.131.672>
- [20] Weltsch Z., Klam K., Lovas A.: *Comparison of hardness and coercivity evolution in various Fe-B based glasses (including FINEMET precursors) during relaxation and crystallization*. Acta Physica Polonica A, 131/4. (2017) 669. <https://doi.org/10.12693/APhysPolA.131.669>
- [21] Lovas A., Kisdi-Koszó É., Potocky L., Novák L.: *Effect of processing conditions on physical properties of transition metal-metalloid metallic glasses*. Journal of Materials Science, 22. (1987) 1535–1546. <https://doi.org/10.1007/BF01132372>
- [22] Cohen M. H., Grest G. S.: *Liquid-glass transition, a free volume approach*. Physical Review B, 20. (1979) 1077. <https://doi.org/10.1103/PhysRevB.20.1077>
- [23] Tsai-Wei Wu, Spaepen F.: *The relation between embrittlement and structural relaxation of an amorphous metal*. Philosophical Magazine B, 61/4. (1990) 739–750. <https://doi.org/10.1080/13642819008219307>

The Abrasion Behaviour of X40CrMoV5-1 Steel Under Various Surface Treatments

László TÓTH,¹ Tünde KOVÁCS,² Zoltán NYIKES,³ Mhatre UMESH⁴

¹ Óbudai University, Bánki Donát Faculty of Mechanical and Safety Engineering, Department of Materials Technology, Budapest, Hungary, toth.laszlo@bgk.uni-obuda.hu

² Óbudai University, Bánki Donát Faculty of Mechanical and Safety Engineering, Department of Materials Technology, Budapest, Hungary, kovacs.tunde@bgk.uni-obuda.hu

³ Óbudai University, Bánki Donát Faculty of Mechanical and Safety Engineering, Department of Materials Technology, Budapest, Hungary, zoltan.nyikes@bgk.uni-obuda.hu

⁴ Surface Modification Technologies Pvt. Ltd. Research and Development La, India, Sativali Road Vasai Road- (East), Dist. Palghar, Maharashtra-401208, umhatre@hotmail.com

Abstract

For evolving a surface layer on the X40CrMoV5-1 steel, a plasma-nitridation and PVD coating process was applied. In our experiments, the samples were heat-treated (high-temperature hardening, annealed three times) and surface treatments (plasma-nitridation, PVD coating by TiAlN, duplex surface treating by plasma nitridation and after that, PVD coating TiAlN). After the heat treatments, we performed hardness tests and surface abrasion wear tests. The abrasion wear resistance of the specimens was studied in order to understand the heat treatment effects on abrasion behaviour. It was observed that the heat treatment and surface treatment process greatly influence the tool steel surface hardness and abrasion resistance behaviour. By plasma-nitridation the surface hardness doubled compared to the quenched surface hardness while the PVD coated TiAlN surface layer hardness is more than five times that of the hardened one. There was no relevant difference between the PVD coated (TiAlN) surface hardness and the duplex surface-treated hardness. On the basis of the results of the comparative abrasive wear tests, it can be concluded that the duplex surface treatment resulted in the greatest wear resistance..

Keywords: *tool steel, secondary hardening, austenitization, PVD coating, hardness, plasma nitriding.*

1. Introduction

It is characteristic of hot-forming tool steels that they often have to meet opposing requirements at the same time, i.e. they have to function under the combined effect of different stresses. It follows that the main properties of the hot forming tool steels are hot strength, hardness, abrasion resistance, toughness, annealing resistance, thermal fatigue resistance, hot workability and machinability. These properties can be achieved partly by alloying with different chemical elements and partly by applied special heat treatment technologies. Depending on their use, there are cases where the toughness and abrasion resistance of the material are required at the same time. In such cases, surface treatments are used. The

abrasion resistance, high strength and toughness can all be achieved at the same time by applying a thin wear-resistant layer on the surface of the material. This is possible in several ways.

The X40CrMoV5-1 steel belongs to the family of hot working tool steels which is known among tool makers as EN 1.2344 The material has a very good heat resistance and hot wear resistance [1, 2]. These steels retain their properties even when working at temperatures of up to 200 °C, due to the optimal heat treatment technology and the chemical composition of the material. An increase in surface abrasion resistance is achieved by creating a thin abrasion-resistant layer [3, 4]. This can be achieved by nitriding or/and coating on hot forming tool steels.

Plasma nitriding technology was introduced in 1920, but in industrial applications has been only used for the past 30 years. The plasma nitriding technology is a thermochemical surface treatment process which is carried out at a temperature of 350–600 °C. In front of the furnace wall serving as an anode, positive ions collide at high impact velocities with workpieces connected to the cathode. This ionic shower first produces a very intensive surface cleaning and then heats and nitrides the workpiece surface [5].

Plasma nitridation can be performed in both DC and pulsed plasma. Plasma nitridation takes place in a vacuum furnace (200 to 500 Pa pressure), in an ionized gas atmosphere (ammonia, nitrogen, methane or hydrogen), but gas mixtures are also used to form more abrasion resistant surface layers.

The quality of the heat treatment is determined by the composition of the gas, the pressure, the temperature and the duration of the operation. The upper part of the nitride layer (up to 30 µm depending on the material) is hard and chemically stable, and below it is the diffusion zone with max. 1 mm thickness.

In the case of hot-forming tool steel, a surface hardness of 850–950 HV can be achieved up to a depth of 0.4 mm by plasma nitriding. The process improves the abrasion and sliding properties of the materials and creates a corrosion-resistant layer on the material surface. The dimension distortion is very small. Plasma nitriding is usually used as the final process in finished parts because after this treatment no machining is required.

The dimensions of nitrided workpieces increase by ~1 % of the bark thickness, which is an insignificant change. This procedure allows precise control of the process, fine-tuning of the microstructure of the nitride layer, and thus achieving the desired properties. PVD surface treatment is a physical vapour deposition in which the coating material is applied to the surface of the coating component in atomic, chemical compounds or ionic form. PVD processes take place at relatively low temperatures, which means that the process does not modify the tissue structure of the sub-layer and there is no allotropic transformation so that the surface-treated tool does not suffer any dimensional changes.

The PVD coating provides good sliding properties, high abrasion resistance and high hardness on the tool surface. The main purpose of the surface treatments was to increase the wear resistance of the tool. The abrasive wear is a complex system of microscopic interactions that occur be-

tween sliding surfaces. These interactions depend on the contact surfaces of the materials, on their physical, chemical, mechanical properties, of the geometry, and external conditions that affect the wear (e.g., temperature) [6–7].

Wear processes can only be investigated in a well-defined wear system, for comparison, measured results that have been determined in a similar tribological system and where only the investigated parameter changes, other parameters are minimized [8–9]. Tool wear resistance is not easy to predict. Hardness measurement is used in many places in the industry for this purpose, as there is some correlation between abrasion resistance and hardness. Similarly, comparative experimental methods are widespread, e.g. ball / flat abrasion test [10–12]. During our measurements, we examined the wear resistance of the specimens with different heat treatment and surface treatment by a comparative method and also compared their hardness values.

2. The experimental materials and technologies

The chemical composition of the tested X40CrMoV5-1 steel specimens is shown in Table 1.

Table 1. Chemical composition (%)

C	Si	Mn	Cr	Mo	V
0.40	1.10	0.45	5.25	1.41	1.2

The austenitization of the samples was performed in a VFC type 300×370×200 mm Ipsen vacuum furnace with two-stage heating (650 °C and 850 °C, respectively) at 1050 °C. The cooling was performed with 6 bar nitrogen gas. The quenching was followed by triple high-temperature tempering (Figure 1.).

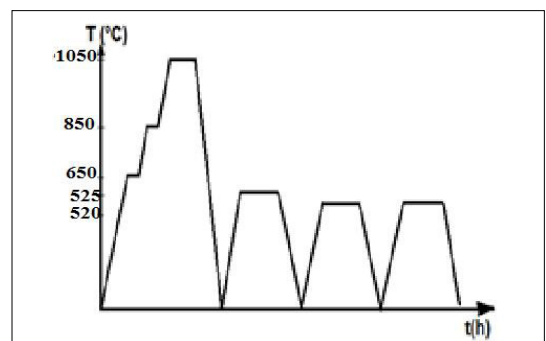


Figure 1. Az X40CrMoV5-1 steel heat treatments diagram.

Tempering was performed in a 300×370×350 mm Muehl furnace under argon gas each with two hours heating times.

After each quenching and tempering operation, Vickers hardness measurements were performed according to standard practice [13–14]. This was done on a Buhler 1105 machine. After that, samples 2 and 4 were plasma nitrided. The cleaning was performed in a mixture of hydrogen (40 L/h), argon (5 L/h) and nitrogen (1 L/h) inert gas. After that, the specimens were plasma nitrided at 480 °C for 24 hours in a mixture of hydrogen (120 L/h) and nitrogen (40 L/h) gas. After cooling, Vickers hardness measurements were performed. Samples 3 and 4 were subjected to a TiAlN PVD coating process, which was also followed by a Vickers hardness test. The final test for all four specimens was the abrasive wear test. Ball wear equipment was used for wear testing (Figure 2). Before the wear test, the roughness was measured using the roughness measuring equipment shown in Figure 3. The abrasion ball was a 20 mm diameter Al₂O₃-based ceramic ball with a polished surface. The abrasion factor (K) (1), which is calculated from the abrasion volume (V_v), the abrasion path length (S) and the load force (N), was used as the wear indicator.

$$K = \frac{V_v}{S \cdot N}, \quad \left(\frac{\text{mm}^3}{\text{N} \cdot \text{m}} \right) \quad (1)$$

The abrasion volume is calculated from the diameter of the abrasion trace (d) and the depth of the spherical bottle (h) (2):

$$V_v = \frac{h\pi}{6} \left(3d^2 + h^2 \right), \quad (\text{mm}^3) \quad (2)$$

The depth of the abrasive sphere is calculated by a simple relationship between the radius R of the abrasion ball and the diameter of the abrasion imprint ($d = 2R$) (3).

$$h = R - \sqrt{R^2 - \left(\frac{d}{2} \right)^2}, \quad (\text{mm}) \quad (3)$$

The wear path length (S) depends on the wear time (t), on the radius of the wear sphere and its speed (n) (4):

$$S = n \cdot 2 \cdot \pi \cdot R \cdot t, \quad (\text{m}) \quad (4)$$

To be comparable with the data in the literature, the speed was set at 570 rpm and the abrasion test time was 5 minutes.



Figure 2. Ball wear equipment.



Figure 3. Mahr roughness tester.

3. Test results

In the delivery condition, the average hardness of the tool steel to be tested (X40CrMoV5-1) was 215 HV.

3.1. Effects of the heat treatments (Table 2.)

After quenching from 1050 °C and three times tempering at 520 °C the hardness of the specimen was 549HV. After plasma nitriding, the hardness of the specimens 2 and 4 was 1140 HV. Sample 3, after the vacuum hardening was PVD coated with TiAlN coating and reached a surface hardness of 2938HV. Sample 4, after plasma nitriding, was PVD coated with TiAlN coating, so it was duplex surface treated and the result was a surface hardness of 2539 HV.

Table 2. The hardness after heat treatments

Sample	Heat treatment	Coating thickness (µm)	Hardness (HV)
1	Quenched and tempered	0	549
2	Quenched, tempered and plasma nitrided	0	1140
3	Quenched, tempered and TiAlN coated	2.05	2938
4	Quenched, tempered, plasma nitrided and TiAlN coated	1.93	2539

Table 3. Roughness and wear factor values

Sample	Heat treatment	Ra (µm)	Wear factor (mm ³ /(N·m))
1	Quenched and tempered	0.010	6.32×10 ⁻⁹
2	Quenched, tempered and plasma nitrided	0.057	1.95×10 ⁻⁹
3	Quenched, tempered and TiAlN coated	0.233	8.46×10 ⁻¹⁰
4	Quenched, tempered, plasma nitrided and TiAlN coated	0.177	7.57×10 ⁻¹⁰

3.2. Effects of the heat treatments

The abrasion factor calculated from roughness measurements and formula (1) is shown in the **Table 3**.

After the wear abrasion test, the diameters of the worn craters were measured with an optical microscope type Neophot 2. (**Figure 4**).

4. Conclusions

The abrasion resistance results of the examined samples from material quality X40CrMoV5-1, treated with various heat treatments and surface treatments, are shown in **Figure 5**.

- Based on the results, conclusions are as follows:
- I. The TiAlN-based PVD coating showed the highest abrasion resistance based on experimental methods and parameters.
 - II. The hardness and wear factor of the test specimen with a plasma nitrided or PVD coated surface also resulted in much more favourable properties than the surface with only a hardened and tempered conventional heat treatment.
 - III. Plasma nitrided and PVD coated surfaces, however, have a lower hardness than hardened-welded and PVD coated surfaces resulting in better abrasion resistance. However, for this result to be accurately evaluated, it is important that the surface roughness of both specimens be identical.

Acknowledgements

This work was supported by the European Union and Hungarian State, National Research, Development and Innovation Office under the 2019-2.1.11-TÉT-2019-00093 number project.

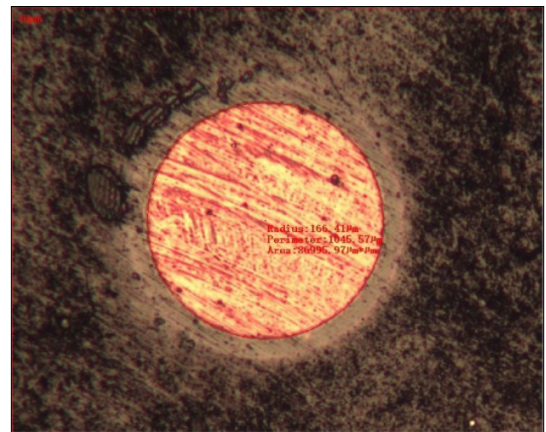


Figure 4. Wear imprint of sample nr. 3.

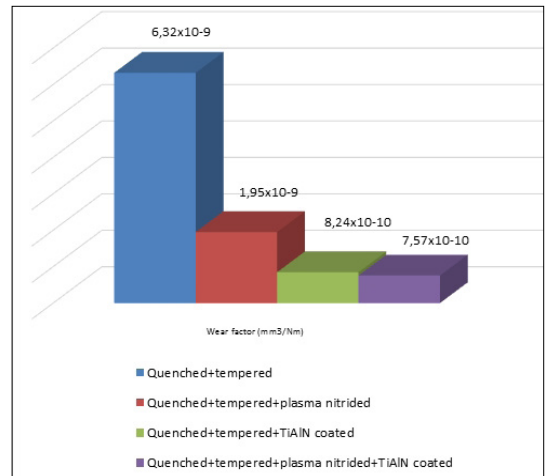


Figure 5. Measurement results: Effect of heat treatment and surface treatment technologies on the abrasion resistance of steel.

References

- [1] Takács L.: Szerszámacél ismertető – RIGOR hidegmunkaacél. Uddeholm <https://adoc.tips/szerszamacel-ismerteto-rigor-hidegmunkaacel-whenever-tools-a.html>
- [2] Borbély G.: Szerszámacélok, nemesacélok. Böhler Kereskedelmi Kft., 2009.
- [3] Bitay E.: Bevonatolt gyorsacélok kopásállósága/ Coated HS steels wear resistance. In: XVIII. FMTÜ, EME, Kolozsvár, 2013. 73–76. <https://doi.org/10.36243/fmtu-2013.10>
- [4] Bagyinszki Gy., Bitay E.: Felületkezelés. Műszaki Tudományos Füzetek 5., EME, Kolozsvár, 2009. <https://doi.org/10.36242/mtf-05>
- [5] Bagyinszky Gy., Bitay E.: Kopásálló felületkezelt rétegek minősítése/Characterization of surface treated, wear resistant layers. In: XIV. FMTÜ, Kolozsvár, 2009. 13–16. <https://doi.org/10.36243/fmtu-2009.08>
- [6] Tóth L.: Examination of the Properties and Structure of Tool Steel EN 1.2379 Due to Different Heat Treatments. European Journal of Materials Science and Engineering, 3/3. (2018) 165–170. http://ejmse.tuiasi.ro/articles/EJMSE_03_03_06_Toth.pdf
- [7] Sebestyén A., Nagyné Halász E., Bagyinszky Gy., Bitay E.: Felületmódosítási eljárások hatása acélok kopásállóságára. In: XII. FMTÜ, EME, Kolozsvár, 2007. 161–169. <https://doi.org/10.36243/fmtu-2007.4>
- [8] Tóth L., Haraszi F., Kovács T.: Surface Roughness Effect in the Case of Welded Stainless Steel Corrosion Resistance. In: Acta Materialia Transylvanica, 1/1. (2018) 53–56. <https://doi.org/10.2478/amt-2018-0018>
- [9] Titu M. A., Pop A. B., Titu S., Pop G. I.: Optimization of the objective function surface quality by end-milling dimensional machining of some aluminium alloys. ICIR Euroinvent, IOP Conf. Series: Materials Science and Engineering 572. (2019) <https://doi.org/10.1088/1757-899x/572/1/012042>
- [10] Stescu C., Chicet D., Munteanu C., Croitoru C., Cârlescu V.: Machining of thermal sprayed coatings a case study for self fluxing powder. ICIR Euroinvent, IOP Conf. Series: Materials Science and Engineering 572. (2019), <https://doi.org/10.1088/1757-899x/572/1/012051>
- [11] Sandu A. V., Baltatu M. S., Nabialek M., Savin A., Vizureanu P.: Characterization and Mechanical Properties of New TiMo Alloys for Medical Applications. Materials, 12/18. (2019), Art. nr. 2973. <https://doi.org/10.3390/ma12182973>
- [12] Kovács T., Bitay E.: The hardness control in the coated surface layer. Materials Science Forum, 729. (2012) 415–418. <https://doi.org/10.4028/www.scientific.net/MSF.729.415>.
- [13] Bitay E.: Lézeresen kezelt felületek kopásállósága. In: VI. FMTÜ, EME, Kolozsvár, 2001. 111–118. <https://doi.org/10.36243/fmtu-2001.23>
- [14] Kovács-Coskun T., Pinke P.: The Effect on Microstructure on the Local Wear Behavior of Dual Phase Steels. IOP Conference Serie: Materials Science and Engineering, 47, (2013) 012032, <https://doi.org/10.1088/1757-899X/47/1/012032>.

Effect of the Production Conditions of Continuously Cast Steels on the Degree of Hot Rolled Product Downgrading

Krisztián WIZNER,¹ Attila KŐVÁRI²

¹ ISD Dunaferr Zrt., Dunaújváros, Hungary, wizner.krisztian@isd-dunaferr.hu

² University of Dunaújváros, Institute of Engineering, Dunaújváros, Hungary, kovari@uniduna.hu

Abstract

Nowadays, quality development is a growing challenge, which places a heavy burden on economic operators, especially on smaller companies. ISD Dunaferr Zrt is the largest steel company in Hungary with its annual steel production of about 2 million tons, but it is small on a global scale. Taking advantage of the opportunities, locating the hidden problems, qualitative development and productivity enhancement can be realized without major investment. This study points out the steel production and casting parameters that have the greatest impact on the quality of the hot rolled product (sheet and coil) and touches upon the effect of rolled product final thickness on the ratio of downgrading. As a result the examination of overheating shows correlation with the ratio of downgrading, but the age of the mould does not. Regarding the thickness of the rolled product, it can be stated that in the case of thicker products (above 9 mm) the ratio of downgrading increases.

Keywords: *steel, slab, coil, casting, quality.*

1. Introduction

In September 2018, Dunaferr Zrt's continuous casting machine no. 1 was completely reconstructed, the most significant step of which was the replacement and modernization of mould level control automatics.

Downgrading ratio of the hot rolled products made from slabs cast before and after the reconstruction showed a clear improvement.

Further analyzing the data generated after the reconstruction (16,697 coils of 3,928 heats), we examined the relationship between various, primarily steel production and casting parameters and the hot rolled product downgrading data.

ISD Dunaferr Zrt's Steelworks has two LD converters (each with the capacity of 135 tons) and two vertically arranged continuous steel casters (2-2 strands). The raw steel is treated by a three-stand ladle metallurgy station located between the converters and the casting machines, without the possibility of heating. The converters are supplied with hot metal by two blast furnaces, with the total capacity of ~ 4000 m³.

After the oxygen blowing (in BOF), the liquid steel gradually cools down, until it solidifies in the casting machine. Without the possibility of heating, the treatments from BOF to mould are limited. The degree of cooling depends on multiple circumstances, for example the quality, type and quantity of alloying materials, the quantity of the flushing inert gas, but mainly on the thermal state of the ladle.

2. BOF, Ladle treatment station

In the liquid state of steel it is important to reduce the inclusion content. This can be achieved by removing active oxygen to intensify the diffusion process (afterflushing in BOF), using a deoxidizing reagent of appropriate quality and quantity (aluminium) and removing as much formed inclusion as possible with inert gas rinsing.

After the oxygen blowing, the oxygen content of the steel can reach 800–1000 ppm.

The following technical variables were analyzed during the study:

- Amount of afterflushed inert gas (argon) in the BOF;

- Amount of aluminum added for deoxidation broken down by type (solid “mokka”, loose “shredder”) [1];
- The amount of Al wire used to set the final aluminum content at the ladle treatment station;
- The amount of inert gas (argon) used to flush the steel in the ladle, broken down by source:
 - from the bottom of the ladle through porous plug, different intensity (lower argon);
 - from the top, through lance, to approx. 2 m below the surface, with high intensity (upper argon).

Rolled product properties inherited from the liquid phase depend primarily on homogeneity, inclusion content and morphology, and chemical composition. These variables are reflected mainly in the mechanical properties (e.g. tensile strength, elongation). If the mechanical properties do not meet the quality requirements, the product would usually be reclassified and would not be downgraded. For this reason, the data of the BOF and ladle treatment station did not show any correlation with downgrading data.

The product would be downgraded due to the inclusion content in the liquid steel only if the amount/morphology of inclusions in the sample taken in the vicinity of the intervention justifies it, or when it appears on the surface of the rolled product and thereby the mechanical surface analysis system (Cognex) or if the human eye can detect it.

3. Continuous casting machine

The casting processes, mainly that of the mould processes, play the greatest role in the formation of internal and external structure of cast slabs. [2-4]. Examination of the data shows that the material is downgraded typically due to surface cracking and scaling. The formation of these errors is

Table 1. Ratio of the causes of downgrading

Cause of downgrading	Ratio
Torn edge	0.00 %
Scale on the edge	0.20 %
Cracked on the edge	0.05 %
Scale on the surface	1.18 %
Rupture on surface	0.11 %
Inclusion on the surface	0.27 %
Cracked on the surface	0.14 %
Based on an inclusion test	0.18 %
Total downgrading	2.11 %

primarily the result of complex processes in the mould [5-7].

3.1. Tundish

The primary role of the tundish is to create a liquid steel buffer, which is essential for continuous casting during the ladle change. The temperature probe in the tundish provides data on the temperature of the steel entering the mould. The difference between the liquidus temperature calculated from the steel composition and the actual measured temperature gives the degree of overheating of the liquid steel. Low overheating poses technical risk, because cast steel may solidify before needed and there is no possibility of heat transmission outside the BOF. High overheating means casting safety, but a greater burden on the cooling system (mould, secondary cooling zones).

The Al-O balance shifting during the cooling of steel triggers a fine inclusion precipitation, the higher the degree of cooling, the more significant inclusion precipitation is. In the mould, this phenomenon intensifies as a result of intense, direct heat dissipation, and inclusions can more easily get close to the surface.

Figure 1 shows the relationship between downgrading and the overheat in the tundish.

3.2. Mould

The mould makes an oscillating motion [8-10] to form a solid shell on liquid steel, which is capable of retaining the internal liquid portion against the ferrostatic pressure during its movement to

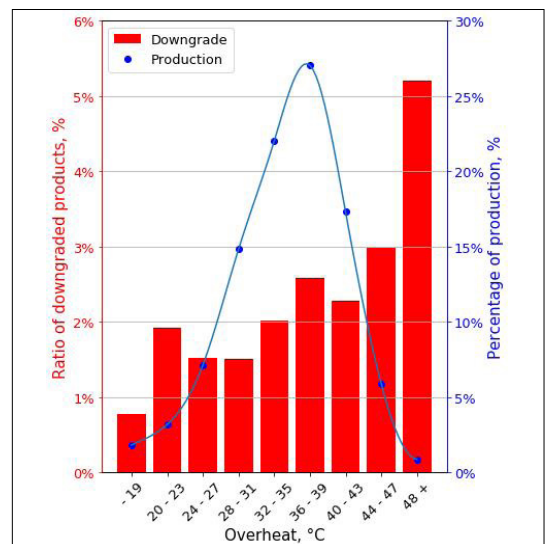


Figure 1. Relationship between the ratio of downgrading and the degree of overheating.

wards the lower zones. In the mould, heat is removed through water-cooled, nickel-plated copper sheets.

3.2.1. The age of the mould

The mould is subject to numerous mechanical effects during casting, which can cause uneven wear and tear on the inner surface of the mould, and these internal irregularities may affect the surface quality of cast slabs. Due to the feeding of the dummy bar from below before casting, mechanical wear occurs at the bottom of the cooling plates. In the case of splashes of liquid steel, the steel droplets may fall into the surface of the cooling plates, which are removed by grinding in cold state. At the meniscus of the held steel level, traces of liquid steel and melting casting powder can be observed.

Contrary to the assumption, the values in Figure 2 do not show a significant correlation between the degree of downgrading and the age of the mould. Presumably because the solid and liquid steel directly touches the wall of the mould only on the short section, such a deep roughness cannot develop in this section, the depth of which would exceed the thickness of the layer burning down later in the reheating furnace.

3.2.2. Fluctuation of casting speed and steel level in the mould

The change in casting speed and the mould steel surface have a significant effect on both the inter-

nal and external properties of cast strand. [11-15] Examining these changes in terms of time and length did not produce significant results, which is presumably due to the fact that the strand sections burdened with major changes are cut off and subsequently not used. Thus they do not cause significant downgrading.

3.3. Secondary cooling zone

The role of the secondary cooling zones below the mould is the stable support of the strand and its further cooling until it solidifies in entire cross section. Earlier observations suggested that casting problems (e.g. bearing breakage, roller bumps) occur quickly and visibly. They did not appear during the period under investigation, so their effects were not investigated.

The cooling strategy of the strand is determined first of all by the quality of the heat and the width of the strand (section size). The degree of overheating has an effect on the maximum casting speed of the strand, so that the appropriate heat dissipation can be achieved in order to solidify the entire cross section. [15]

Due to chemical similarity, only the section size affects the cooling strategy of the examined steel grades, therefore it has been investigated on this basis.

In Figure 3 the data show an extremely high ratio of downgrading at the widest section width.

The amount cast on B15 (1550 mm wide) section and the high ratio of downgraded material sub-

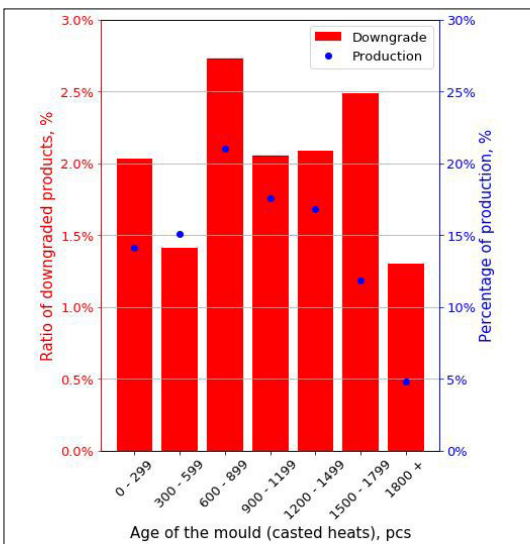


Figure 2. Relationship between downgrading and the age of the mould.

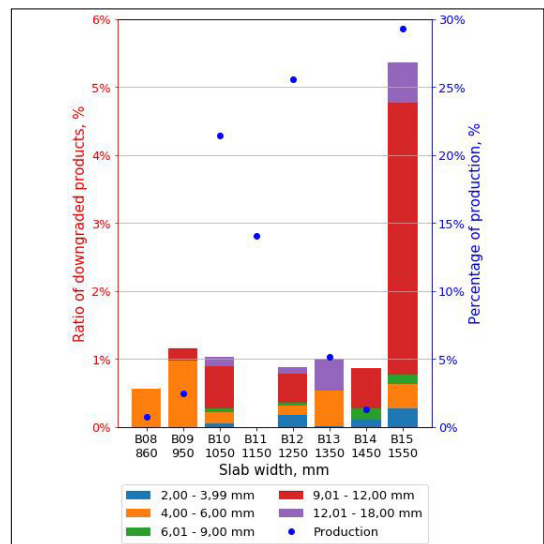


Figure 3. Relationship between the ratio of downgrading to slab width.

ject to regular inspections during the investigated period exclude that the problem arises from local nozzle failure, clogging. Rather, it suggests that production parameters, which depend on the section size in the production line (Casting Machine, Hot Rolling Mill), is responsible for the phenomenon. Finding the exact reasons is beyond the scope of this study.

4. Hot rolling

In this study it is mainly the technological variables of steelworks that were analyzed. Hot rolling mill production properties were not subject to the study, but based on experience it seemed appropriate to examine the relationship between the thickness of the rolled product (degree of deformation) and the downgrading. The thickness categories were selected according to the manufacturing technology of typical products.

According to conjecture, it can also be seen from the chart in [Figure 4](#) that the degree of downgrading in thicker product categories is significantly higher.

5. Conclusions

The tested properties of the BOF and ladle treatment station mainly affect the mechanical properties of the hot rolled product. In case of non-compliance, the product is usually reclassified to a different quality. Presumably for this reason, investigations did not reveal any correlation with downgrading.

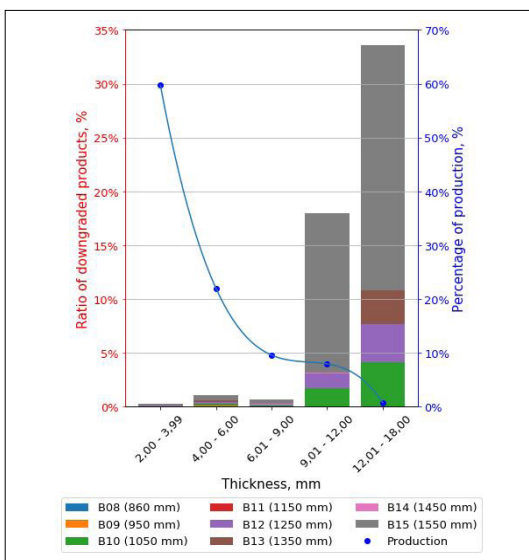


Figure 4. Relationship between downgrading and the final thickness of rolled flat product.

The examination of overheating shows correlation with downgrading. In the lower temperature range (near the liquidus temperature), the steel solidification process can already start due to cooling in the casting chain. However, in the higher temperature range, the thermal burden of the mould increases, which will have a negative effect on the surface of the strand. Current casting with high overheating, mostly at 35–40 °C, is the consequence of the supply of raw materials and refractory materials from non-permanent suppliers. Due to the uncertainty, it is necessary to keep a constant supply of safety heat reserve. Supplying raw materials and refractory materials from continuous, steady sources can reduce tapping and casting temperatures, leading to quality improvements and cost savings.

There was no correlation between the age of the mould and downgrading. This is presumably due to the short, direct contact of the molten steel with the mould wall, during which no such deep defect arising from the uneven surface of the mould can form that will not burn down in the reheating furnace.

Investigating the change in casting speed and mould steel level did not deliver any measurable results. This is primarily due to the fact that the strand segments affected by major changes are cut out and not rolled.

According to the data, the downgrading ratio of 1550 mm wide (B15) slabs, which is significantly higher than the others, is not a maintenance problem (e.g. nozzle clogging), instead it is caused by other cooling specifics depending on the section size. Exploring the cause of the error affects complex review of the cooling strategy of both the continuous caster and the hot rolling mill.

Regarding the thickness of the rolled product, it is clear regardless of the section size, that in the case of thicker products (above 9 mm) the degree of downgrading increases significantly. This leap in the case of products thicker than 12 mm can be partly explained by the fact that they can be sold only in coils. There is no possibility of cutting and thus a full coil is downgraded even in the case of partial problems. [Figure 3.](#) and [4.](#) show that the largest portion of the thick product (above 9 mm) is produced on a B15 (1550 mm wide) section.

Based on the above data, it can be concluded that the effects of the section size and the thickness of the rolled product add up, and the risk of downgrading significantly increases in case of thick, wide products.

Acknowledgments

The study is funded by „EFOP-3.6.1-16-2016-00003 K+F+I folyamatok hosszú távú megerősítése a Dunaújvárosi Egyetemen” project.

References

- [1] Wizner K., Kővári A.: *Efficiency of different kinds of aluminiums during deoxidation in the Steelworks of ISD Dunaferr Co. Ltd.* IOP Conf. Series: Materials Science and Engineering, 426. (2018) 012052 <https://doi.org/10.1088/1757-899X/426/1/012052>
- [2] Meng Y., Thomas B. G.: *Heat transfer and solidification model of continuous slab casting: CON1D.* Metall. & Material Trans., 34B/5. (2003) 685–705. <https://doi.org/10.1007/s11663-003-0040-y>
- [3] Zhang L., Pluschkell W., Thomas B. G.: *Nucleation and growth of alumina inclusion during steel deoxidation.* In: Proceeding of 85th Steelmaking Conference, Vol. 85. ISS, Warrendale, PA, 2002. 463–476.
- [4] Thomas B. G., Jenkins M., Mahapatra R. B.: *Investigation of strand surface defects using mold instrumentation and modeling.* Ironmaking & Steelmaking, 31/6. (2004) 485–494. <https://doi.org/10.1179/030192304225019261>
- [5] Brimacombe J. K., Sorimachi K.: *Crack formation in the continuous casting of steel.* Metallurgical Transactions, B, 8/2. (1977) 489–505. <https://doi.org/10.1007/BF02696937>
- [6] Schmidt K.-D. et al.: *Consequent improvement of surface quality by systematic analysis of slabs.* Steel Research, 74/11. (2003) 659–666.
- [7] Thomas B. G.: *Modeling of continuous casting defects related to mold fluid flow.* In: Proceeding of 3rd Int. Congress on Science & Technology of Steelmaking, AIST, Warrendale, PA, 2005. 847–861.
- [8] Shin H.-J., Lee G. G., Choi W. Y., Kang S. M., Park J. H., Kim S. H., Thomas B.G.: *Effect of mold oscillation on powder consumption and hook formation in ultra low carbon steel slabs.* Iron Steel Technology, 2/9. (2004) 15–17.
- [9] Thomas B. G., Sengupta J., Ojeda C.: *Mechanism of hook and oscillation mark formation in ultra-low carbon steel.* In: Proceeding of Second Baosteel Biennial Conference, Vol. 1, 2006. 112–117.
- [10] Sengupta J., Thomas B. G., Shin H.-J., Lee G. G., Kim S.-H.: *A new mechanism of hook formation during continuous casting of ultra-low-carbon steel slabs.* Metallurgical and Materials Transactions, 37/5. (2006) 1597–1611. <https://doi.org/10.1007/s11661-006-0103-1>
- [11] Thomas B. G.: *Continuous Casting of Steel.* In: Modelling for casting and solidification process, (Ed: O. Yu) Marcel Dekker, New York, NY, 2001. 499–540.
- [12] Sengupta J.: *Effect of a sudden level fluctuation on hook formation during continuous casting of ultra-low carbon steel slabs.* In: Modeling of Casting, Welding, and Advanced Solidification Processes XI. (Szerk. Gandin C. A., Allison J. E.). TMS, Warrendale, PA, 2006. 727–736.
- [13] Shin H.-J., Thomas B. G., Lee G. G., Park J. M., Lee C. H., Kim S. H.: *Analysis of hook formation mechanism in ultralow-carbon steel using CON1D heat flow solidification model.* Materials Science and Technology 2, TMS, Warrendale, PA, Vol. II, 2004. 11–26.
- [14] Zhang Q., Wang L., Wang X.: *Influence of casting speed variation during unsteady continuous casting on non-metallic inclusions in IF steel slabs.* ISIJ International, 46/10. (2006) 1421–1426.
- [15] Wang Y., Zhang L.: *Transient fluid flow phenomena during continuous casting: Part II—cast speed change, temperature fluctuation, and steel grade mixing.* ISIJ International, 50/12. (2010) 1783–1791. <https://doi.org/10.2355/isijinternational.50.1783>